

Flow Separation Characteristics Within Rectangular and Conical Diffusers



Arthur Hajaali

School of Engineering

Cardiff University, Wales, UK

Supervised by:

Prof. Shunqi Pan and Dr. Zhihua Xie

This thesis is submitted in partial fulfilment of the requirements
for the degree of

Doctor of Philosophy (Ph.D.)

2020

Acknowledgements

I changed supervisor during my PhD, so it binds me to thanks both Professor Thorsten Stoesser and Professor Sunqi-Pan for supervising my research at the School of Engineering at Cardiff University. Their inputs were substantial for my personal development as a researcher.

Great appreciation to the Engineering and Physical Sciences Research Council in the UK for awarding the grant, EP/L016214/1 to the Water Informatics: Science and Engineering (WISE) Centre for Doctoral Training which has generously supported this work.

First, I want to thanks Alex! Without him, I would never have applied and embarked on this long journey, I truly enjoyed collaborating with him on some projects during my PhD. During these years, I spent most of my time coding in Fortran and post-processing to acquire the relevant results for my thesis. I had a formidable time exchanging ideas with my office colleagues (Valentine, Giovanni, Ben), it was really a pleasant environment to work in, so thank you!

A special mention to the UCL team, where I undertook a three-months internship. Filipa (bruv'), you have my forever gratitude for helping me move into London, best blablacar ever! Qianyu, although you most probably have surpassed me now, working with you on the coding helped me realise the progression I had made. Finally, Lucy thanks you for the few times you convinced me to go to the climbing center, I loved it once I was there!

Lastly, I am very thankful to my family for supporting me emotionally and helping me financially during my last year of PhD. I am awfully grateful to my partner Elena, who stayed at my side and

learned to navigate and uplift my moods in some of these turbulent times. Echizeni, our arrogance both led us to do a PhD, well it has humbled us, I truly appreciated our videocall working sessions. Throughout this PhD I had the best two years with my housemate Ben and Corentin, guys I will always cherish our cooking and geeking sessions. All the weekends spent playing board game, barbecuing in Bute park with all my friends from Cardiff made the experience much more enriching. Thank you all for these memories.

Cardiff, 2020

Arthur Hajaali

Abstract

The concept of a diffuser relies on transforming the dynamics or velocity pressure into static pressure. This simple concept found numerous application including in the jet engine, sewage, optics, automotive, ventilation systems. During the first half of the 20th century, a multitude of diffuser designs were investigated to provide valuable information and guideline in optimising their efficiency. The performance of diffuser is extremely sensitive to its geometry and inlet condition, which can lead to the flow separation of the turbulent boundary layer and the development of reversal flow. This reversal flow is the main contributor to the pressure losses leading to a drop in the diffuser's efficiency. The three-dimensional nature and the unsteadiness of the reversal flow makes it experimentally and numerically challenging to study and quantify its characteristics and underlying mechanisms.

This research operates and analyses high-resolution Large Eddy Simulation (LES) to further the understanding of the flow mechanisms and interactions with the coherent structures responsible for the emergence of instantaneous reversal flow pockets. The flow separation geometrical sensitivity is assessed through the investigation of two different asymmetric rectangular diffusers. Moreover, the flow separation temporal behaviour and the arrangement of the energy-containing motions are evaluated within a conical diffuser when subjected to a fully developed pipe inlet and a swirling boundary condition. Prior to these parametric studies, the hydrodynamics of each diffuser were calibrated and validated extensively with experimental data.

Two publications derived from the work undertaken in this thesis have been submitted.

Journal papers

1. **A. Hajaali**, T. Stoesser. Flow separation behaviour within three-dimensional asymmetric diffusers . *Submitted to Journal of Flow, Turbulence and Combustion.*
2. **A. Hajaali**, T. Stoesser. Impact of swirling inflow on conical diffusers' efficiency of a conical diffuser and their coherent structure . *Submitted to Journal of Fluids Engineering, ASME.*

Nomenclature

Abbreviations

CD16degFu	Wide opening angle conical diffuser with a fully developed inlet
CD16degSw	Wide opening angle conical diffuser with a swirling inlet
CD8degFu	Narrow opening angle conical diffuser with a fully developed inlet
CFD	Computational Fluid Dynamics
CFL	Courant-Friedrichs-Lewy condition
CV	Concentrated Vortex swirling inlet
D1	Diffuser 1
D2	Diffuser 2
DNS	Direct Numerical Simulation
FS	Flow Separation
FTP	Flow Through Passage
HLR	Hybrid LES/RANS
HWA	Hot-Wire-Anemometer
IBM	Immersed Boundary Method
IBP	Immersed Boundary Points
ID	Incipient Detachment
ITD	Intermittent Transitory Detachment
JW	Jet-Wall swirling
KH	Kevin-Helmholtz instability
LDA	Laser Doppler Anemometry
LDV	Laser Doppler Velocimetry
LES	Large Eddy Simulation
LMR	Local Mesh Refinement

LSE	Linear Stochastic Estimation
LSM	Large-Scale Motion
MPI	Message-Passing Interface
MRV	Magnetic Resonance Velocimetry
OpenMP	Open Multi-Processing
PD	Permanent Detachment
PDF	Power Density Function
PISO	Pressure-Implicit with Splitting of Operators
PIV	Particle Image Velocimetry
PSD	Power Spectral Density
PTD	Persistent Transitory Detachment
RANS	Reynolds Averaged Navier-Stokes
SB	Solid-Body swirling inlet
SGS	Sub-Grid Scale
SI	Secondary Instabilities
SIMPLE	Semi-Implicit Method for Pressure Linked Equations
SIP	Strongly-Implicit Procedure
TD	Transitory Detachment
TKE	Turbulent Kinetic Energy
VITA	Variable-Interval Time-Averaging
VLSM	Very Large-Scale Motion
WALE	Wall-Adapting Local Eddy viscosity model

Dimensionless parameters

AER	Asymmetric Expansion Ratio
AR	Area Ratio
AS	Aspect Ratio
BV	Backflow Volume
C_{PRi}	Ideal pressure recovery
C_{PR}	Actual pressure coefficient
FV	Fractional Volume
H_L	Dimensionless Headloss
$R_{\mathbf{v}\mathbf{v}}$	Auto-correlation
Re	Reynolds Number

St Strouhal Number

Symbols

η Efficiency of the diffusers

λ_2 Vortex criterion

ν Kinematic viscosity

ν_t Turbulent/Eddy viscosity

ω Rotation rate

ρ Fluid density

θ Opening angle of conical diffusers

F Lagrangian force

f Eulerian and external forces

lx, ly, lz Computational domain axes length

N_{DE} Number of elements located within the diffuser

N_e Number of elements in the computational domain

$N_e - Op$ Optimised number of elements in the computational

n_x, n_y, n_z Axes number of cells

P Pressure

r Radial position

S Strain rate

t Time

u, v, w Cartesian Velocities

V_x, V_r, V_t Cylindrical Velocities

x, y, z Eulerian Coordinates

Subscripts Superscripts

$(.)'$ Fluctuation value

$(.)^+$ Variable expressed in wall-units

$(.)_0$ Initial or inlet conditions

$(.)_c$ Centerline value

$(.)_{mag}$ Scalar magnitude value

$(.)_{rms}$ Root mean square value

$\overline{(.)}$ Time-averaged variable

List of Figures

2.1	Ideal and actual pressure distribution in a conical diffuser from Legg [2017]	7
2.2	Schematic representation of the various diffuser geometrical parameters	8
2.3	(a) Eiffel and (b) Gibson performance curves based on the opening angle 2θ and the length x/R of the diffuser (McDonald & Fox [1966])	9
2.4	(a) Schematic representation of a horseshoes vortex (Adrian [2007]), (b) Experimental picture of a single horseshoe (Bandyopadhyay [1980])	12
2.6	Swirling inlet impact on the performance of numerous conical diffusers (Mcdonald <i>et al.</i> [1971])	14
3.1	Schematic representation of the periodic boundary condition	19
3.2	Representation of a tangential velocity exiting a swirling generators	21
3.3	2D representation of IBP Lagrangian points and their respective ϕ interpolation from Eulerian grid point neighbours	23
3.4	Komogolov's Energy Cascade	25
3.5	Three-dimensional representation of the Cartesian staggered grid .	29
4.1	Three-dimensional dimensions of the precursor channel and the two asymmetric rectangular diffusers D1 and D2	37
4.2	Inlet flow conditions: (a) Mean streamwise velocity, (b) Root mean square of streamwise fluctuation	37
4.3	Normalised mean streamwise velocity \bar{u}/U_b : (a) Vertical plane $z/H=1/2$, (b) Vertical plane $z/H=7/8$, (c) Horizontal plane $y/H=1/8$	39

4.4	Iso-surface of the Flow separation ($\bar{u} = 0.001$) with a normalised root mean square of the fluctuation contour (u_{rms}/U_b) : (a) D1, (b) D2, the dotted rectangles represent the cross-section locations of Fig.4.5	41
4.5	Normalised mean streamwise velocity contour (\bar{u}/U_b) of D1 and D2 at multiple cross-sections ($x/H=5,8,12,15$). Contour lines spaced 0.1m/s apart, bold line represents $\bar{u}/U_b = 0$	42
4.6	Fractional area occupied by the mean flow separation within the rectangular diffusers: D1 and D2	43
4.7	Vertical profiles located on the vertical plane $z/H=1/2$: (a) Normalised root mean square of the streamwise turbulent fluctuations u_{rms}/U_b , (b) Normalised shear stress $\overline{u'v'}/U_b$	45
4.8	Contours of the turbulent kinetic energy at multiple cross-sections ($x/H=5,8,12,15$) along the D1 and D2, the white line represents the mean zero-streamwise velocity $\bar{u} = 0$	46
4.9	(a) One-dimensional pressure coefficient C_p , (b) Dimensionless pressure gradient $P+$ along the two rectangular diffusers	47
4.10	D1: Side and top views of normalised instantaneous streamwise velocity u/U_b at three selected instants in time: $t=0.54,1.1,1.86$	49
4.11	D2: Side and top views of normalised instantaneous streamwise velocity u/U_b at three selected instants in time: $t=2.86,4.43,6.35$	50
4.12	Backflow coefficient contours of the vertical plane $z/H=7/8$: (a) D1, (b) D2	53
4.13	Backflow coefficient contours of the horizontal plane $y/H=1/8$: (a) D1, (b) D2	53
4.14	(a) Flow separation total volume time series across expansion and extension sections of the two rectangular diffusers and (b) PSD of the flow separation total volume series	54
4.15	Quadrant Analysis of the shear stress $u'v'$ at specific locations across D1	57
4.16	Quadrant Analysis of the shear stress $u'v'$ at specific locations across D2	58

4.17	Iso-surface Q Criterion (75000) contoured with the normalised Velocity magnitude (U_{mag}/U_b) : (a) D1 , (b) D2	60
5.1	(a) Three-dimensional representation of the swirling generator and the wide opening angle conical diffuser, (b) Evolution of the radius number of cells along the diffuser, (c) Two-dimensional representation of the computational domain for the wide opening angle conical diffuser (Grid points only plotted every four points for clarity)	69
5.2	(a) Normalised mean tangential velocity \overline{V}_t/U_b at five different stations along the pipe, (b) Inlet normalised root mean square of the axial,radial and tangential velocity fluctuations and (c) Normalised mean axial velocity \overline{V}_x/U_b at five different stations along the pipe, (d) Swirling decay along the pipe	71
5.3	(a) Dimensionless mean axial velocity profile U^+ , (b) Inlet normalised root mean square of the axial,radial and tangential velocity fluctuations, (c) Normalised mean axial velocity profiles \overline{V}_x/U_b at four locations along CD8degFu, (d) Normalised root mean square of the axial velocity fluctuations Vx_{rms}/U_b at two locations along CD8degFu	72
5.4	(a) Normalised mean axial velocity \overline{V}_x/U_b along the conical diffusers normalised length (AR), (b) Normalised mean axial velocity of the conical diffusers centerline $\overline{V}_c/\overline{V}_{c_{ref}}$ along the normalised length AR	74
5.5	Normalised root mean square of the axial fluctuations Vx_{rms}/U_b along the three conical diffusers	75
5.6	Normalised turbulent kinetic energy TKE/U_b^2 along the three diffusers	77
5.7	(a) One-dimensional wall pressure coefficient C_p , (b) Skin Friction coefficient C_f along the conical diffusers	77
5.8	Iso-Surface of the mean streamwise velocity $\overline{V}_x = -0.005$ with TKE/U_b^2 contour: (a) CD16degFu (b) CD16degSw	79

5.9	Fractional area of the reversal flow along the three conical diffusers with backflow coefficient: (a) Mean : $\gamma = 50\%$, (b) Intermittent : $\gamma = 80\%$	79
5.10	Backflow coefficient contour within the three conical diffusers: (a) CD8degFu (b) CD16degFu (c) CD16degSw	81
5.11	(a) Total instantaneous backflow fractional volume time-series within the two wide opening angle conical diffusers, (b) FFT: CD16degFu, (c) FFT: CD16degSw	82
5.12	Iso-Surface of the normalised mean tangential velocity \overline{V}_t/U_b with a iso-contour of the normalised mean axial velocity \overline{V}_x/U_b : (a) PipeSw, (b) CD16degSw, (c) Swirling decay along PipeSw and CD16degSw	83
5.13	Cross-section vector field at two different locations (AR=1.74,2.71) within three conical diffusers: (a,d) CD8degFu, (b,e) CD16degFu, (c,f) CD16degSw	85
5.14	Instantaneous axial and tangential velocity fields at two different times (t=24.6s and t=31.8s) within CD16degFu	87
5.15	Instantaneous axial and tangential velocity fields at two different times (t=22.1s and t=27.3s) within CD16degSw	88
5.16	Iso-Surface of the criterion $\lambda_2 = 20\%$ of maximum value with r/R contour joint with the iso-surface of the instantaneous axial velocity $V_x = 0$ in grey: (a) CD16degFu (b) CD16degSw	89
5.17	Iso-contour of the instantaneous axial fluctuation V'_x at the wall: (a) CD16degFu (b) CD16degSw	90
5.18	Two-points correlations of the axial velocity at four different locations (AR=1.26,1.83,2.82,3.74) along the conical diffusers: (a) CD8degFu, (b) CD16degFu, (c) CD16degSw	93
5.19	Two-points correlations of the radial velocity at four different locations (AR=1.26,1.83,2.82,3.74) along the conical diffusers: (a) CD8degFu, (b) CD16degFu, (c) CD16degSw	94
5.20	Two-points correlations of the tangential velocity at four different locations (AR=1.26,1.83,2.82,3.74) along the conical diffusers: (a) CD8degFu, (b) CD16degFu, (c) CD16degSw	95

List of Tables

4.1	Mesh resolution of the different simulation computational domains	36
4.2	Fractional Volume (FV) occupied by the backflow coefficient: $\gamma = 0.99, 0.5, 0.2$ within the rectangular diffusers D1 and D2	52
5.1	Mesh resolution and configuration of the simulations	67

Contents

Declaration	i
Acknowledgements	iii
Abstract	iv
Nomenclature	vii
List of Figures	viii
List of Tables	xii
Contents	xiii
1 Introduction	1
1.1 Motivation	1
1.2 Objectives and Thesis structure	2
2 Literature Review	5
2.1 Diffuser history and design	5
2.2 Hairpin Vortices	11
3 Hydro3D Numerical Framework	15
3.1 Governing-Equation	15
3.2 Domain Decomposition and Parallel Computing	17

3.3	Boundary Condition	18
3.4	Geometry: Immersed Boundary Method	22
3.5	Sub-grid scale model	25
3.6	Time and Spatial Discretisation	28
4	Rectangular Diffuser: Influence of the geometrical aspect ratio on flow separation behaviour	32
4.1	Overview	32
4.2	Computational set-up	35
4.3	Results and Discussion	38
4.3.1	Time-averaged flow	38
4.3.2	Turbulence statistics and kinetic energy	44
4.3.3	Pressure and efficiency	47
4.3.4	Instantaneous flow	48
4.3.5	Unsteadiness of the flow separation	51
4.3.6	Turbulent boundary layer and coherent flow structures	55
4.4	Summary	61
5	Conical Diffuser: Impact of a swirling inlet onto the flow-separation behaviour	63
5.1	Overview	63
5.2	Computational Set-Up	66
5.3	Results and Discussion	70
5.3.1	Simulation calibration and validation	70
5.3.2	Time-averaged flow field	73
5.3.3	Unsteadiness of the flow separation	78
5.3.4	Swirling decay	83
5.3.5	Instantaneous flow	84
5.4	Conclusion	93
6	Conclusions, Contributions, and Recommendations for Further Studies	97
6.1	Conclusions	97

6.2 Thesis Contributions	100
6.3 Recommendations for Further Studies	101
References	105

Chapter 1

Introduction

1.1 Motivation

The design of diffusers and their optimisation has been extensively researched over the years. Numerous geometrical and inlet factors including opening angle, aspect ratio, area ratio, inlet distribution and swirling inlet alter the performance of a diffuser. These researches were mainly experimental and only monitored the pressure drop along the diffuser wall using Pitot tubes in order to determine the performance of the diffuser. The alteration of the pressure recovery was closely linked with the development of instantaneous reversal flow within the diffusers. More recent experimental and numerical studies provided the mean properties of the flow separation including its size and location but only a few attempt to describe the behaviour of the instantaneous reversal flow. The three-dimensional nature of the flow separation constitutes a great challenge to quantify its unsteadiness and its instantaneous hydrodynamic behaviour. The impact of the geometrical and inlet change onto the arrangement of the coherent structure which leads to the emergence of the instantaneous flow separation from the turbulent boundary layer stills remains unclear for the research community. Improving the understanding of these mechanisms which in turn affect greatly the efficiency of diffusers will contribute to the amelioration of their design.

1.2 Objectives and Thesis structure

The high-fidelity diffuser simulations performed using the in-house LES software Hydro3D ensured the investigation and correlation of the emergence of the flow separation with the distribution of the coherent structure within the turbulent boundary layer supported by recent prediction consensus. The findings of this thesis validate and reject some of the main theoretical predictive models including Theodorsen horseshoes, Townsend attached eddies and Adrian single hairpin eddies. To further understand the impact of geometrical (a/b) and inlet changes (b) on the development and behaviour of the reversal flow, two different diffuser cases are examined: (a) an asymmetrical rectangular diffuser and (b) an axisymmetric conical diffuser. The influence of the different geometrical and design factors such as the area ratio ($AR = A_{outlet}/A_{inlet}$), aspect ratio ($AS = height/base$) and opening angle ($2\theta = 2 * \text{asin}(R_{outlet}/R_{in})$) on the size, location and unsteadiness of the backflow region is evaluated. The asymmetric conical diffuser furthers the global knowledge on the impact of a swirling inlet onto the development and behaviour of the reversal flow. The most important industrial factor remains the efficiency of a diffuser, so ultimately, the effect of the flow separation and reversal flow on the diffuser's performance is assessed in both cases.

- Chapter 2 is a literature review which provides the necessary understanding on diffuser designs based on previous and current research. For the reader interest, it links history and science; the chronological development of diffuser throughout the 20th century is provided. The fundamental principles responsible for the development and classification of the coherent structure within the turbulent boundary layer is explained. Finally, the swirling inlet literature provides key information on the different swirling generation methods and their applications.
- Chapter 3 presents Hydro3D, the in-house LES software used to perform all the simulations of this research. The underlying principles and methods implemented in Hydro3D, including the governing equation, the fractional-step method and the Immersed Boundary Method (IBM) are introduced. The implementation of a new methodology to prescribe a turbulent swirling

inlet as boundary condition is also described.

- Chapter 4 explores and compares the hydrodynamics of the flow separation within two different asymmetrical rectangular diffusers, D1 and D2. The duct inlets of these diffusers are identical while their aspect ratio diverge: $AS_{D1} = 1$ and $AS_{D2} = 0.75$, leading to a slight difference in their respective area ratio: $AR_{D1} = 4.80$, $AR_{D2} = 4.56$. The mean first and second-order statistics are validated with [Cherry *et al.* \[2008\]](#) experiment prior to investigation of the instantaneous flow field. The temporal behaviour of the flow separation is evaluated using numerous analytical tools, including the backflow coefficient and the Fast Fourier Transformation (FFT) of the backflow volume (BV) time-series. The coherent structures responsible for the emergence of the instantaneous reversal flow are depicted and visualised using the quadrant analysis in conjunction with the Q-criterion.
- Chapter 5 first validates the swirling implementation and the mean hydrodynamics within a narrow opening angle $2\theta = 8^\circ$ conical diffuser using [Rocklage-Marliani *et al.* \[2003\]](#) and [Okwuobi & Azad \[1973\]](#) experimental data respectively. Previous studies suggested that this expansion angle is the most efficient in preventing the formation of the backflow region. For this reason, a parametric study is performed on a higher expansion angle $2\theta = 16$ to ensure the development of mean flow separation. A swirling number ($Sw=0.6112$) is then prescribed to the inlet, and its effect on the velocity field, flow separation instantaneous behaviour and the efficiency of the diffuser is examined. The effect of the adverse-pressure gradient on the swirling decay within the diffuser is evaluated. A classification of coherent structures present in both flow is provided through the visualisation of two-dimensional instantaneous flow fields, λ_2 criterion and the two-point correlations. These observations are also compared with the aforementioned coherent structure predictive models
- Chapter 6 summaries the impact of the geometrical changes and inlet type on the coherent structure distribution responsible for the bursting of the flow separation with turbulent boundary layer and the behaviour of its reversal

flow. The impact of this reversal flow on the efficiency of the diffuser is reviewed. The main contribution of this thesis and further axe of research ensuing from its finding is provided.

Chapter 2

Literature Review

This section intends to provide the reader with the necessary tool and background to facilitate its understanding of the analysis performed in this thesis. The scientific literature on diffuser design, turbulent boundary layer, coherent structure and swirling flow is introduced chronologically.

2.1 Diffuser history and design

A diffuser consists of an abrupt or gradual expansion of the cross-section of geometries including duct or pipe along a specific distance. Natural and geologic diffusers can be observed, for instance, if considering the river Taff in Cardiff, when reaching and pouring into Cardiff bay, the flow is subjected to an abrupt expansion. From an engineering point of view, the main purpose of a diffuser is to transform dynamics pressure into static pressure by decelerating the flow or in other words, it reduces the kinetic energy of the incoming flow. Diffusers are ubiquitous in engineering applications for instance in pipe networks in the water or in the ventilation industry (Laliberte *et al.* [1983]). They are also often succeeding the combustion chamber (Fishenden & Stevens [1977]) in jet engines in the aeronautics and automotive industry. Diffusers are used in the form of draft tubes of hydro turbines such as bulb (Duquesne *et al.* [2016]), Kaplan (Daniels *et al.* [2020]) or Francis turbines (Zhang *et al.* [2009]). The industry's infatuation with

optimising diffuser designs to minimise energy losses has led to a sea of experimental research since the 20th century to further understand the key parameters affecting the diffuser efficiency. The first experiments on diffuser were undertaken more than two century ago. [Venturi \[1797\]](#) research was entirely based on the Bernoulli equation and was precursor in studying the transfer of velocity head into pressure head while accounting for the mechanical losses affecting the total pressure of the system.

This principle can also be defined as pressure recovery as shown in Fig.2.1 where p_s is the static pressure, p_v corresponds to the velocity pressure also called dynamic pressure, C_{pi} is the ideal pressure coefficient, H_L is the head loss, and $C_p = C_{pi} - H_L$ the pressure coefficient. This research became renown for the reversed principle when the reduction of fluid pressure occurs when a pipe flow is conveyed through a constricted section, also known as the Venturi Effect.

It is in the early-mid 20th century that the modern diffuser design guidance emerge from a collection of scientific papers which experimentally investigated multiple parameters on diffuser and their impact on the efficient which is solely based on head pressure losses. At the time, precision tools including Laser Doppler Velocimetry (LDV), Laser Doppler Anemometry (LDA) or Particle Image Velocimetry (PIV) were yet to be created restraining the hydraulic researcher to the pilot tubes instrumentation to assess the pressure gradient across the diffusers. From [Patterson \[1938\]](#) review paper, two main categories altering the performance of the diffuser are introduced. The first category relies on the geometrical parameters including the opening angle (θ), length (L), area ratio ($AR = A_2/A_1$), aspect ratio ($AS = h/b$), curvature (β), and length of the tail section (Γ) of the diffuser as illustrated in Fig.2.2. The second factor corresponds to the inlet characteristic influenced by the Reynolds number, the velocity profile distribution, the vortex generation, the swirling inlet. It is essential to understand the main goal of these design guidelines is to optimised the performance of the diffuser for the lowest infrastructural cost. The remaining of this section provide concise summary of literature produce on aforementioned two design categories.

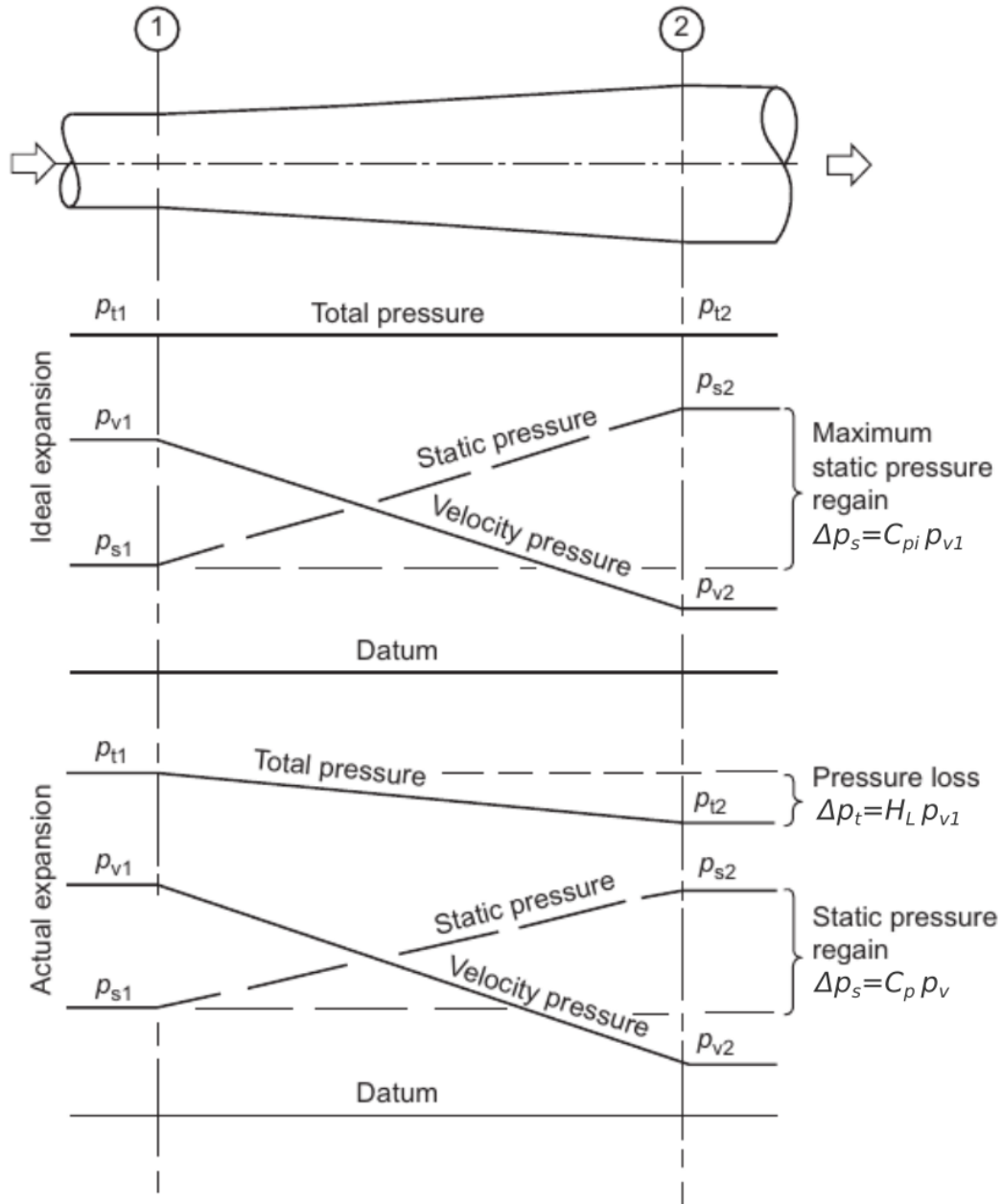


Figure 2.1: Ideal and actual pressure distribution in a conical diffuser from [Legg \[2017\]](#)

[Gibson \[1910\]](#) and Eiffel were one of the first experimental researcher to produce these performance graphs solely based on the opening angle (2θ), area ratio (AR) and the length of the diffuser (x/R). Their results were complementary as the

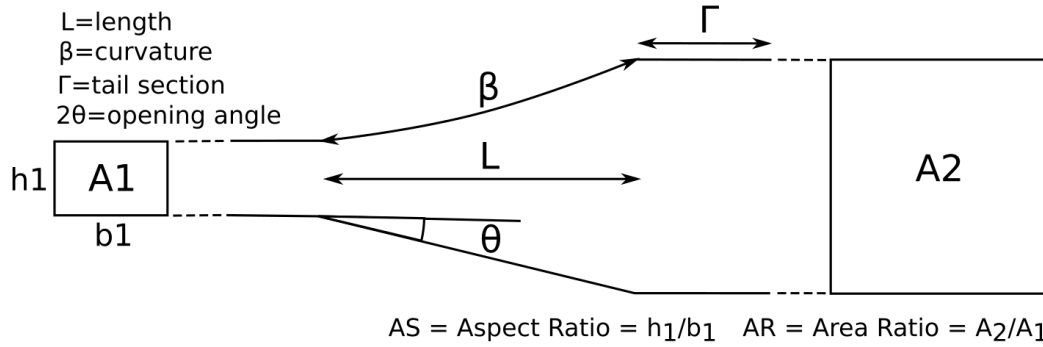


Figure 2.2: Schematic representation of the various diffuser geometrical parameters

area ratios between the inlet and outlet of the diffuser used in their work were different (Fig.2.3). Moreover Gibson [1910] manufactured twenty-five different wood diffusers to extensively investigate the effect of the ‘pipe’ cross-section geometry (eg. square, rectangular and circular) in conjunction with different opening angle ranging from $2\theta \in [3^\circ - 180^\circ]$ on the head losses monitored with pressure gauge. The cross-section unsurprisingly has a significant impact on the diffuser’s head losses, the square and rectangular sections are composed of four edges and vertices while the circular section exhibits only one edge, leading the circular section diffuser to reduce its pressure losses by 20%. Kline [1959] provided the correct equations to define the correct area ratio for different cross-sections such as rectangular, conical and annular, he also correlated the expansion angle with the length of the diffuser to generate an optimal line. McMillan & Johnston [1973b] and McMillan & Johnston [1973a] assessed and compared the flow regimes within one low aspect ratio ($AS=0.1$) and one high aspect ratio ($AS=2$). The pressure recovery is greater in the high aspect ratio diffuser. Gibson [1910] and Peters [1931] both understood and demonstrated the importance of the tail section subsequent to exit of the diffuser. The tail section of a diffuser defines either an outlet pipe for circular diffusers or an outlet duct for square and rectangular diffusers. During their experiments, they witnessed that the pressure rise was still ongoing in the tail section. Subsequently, they recommended for the tail section to be at

least between 2 and 6 times the length of the inlet diameter.

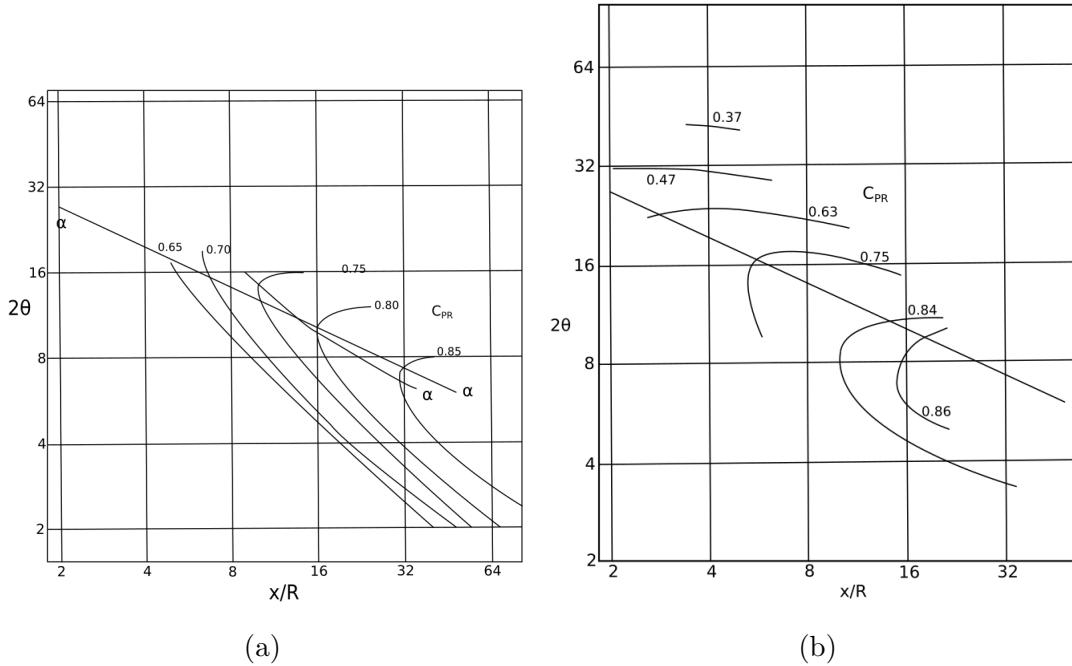


Figure 2.3: (a) Eiffel and (b) Gibson performance curves based on the opening angle 2θ and the length x/R of the diffuser (McDonald & Fox [1966])

The inlet parameters also alter greatly the performance of the diffusers, Waitman *et al.* [1961] performed test on two-dimensional subsonic diffusers where he varied the length of the inlet sections yielding different boundary layer thickness of the diffuser's incoming flow. The increase of the inlet boundary layer thickness leads to an increase of the turbulence level which in turn deteriorate the pressure recovery of the diffuser. It also catalysts the development of stall region within diffusers with a narrow opening angle. Brown *et al.* [1968] installed a vortex generator composed of inclined NACA blades to induced a line of vortices along the wall of the diffuser to interact with the boundary layer of the two-dimensional diffuser. It effectively reduces the pressure losses by 40%. Livesey & Turner [1964] proposed an interesting study on the effect of the velocity profile decay and its boundary thickness on the static pressure recovery within two diffusers. The first diffuser had an opening angle of 4° and area ratio of 1.5 while the sec-

ond second was endowed of an 4° opening and an area ratio of 1.9. The studies show that reducing the apparent Reynolds Stresses also inhibit the development of separated flow.

The inlet condition can be altered further, Klein [1981] research group placed small guide vanes aligned to the streamline of the flow just prior to the inlet of the diffuser, yielding an improvement of the overall performance. Intuitively one could question the beneficial properties of the guide vanes as it adds eddies and transitional reversal flow into the diffuser. These eddies detach sporadically preventing the already present reversal flow pocket to stagnate and developed further as it forces their detachment from the diffuser walls before being washed away by the core flow. More recent studies including Senoo [1974], Furaya *et al.* [1966] connected a blower to prescribe constant suction at the inlet pipe for diffuser with opening angle ranging between $2\theta \in [10, 60]$. The blower leads to a reduction of the pressure losses by 20%. Schubauer & Spangenberg [1948] inserted screens within a diffuser which reduces the turbulent quantities near the wall of the diffuser. It prevents the development of large stall region by enforcing a fast reattachment of the emerging flow separation. Pressure drop occurs through the screen, so the number and distribution of the screens across the diffuser can decrease the performance of the diffuser. Other scientists, including Feil [1964], opted for long guide vanes that compartment the beginning of the diffuser to stabilise and idealise the flow stream. Welsh [1976] installed a star flow control device near the entrance of the diffuser. The characteristic of the star flow such as the thickness of the arm alters greatly the level of turbulence near the wall affecting the pressure recovery. Hoffmann [1981] positioned rods to increase inlet turbulence intensity which increases the pressure recovery by 10%.

The Reynolds number is another parameter that could affect the inlet condition of the diffuser as it influences both the inlet boundary layer thickness at the entry and the growth gradient of the boundary layer within the diffuser and herein the pressure losses (Cockrell *et al.* [1965]). The quantification of the Reynolds influence has been challenging over the year. Gibson [1910]'s experimental results of a given diffuser in which the Reynolds Number varied between 5000 and

250000 did not validate the aforementioned conjectures. It is not a consensus to which every scientist agree on, Détery [2001] considered that for a flow, which is fully turbulent, the effect of the separated flow on the pressure is completely independent from the Reynolds number while McDonald & Fox [1966] believes that this statement is only true for flow with a Reynolds number above 75000. McMillan & Johnston [1973b] conjecture that the performance of the diffuser with high-aspect ratio remains independent from the Reynolds number but conversely when endowed with a low-aspect it is dependent.

2.2 Hairpin Vortices

It is important to denote that the flow structure that emerges and grows within the inner-layer and outer-layer of the boundary-layer are designated using various names including coherent structures, organised motions, energy-containing motion, hairpin-vortices. There has been numerous pioneer works which propose different paradigms to conceptualise the formation and development of these entities including Theodorsen [1952] hairpin-vortex paradigm, Townsend [1976] attached-eddies hypothesis and more recently Adrian *et al.* [2000b] single hairpin-vortex paradigm. Numerous researches are still ongoing in hope to elucidate and quantify the particularities of these phenomenons including : (a) Near-wall streak formation, (b) Bursting process, (c) Mass and momentum transfer between the different region of the boundary layer, (d) Influence of the Reynolds number on the turbulent motions, (e) Taxonomy of the coherent structures types (Robinson [1991]).

Theodorsen [1952]’s paradigm conjecture’s the developed of horseshoe vortices and suggests that the elongation and growth of these hairpins occur at an angle of 45° . This conceptual model also postulates that coherent structure located within the boundary layer are only composed of horseshoes vortices which differ only in scale. Interpreted with a later established coherent structure classification, Theodorsen [1955]’s definition suggests that the horseshoes vortices originate from a spanwise or roller vortices which further extend as shear trans-

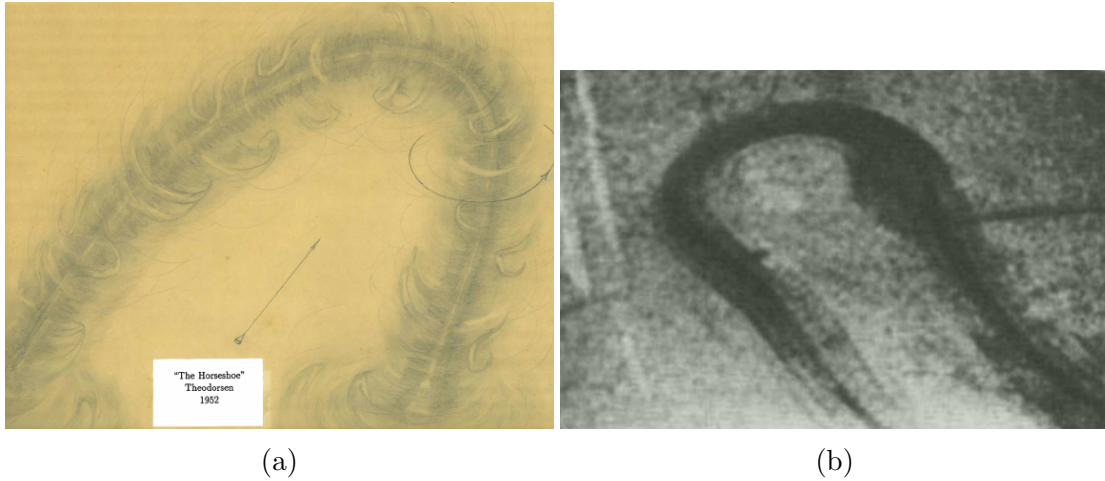


Figure 2.4: (a) Schematic representation of a horseshoes vortex (Adrian [2007]), (b) Experimental picture of a single horseshoe (Bandyopadhyay [1980])

mitting entities. At first, this proposal was supported by Weske & Plantholt [1953]’s (student of Wallace [2016] who first developed the quadrant analysis) experiment in which vortex filaments were generated in a pipe detecting horseshoes vortices using smoke visualisation as displayed in Fig.2.4. It provides clear visualisation of new arch vortices surrounding the horseshoes vortices. Head & Bandyopadhyay [1981], produced further experimental smoke visualisation of coherent structures for Reynolds Number $Re < 17500$, this experiment interestingly observed that at low and moderate Reynolds number flow the horseshoes vortices are the prominent structure forming the edge of boundary layer supporting Black [1968] analysis. It also suggests that this elongation occurs at an angle close to 45° , assuming that vortices emerge and propagate together in a quasi-constant convection speed U_{conv} . The elongation of the coherent structures occurs at an angle of 45°

The swirling phenomenon also described as vortical flow, was first investigated in the 50s, the understanding of this type of angular flow has a wide range of applications including combustion chamber (Binnie [1957]), multiphase separation (eg. water & gaz), heat transfer exchangers, nuclear rocket engines (Rochino & Lavan [1969]).

[Binnie & Teare \[1956\]](#) investigated the pressure and velocity distribution within a convergent vertical nozzle or swirl atomisers used in combustion chambers. The experiment correlates the level of swirl and the emergence of reversal flow which travelled upstream the converging cone to eject from its entry. The separation in this swirl atomiser was later numerically investigated by [Doby *et al.* \[2007\]](#).

[Kerrebrock & Meghreblian \[1961\]](#) studied a vortex flow in order to suitably contain the gaze emanating from a rocket fission while [Backshall & Landis \[1969\]](#) investigated the boundary layer development of a swirling flow within a pipe to avoid local hot spots that sometimes emerge in cooled rocket nozzle while [Mager \[1971\]](#) used induced swirling as thrust control of a rocket nozzle. The swirling flow has for benefit to increase the heat transfer while increasing the pressure drop.

[Kreith & Margolis \[1959\]](#) and [Smithberg & Landis \[1964\]](#) research focused on improving the heat exchanger's design, the performance of heat exchanger can be improved by increase the volume of the device, but it requires a higher pumping power. In these experiments, the tangential momentum was induced into the pipe using coiled wires or twisted strip. The pressure drop was increased when using twisted strip, but overall the rate of heat transfer per unit of area in was greatly improved. Heat exchanger where a swirling device is attached at the entry could be reduced in size. Swirling inlet diminishes the overall flow resistance, [White \[1964\]](#) injected dye into at the entry of a pipe's centerline at a $Re=8800$ into a stationary and rotating pipe. The dye diffused quite rapidly within the stationary while being radially conveyed into the rotating pipe. This experiment also introduces a linear correlation between the reduction of the pressure losses and the increase of the rotational speed for $Re \in [4000, 9000]$. Nevertheless, the axial velocity distribution remains logarithmic from the wall to the core flow when a tangential momentum is added with a twisted pipe ([Backshall & Landis \[1969\]](#)).

Analytical predictions were also developed to approximate the swirling decay along a pipe channel. [Rochino & Lavan \[1969\]](#) solves the swirl equation in conjunction with the uses Taylor's modified transport theory and the Karman's similarity hypothesis to impose the correct turbulence and eddy diffusivity in the

Area Ratio, AR	Opening Angle, 2θ , degrees					
	4.0	6.0	8.0	12.0	15.8	31.2
1.3	$\frac{0.35}{0.38} \frac{0.38}{0.38}$	$\frac{0.36}{0.35} \frac{0.33}{0.34}$	$\frac{0.38}{0.41} \frac{0.39}{0.40}$			
1.64	$\frac{0.50}{0.53} \frac{0.52}{0.53}$	$\frac{0.51}{0.59} \frac{0.52}{0.54}$	$\frac{0.51}{0.53} \frac{0.52}{0.52}$	$\frac{0.47}{0.51} \frac{0.48}{0.49}$	$\frac{0.42}{0.47} \frac{0.44}{0.45}$	
2.43	$\frac{0.66}{0.66} \frac{0.63}{0.64}$	$\frac{0.66}{0.74} \frac{0.71}{0.73}$	$\frac{0.63}{0.74} \frac{0.66}{0.70}$	$\frac{0.54}{0.70} \frac{0.54}{0.66}$	$\frac{0.48}{0.66} \frac{0.64}{0.65}$	$\frac{0.33}{0.39} \frac{0.28}{0.31}$
4.48	$\frac{0.77}{0.93} \frac{0.92}{0.93}$	$\frac{0.77}{0.92} \frac{0.91}{0.96}$	$\frac{0.75}{0.93} \frac{0.89}{0.91}$	$\frac{0.62}{0.89} \frac{0.82}{0.85}$	$\frac{0.55}{0.80} \frac{0.64}{0.69}$	$\frac{0.35}{0.38} \frac{0.24}{0.28}$
8.27			$\frac{0.80}{0.98} \frac{0.94}{0.96}$	$\frac{0.67}{0.95} \frac{0.86}{0.91}$	$\frac{0.60}{0.90} \frac{0.76}{0.83}$	$\frac{0.35}{0.46} \frac{0.34}{0.35}$

C_{PR}	C_{PRS1}
C_{PRS2}	C_{PRS3}

C_{PR} : Pressure recovery without swirling inlet
 C_{PRS1} : Pressure recovery with swirling inlet S1
 C_{PRS2} : Pressure recovery with swirling inlet S2
 C_{PRS3} : Pressure recovery with swirling inlet S3

Figure 2.6: Swirling inlet impact on the performance of numerous conical diffusers (McDonald *et al.* [1971])

system. The decay of the swirl was faster for low Reynolds and high swirling number similar findings were observed by Kreith & Sonju [1965].

McDonald *et al.* [1971] prescribe three different types of swirl into conical diffuser of various dimension and observed improvement of their performance as shown in Fig.2.6. Similarly to Binnie [1957], the tangential velocity in conical diffuser prevented the development of large reversal in conical diffusers flow field (Clausen *et al.* [1993]). So [1967] and Okhio *et al.* [1983] experiments showed that for high swirling numbers can enforce the development the center of stagnant reversal bubbles the conical diffuser.

Chapter 3

Hydro3D Numerical Framework

3.1 Governing-Equation

The numerical representation of fluid mechanics phenomenon relies on discretisation methods to resolve the Navier-Stokes equations. The continuity and momentum set of equations correspond to Newton's second law ($\vec{F} = ma$) for fluid motions. In near-field CFD research, most cases are investigated in 4 dimensions consisting of a three-dimensional spatial referential and time referential. The complexity of solving the momentum equations (Eq.3.1) and continuity equation (Eq.3.2) prevents analytical and smooth solutions, herein it is most accurately approximated using a discretised numerical framework. Over the last 50 years, the digital revolution exponentially increased the development rate of Computational Fluid Dynamics (CFD) research. It has become an invaluable tool for numerous research and industrial fields. Research on incompressible flow has been supported by three main CFD turbulence models: the Reynolds-Average Navier-Stokes (RANS), the Large Eddy Simulations (LES) and the Direct Numerical Simulation (DNS).

$$\underbrace{-\nabla p + \mu \nabla^2 \vec{u} + \rho \vec{f}}_{\vec{F}} = \underbrace{\rho}_{\text{m}} * \underbrace{\left(\frac{\partial \vec{u}}{\partial t} + (\vec{u} \cdot \nabla) \vec{u} \right)}_{\vec{a}} \quad (3.1)$$

$$\nabla \cdot \vec{u} = 0 \tag{3.2}$$

where ∇p represent the pressure gradient, $\mu \nabla^2 \vec{u}$ the internal stresses in between the layer of the fluid, \vec{f} is the external forcing including the IBM forcing, $\partial \vec{u} / \partial t$ correspond the local acceleration while $(\vec{u} \cdot \nabla) \vec{u}$ is the convective acceleration.

DNS is the only CFD model to resolved all the turbulence spectrum up to the Kolmogorov microscales, considered the smallest scales in turbulent flows. It is also the most demanding in computational power thus it mostly used for research application with moderate Reynolds Number flow condition. Meanwhile, both RANS and LES models require additional eddy models to account for the generation of turbulence that mathematically corresponds to the Reynolds stress tensor. RANS is the most widely used mathematical model in industry as it requires low computational power, this model does not resolve any turbulence scale, instead it uses two additional turbulence equations such as $\kappa - \omega$ and $\kappa - \epsilon$. The explanation of these equations and their respective assumption are not attempted in the scope of this thesis as only LES simulations are employed throughout this research.

Throughout this thesis, the in-house LES software Hydro3D developed by [Stoesser, 2001] is used to investigate the flow separation behaviour under different inflow condition and diffuser geometries. The LES is defined as a filtered mathematical model that resolves the flow turbulence and dissipating scale larger than its filter cutoff corresponding to cell volume $\Delta = (dx * dy * dz)^{1/3}$. Scales smaller than the spatial filtering are generated using SubGrid-Scale (SGS) models. The SGS model is based on the Boussinesq hypothesis, which states: *"small-scale turbulent stress should be linearly proportional to the mean strain rates"*. This chapter details Hydro3D functionalities, implementation, and governing principles, while the SGS process is further developed in Section 3.5. In hope to facilitate reader understanding, the next sections enumerate and explains the underlying principle embedded in Hydro3D Framework following the chronological timeline of a

simulation.

3.2 Domain Decomposition and Parallel Computing

The expensive computational cost of high resolution LES simulations requires a parallel framework to efficiently complete the simulations using multiple nodes of a High Performance Computer (HPC) cluster. Sharing of the computational loads is provided and optimised in Hydro3D through a hybrid parallel strategy combining two parallel protocols: Message Passage Interface (MPI) and Open Multi-Processing (OpenMP). This hybrid framework contributes to the reduction of memory overhead requirement of multiple simultaneous processes. The MPI processes enable the transfer of information between the different cores of a cluster while OpenMP Threads share and distribute the core memory across the system to efficiently perform a single targeted task. The OpenMP routine is used to calculate the delta interpolation function and to distribute the Lagrangian forcing onto the Eulerian markers in the immersed boundary method algorithm presented in [3.4](#).

Prior to the execution of the computational loop that discretise and solves governing equations (Eq.3.1) to monitor and study the flow development for a pre-defined temporal length, Hydro3D initialises the MPI Framework and segments the entire computational domain into smaller sub-domains. The spatial integrity of these sub-domains is evaluated before being allocated across the nodes employed for the simulation. The size of the sub-domains are extended from 1 to 4 layers of ghost cells, each face's ghost-cell layers receive and hold the instantaneous fluid properties of the neighbour joint cell face. The ghost layers location determines if it receives the flow information (u,v,w,p etc) from the face of the previous or preceding cell. The ghost cell layers provide the necessary spatial information to enable an accurate flow approximation within a sub-domain using numerical methods such as central-difference. It is through this system of ghost cells in conjunction with the MPI framework that the continuity of the

Eulerian field is ensured. The MPI framework uses numerous routines including `MPI_BROADCAST`, `MPI_SEND`, `MPI_WAIT`, `MPI_RECV` to transfer specific information in between the relevant sub-domains. The MPI can also collect an information from all sub-domains and performed algebraic operation including product and sum using `MPI_ALLREDUCED`. This routine is for instance used in the mass-conservation assessment or to determine the variable time step of the simulations. The MPI Framework is widely used for the initialisation and execution of core methods such as Level-Set-Method (LSM), Lagrangian-Particle-Tracking (LPT) and Immersed Boundary Method (IBM) and the Fractional-step method detailed in Sect.3.6. The OpenMP Framework is used exclusively in the calculation of the delta function in the IBM presented in Sect.3.4.

3.3 Boundary Condition

After the parallel framework is established, the initial velocity field is imposed across all computational cells of the sub-domains at time t_0 . The development of the flow field within the computational domain of Hydro3D relies on a momentum driven strategy. This momentum is prescribed through the different boundary condition faces of the domain (east,west,north,south,top,bottom). Inlet boundaries can be set up as a uniform flow, a power law to represent the profile of a open-channel incoming flow, which enables a faster convergence of the flow field. The Outlet boundaries options includes the Neuhmann or Convective boundary conditions, and the non-slip condition is used to simulate the presence of a wall. The representation of a channel bed can also be achieved with different log-law conditions available in Hydro3D. To ensure mass conservation within the computational system, the inlet flow mass and outlet flow mass are calculated at each time step. If the mass difference is not null a mass ratio corrector is applied onto the inlet and outlet sub-domains. The periodic boundary condition was used in the precursor simulations of every research cases presented in this thesis.

The periodic boundary pairs the inlet and outlet sub-domains, and the pairs exchange their boundary conditions at each time step, simulating an infinity pipe

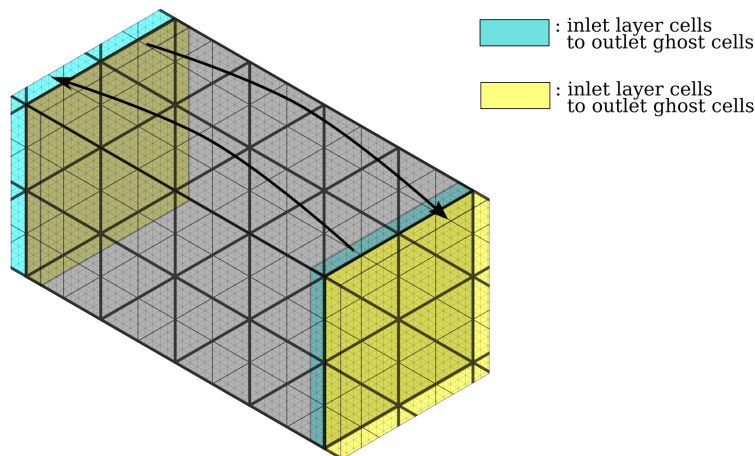


Figure 3.1: Schematic representation of the periodic boundary condition

or duct channel through this synthetic loop. Fig.3.1 represent a computational domain with a periodic condition between the west and east boundaries. The first two cells layer (YZ) of the inlets sub-domains are transferred onto the ghost cells of their paired outlet sub-domains, inversely the last two layers (YZ) of the outlet sub-domains are shared onto the ghost cells of their paired inlet sub-domains. This synthetic loop shortens the computational domain length, which in turn reduces the computational cost while providing faster convergence of the flow field towards accurate statistical properties. Similarly to the inlet and outlet paired condition, the mass conservation is assessed and adds a pressure forcing to correct the mass deficiency if one is present.

The Precursor Inlet consists of two distinctive parts. First, the flow instantaneous properties of the cross-section of a computational domain (eg.pipe or duct) is extracted and exported when the first order-statistic and second order statistic are in good agreement with the inlet experimental data. The user predefines the number of steps to extract, which usually range between 1-2 Flow Through Passage (FTP) to have a large enough sample to accurately represent the time-averaged properties of the inlet flow. A single data file represents the partial instantaneous information of the cross-section of a specific time step. Secondly, these instantaneous data files are prescribed as inlet boundary conditions provid-

ing the driving momentum to the main simulation of the rectangular and conical diffusers.

A methodology to prescribe a swirling inlet was developed and implemented specifically for the conical diffuser case in Chapter 5. Several experimental researchers have introduced numerous swirling generators including propeller devices [Bali & Sarac, 2014], static guide vanes [Yilmaz, 1999], rotating pipe swirling device [Najafi *et al.*, 2005] and tangential injection slots [Chang, 1994]. These swirling generator mechanisms often entail complex mechanical parts and provide limited geometrical information, therefore it is challenging to accurately represent these geometry as a IBP cloud. For this reason, the swirling boundary methodology solely relies on accurately prescribing the tangential and radial velocity components exiting the swirling generator devices. In the case of a swirling pipe inlet, the tangential velocity is specified as a function of the ratio between radial position over the pipe radius (Fig.3.2). Using this method any type of swirl including solid-body (SB), concentrated vortex (CV) and jet wall (JW) swirling [Steenbergen & Voskamp, 1998] can be prescribed into Hydro3D.

$$\begin{bmatrix} V_r \\ V_t \end{bmatrix} = \begin{bmatrix} \cos(\theta) & \sin(\theta) \\ -\sin(\theta) & \cos(\theta) \end{bmatrix} \begin{bmatrix} v \\ w \end{bmatrix} \quad (3.3)$$

As previously stated at the beginning of this section Hydro3D uses a Cartesian spatial referential, while most of the experimental and numerical studies on conical diffuser use Cylindrical spatial coordinate. The implementation of a new cylindrical coordinate mesh system into Hydro3D would have required intensive programming. Instead, the Cylindrical velocities (V_x, V_r, V_t) prescribed as inlet boundary condition are transformed into Cartesian velocities using a Rotation matrix (Eq.3.3).

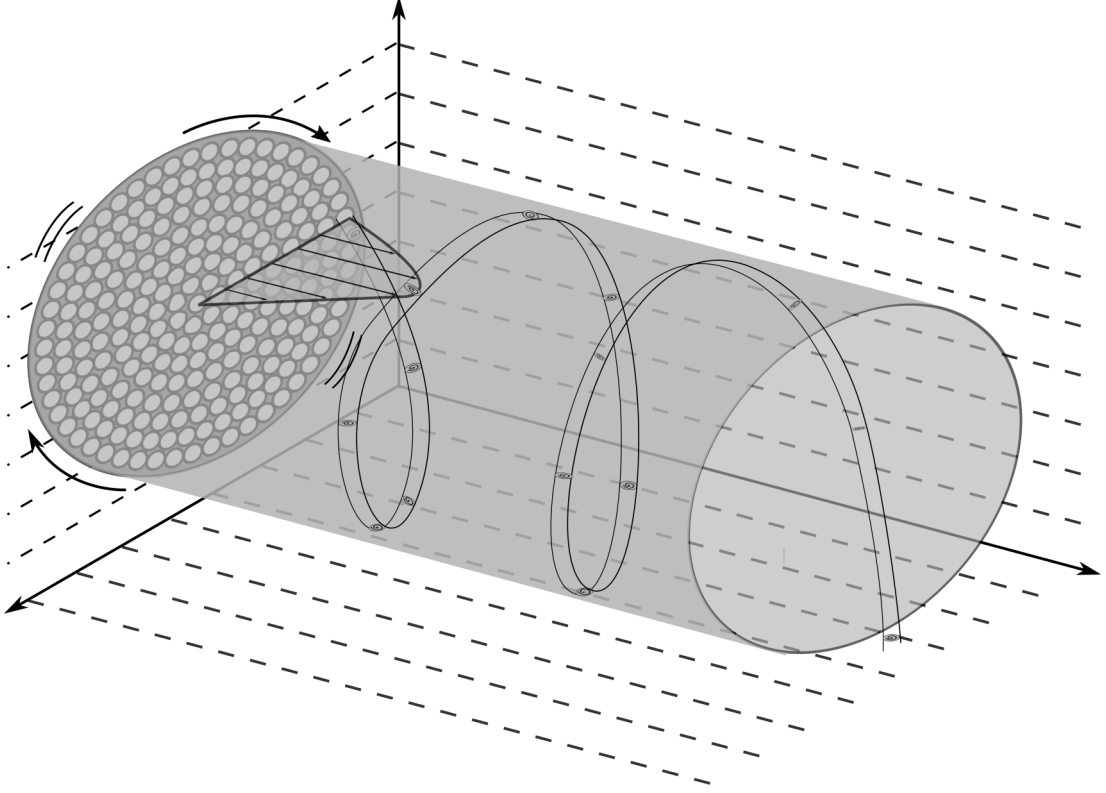


Figure 3.2: Representation of a tangential velocity exiting a swirling generators

$$\begin{bmatrix} v \\ w \end{bmatrix} = \begin{bmatrix} \cos(\theta) & -\sin(\theta) \\ \sin(\theta) & \cos(\theta) \end{bmatrix} \begin{bmatrix} V_r \\ V_t \end{bmatrix} \quad (3.4)$$

Inversely once the divergence velocity field (Eq.3.25) is calculated, the instantaneous Cartesian velocities are transformed into Cylindrical velocities using the inverse of the Rotation matrix (Eq.3.4). Subsequently, the first and second order statistics of the cylindrical velocity field are computed and exported by Hydro3D.

3.4 Geometry: Immersed Boundary Method

The Immersed Boundary Method (IBM) was first established in the field of biomechanical medicine by [Peskin \[1972\]](#), who developed this methodology to investigate blood flow behaviour through an artificial heart valve. The IBM is a non-grid fitting or non-body conformable method meaning that the solid boundary surface does not have to coincide with the computational grid. [Peskin \[1982\]](#) method was first applied to a two-dimensional computation domain at a low Reynolds number, it generated great interest from research community, which further developed and improved the IBM, broadening its application onto three-dimensional flow field problems during the last decade. The IBM constitutes a cheap and fairly accurate alternative in representing solid boundary within a computational domain. Moreover, this method is largely versatile as it can be combined with any type of mesh ranging from Staggered Cartesian Mesh (Hydro3D) to Unstructured Triangular mesh. An organised cloud of Lagrangian points constitutes the immersed body surface interface within the computational domain. Subsequently, the no-slip condition and pressure condition is enforced at each Lagrangian marker (L) using a forcing term as part of the external forcing in the Navier-Stokes equations [3.1](#).

There is three different forcing methods to enforce the no-slip condition at the Lagrangian IBPs: 1] Feedback Forcing, 2] Penalty method, 3] Direct Forcing. [\[Iaccarino & Verzicco, 2003\]](#) provides a detailed description of the governing equation of each method and depicts that the Feedback Forcing and Penalty method present stiffness constraint onto the governing equation [3.1](#) substantially increasing the computational cost when the geometry is complex. For these reasons, the direct forcing was implemented in Hydro3D. The direct forcing methods consist of a multi-step predictor-corrector procedure: first a predicted Eulerian velocity field (u) is calculated which is in turn transferred to the Lagrangian geometry points using the interpolation delta function (δ). Depending on the kernel of the delta function, the Lagrangian marker receives information from 3-5 Eulerian neighbours in all three directions to obtain it's interpolated velocity U_L :

$$U_L = \sum_{i=1}^{n_e} u_{ijk} \cdot \delta(x_{ijk} - X_L) \cdot \Delta x_{ijk} \quad L = 1, \dots, N_l \quad (3.5)$$

where $x_{ijk} - X_L$ denotes the distance between the Eulerian grid points and the Lagrangian Immersed Boundary Points (IBP) and Δx_{ijk} correspond to the Eulerian cell volume. The calculation method of the kernel plays important role in the interpolation accuracy, in some case the kernel leads to spurious oscillation forces. Hydro3D uses Yang kernel (ϕ) which smooth and reduce the force oscillations.

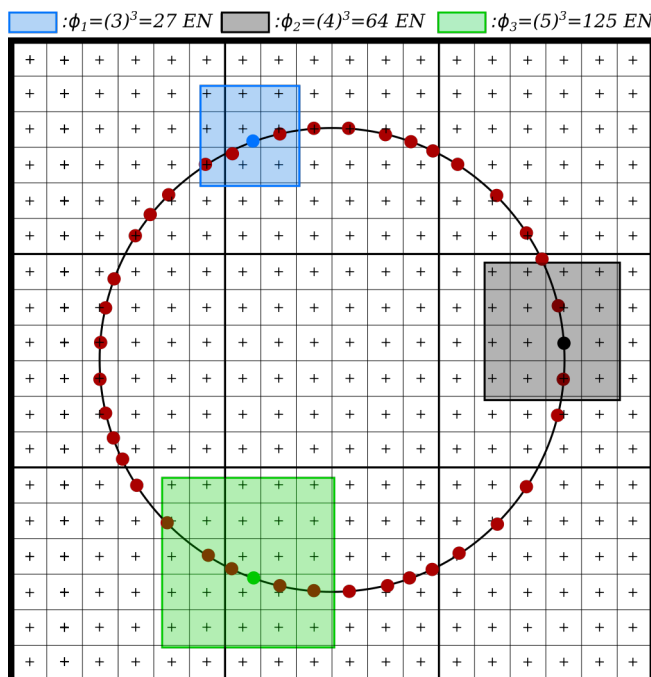


Figure 3.3: 2D representation of IBP Lagrangian points and their respective ϕ interpolation from Eulerian grid point neighbours

$$\delta(x_{ijk} - X_L) = \frac{1}{\Delta x_{ijk}} * \phi\left(\frac{x_{ijk}}{X_L}\right) * \phi\left(\frac{x_{ijk}}{Y_L}\right) * \phi\left(\frac{x_{ijk}}{Z_L}\right) \quad (3.6)$$

Once the interpolation is complete, the direct forcing method calculates the Lagrangian forcing F_L to exert on the Eulerian neighbours of each Lagrangian IBP

to ensure a no-slip condition at this precise location. The force corresponds to the difference between the desired velocity U_L^* usually equal to zero and the aforementioned interpolated velocity U_L acting at that location.

$$F_L = \frac{U_L^* - U_L}{\Delta t} \quad L = 1, \dots, N_L \quad (3.7)$$

The last step consists in feeding back and interpolating the Lagrangian forcing onto its Eulerian neighbours cells and obtain the Eulerian forcing, f used in Navier-Stoke equation (Eq.3.1). The same delta interpolation function is used to distribute the Lagrangian force F_L proportionally to the distance between the Lagrangian location and its Eulerian neighbours location.

$$f_i = \sum_{L=1}^{n_L} F_L \cdot \delta(X_L - x_i) \cdot \Delta V_L \quad i = 1, \dots, N \quad (3.8)$$

where ΔV_L is the Lagrangian volume, in order to improve the stability of the method, [Uhlmann, 2005] the following equilibrium:

$$\sum_{ijk=1}^{N_e} f(i) \Delta x_{ijk} = \sum_{L=1}^{N_L} F_L \Delta V_L \quad (3.9)$$

which means that the further the neighbour is from the Lagrangian point the smaller the Lagrangian cell will be. Finally, the final Eulerian field (\tilde{u}^*) is calculated by correcting the initial (u^*) Eulerian field with its Eulerian forcing ($f\Delta t$) (Eq 3.8):

$$\tilde{u}^* = u^* + f\Delta t \quad (3.10)$$

In complex geometries, the user can reduce the residual velocity within the IBP by running the multi-step predictor corrector procedure numerous times to increase

the accuracy of the forcing.

3.5 Sub-grid scale model

The Lagrangian location of IBP cloud to represent the geometry was allocated to their respective domain in association with the transfer of their weight to their surrounding Eulerian point. The main challenge of the different Navier-Stokes computational models lies in providing an accurate energy dissipation rate to the flow field system.

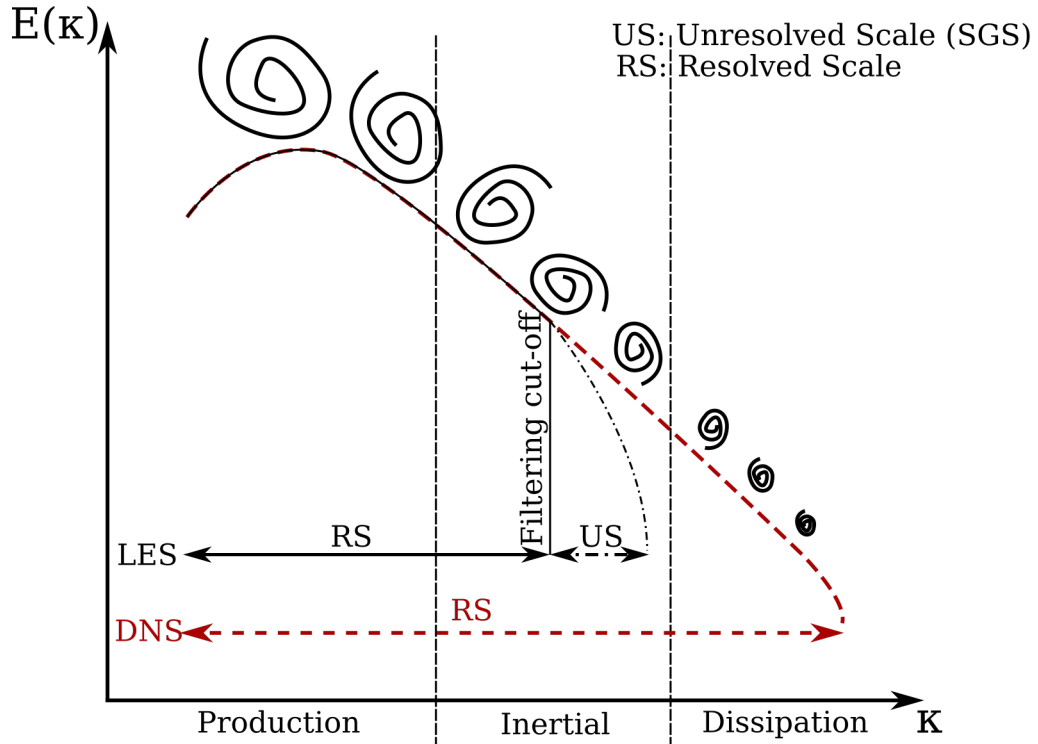


Figure 3.4: Komogolov's Energy Cascade

The full turbulent flow energy spectrum is characterised by three distinctive zones: (I) the production range relies on the amount of kinetic energy and dissipation rate present in the flow, it is the origin and sources of large scales eddies, (II) the inertial range physically describes the shedding and diffusion of those large structures following Kolmogorov decay law with the $-5/3$ slopes, which depend

on the size of the turbulent structures and dissipation's rate, (III) the dissipation range portray the total depletion of the turbulent structure which is dictated by the viscosity of the flow and the dissipation range. As previously stated the LES mathematical model does not resolve the eddies smaller the simulation cut off size. Instead, the dissipation rate is generated through the sub-grid scale tensor τ_{ij} , significantly reducing the computational cost compared to DNS. Prior to the resolution of the velocity field for the next time step using the fractional step method, the SGS model calculates the turbulent viscosity (ν_t) also referred to as eddy viscosity.

$$\tau_{ij} = \tau_{ij}^a + \frac{1}{3}\tau_{kk}\delta_{ij} \quad (3.11)$$

The first term τ_{ij}^a represents the anisotropic component while the second τ_{kk} corresponds to isotropic component linked to the Kronecker delta δ_{ij} . Hydro3D is endowed with three different SGS models: the Smagorinsky-Lilly is subjected to the von Driest damping, One-Equation and Weighted Essentially NonOscillatory model (WALE). These models enforce additional dissipation rate with distinctive methods to generate the turbulent/eddy viscosity ν_t . In turn this artificial velocity is employed to calculate the anisotropic sub-grid stress tensor:

$$\tau_{ij}^a = -2\nu\overline{S_{ij}} \quad (3.12)$$

The first SGS model was developed by Smagorinsky in 1963 to approximate the turbulent viscosity as:

$$\nu_t = (C_s\Delta)^2 * |\sqrt{2\overline{S_{ij}} * \overline{S_{ij}}}| \quad (3.13)$$

$$\overline{S_{ij}} = \frac{1}{2} \left(\frac{\partial \overline{u_i}}{\partial x_j} + \frac{\partial \overline{u_j}}{\partial x_i} \right) \quad (3.14)$$

C_s refers to the Smagorinsky constant ranging between 0.1-0.3 depending on the investigated computational case. In Hydro3D the default value is set to 0.1, $\Delta = (dx dy dz)^3$ corresponds to the filter mesh size while S_{ij} is the resolved rate of strain.

The WALE SGS model was first introduced in 1998 by [Ducros *et al.* \[1998\]](#), [Nicoud & Ducros \[1999\]](#). It was specially developed to overcome the difficulties encountered by the research and industrial corpus in generating physically accurate small eddies. Specially in the field of turbo-machinery and aeronautics, where the rotational geometries have a significant impact on the energy dissipation and its surrounding flow field. The WALE improves its tensor framework in combining both the resolved strain rate and the resolved rotational rate, accounting for the possibility of $\nabla \vec{U} \neq 0$. In contrast to the Smagorinsky model, the WALE method does not require any damping near the solid wall. This enables to predict the most accurate behaviour of eddy viscosity near solid surfaces, providing a clear advantages when using the Immersed Boundary Method, which does not impose a grid fitting solid surfaces.

$$\nu_t = (C_w \Delta)^2 * \frac{\sqrt[3]{S_{ij}^d S_{ij}^d}}{\sqrt[5]{S_{ij} S_{ij}} + \sqrt[2.5]{S_{ij}^d S_{ij}^d}} \quad (3.15)$$

where C_w corresponds to the WALE constant assumed to be 0.46, the turbulent viscosity is determined from the resolved strain rate S_{ij} and S_{ij}^d the traceless symmetric part of the square velocity gradient tensor $\overline{g_{ij}} = \partial u_i / \partial x_j$.

$$S_{ij}^d = \frac{1}{2} (\overline{g_{ij}}^2 + \overline{g_{ij}}^2) - \frac{1}{3} \delta_{ij} \overline{g_{kk}}^2 \quad (3.16)$$

The previous term can be developed as a function of the strain rate S_{ij} and rotation rate $\Omega_{ij} = 1/2(\partial u_i/\partial x_j - \partial u_j/\partial x_i)$, S_{ij}^d is implemented into Hydro3D using the following form:

$$S_{ij}^d S_{ij}^d = \frac{1}{6} (S^2 S^2 + \Omega^2 \Omega^2) + \frac{2}{3} S^2 \Omega^2 + 2\bar{S}_{ik}\bar{S}_{kj}\bar{\Omega}_{jk}\bar{\Omega}_{ki} \quad (3.17)$$

The one-equation model solves the transport equation to unveil the kinetic energy present in the sub-grid scale in order to calculate the turbulent viscosity. It is the only method that incorporate physical processes in term of production, convection and dissipation of k_{sgs} :

$$\nu_t = C_k \Delta \sqrt{k_{sgs}} \quad (3.18)$$

$$\frac{\partial k_{sgs}}{\partial t} + u_j \frac{\partial k_{sgs}}{\partial x_j} = -\tau_{ij} \frac{\partial u_i}{\partial x_j} - C_c \frac{k_{sgs}^{3/2}}{\Delta} + \frac{\partial}{\partial x_j} \left[(\nu_t + \nu) \frac{\partial k_{sgs}}{\partial x_j} \right] \quad (3.19)$$

3.6 Time and Spatial Discretisation

The LES spatially filtered Navier-Stokes equations in [eq](#) in its continued mathematical form. The computational resolution of the velocity and pressure field over time requires a framework to discretise the Navier-Stokes equations both spatially and in time. Prior to this resolution, the stability criterion or Courant-Friedrichs-Levy (CFL) number needs to be determine associated with the size of the time step. Numerically it means that the size of the time step enquire the flow particle to computed at every cells along its streampath. The CFL need to fulfil the condition $C \in [0, 1]$.

$$C = \Delta t \left(\sum_{i=1}^3 \frac{u_i}{\Delta x_i} \right) \leq (C_{max} = 1) \quad (3.20)$$

Hydro3D offers both variable and fixed time step, in this thesis most simulations were ran using the variable time step based on $C = 0.5$. Hydro3D time discretization is executed using the fractional-step method based on the projection method which was first developed by (Chorin [1968]). While other methods such SIMPLE and PISO have their velocity and pressure computations coupled, Hydro3D staggered Cartesian grid in conjunction with the fractional step offers a decoupled velocity and pressure computation. In Fig.3.5, the velocity u, v, w and pressure p are resolved at different locations of the staggered grid, the velocities are computed on the respective faces of the cell while the pressure is calculated at the centre of the cell.

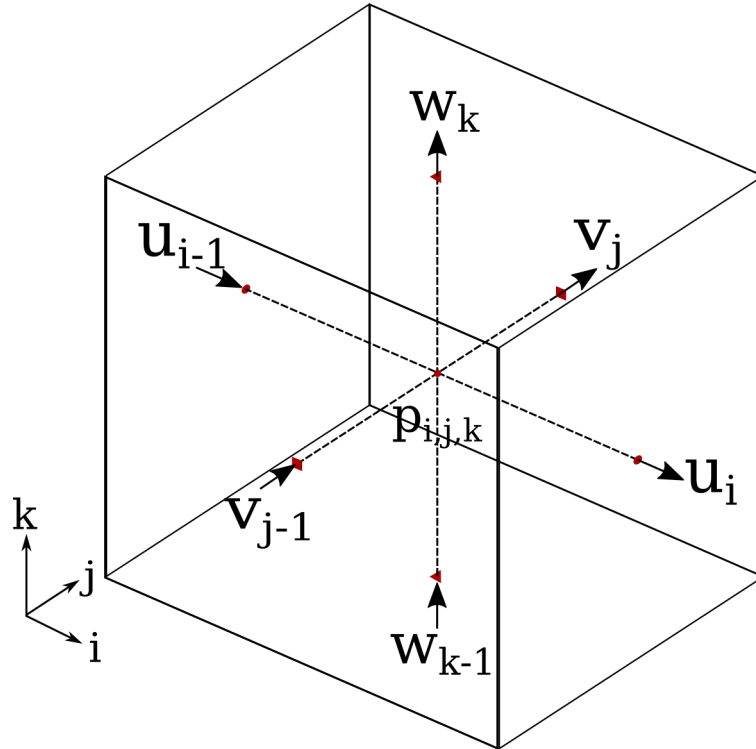


Figure 3.5: Three-dimensional representation of the Cartesian staggered grid

The fractional-step method is composed of two distinctive steps, the first step focuses on the calculation of the intermediate non-divergence velocity field u_i^* . The second step projects the intermediate velocities onto the divergence free vector field.

$$u_i^{*,n+\beta} = u^n + \frac{\Delta t}{\beta} \left[R^{n+\beta} - \frac{\partial p^{n-\beta}}{\partial x_i} \right] \quad (3.21)$$

where β is the substep index depending on the convection scheme, varying from 1 to 3.

$$R = -\frac{\partial(u_i u_j)}{\partial x_j} + \left(\frac{1}{Re} + \nu_t \right) \frac{\partial^2 u_i}{\partial x_i \partial x_j} \quad (3.22)$$

The non-divergence field is also subjected to the external forcing f (rhs of Eq.3.1) which include the gravity force and the immersed boundary force:

$$\tilde{u}^* = u^* + f \Delta t \quad (3.23)$$

The Poisson equation calculates the projection scalar function, δp , this takes into account the velocity increment of the divergence-free field and translates into the pseudo-pressure field:

$$\nabla^2 \tilde{p} = \frac{\nabla \cdot \tilde{u}^*}{\Delta t} \quad (3.24)$$

This Eq.3.24 can be solved using two different methods: the Strong Implicit Procedure (SIP) or the multi-grid method. This pseudo-pressure gradient is subsequently added to the divergence free field acting as a corrector to predict the new velocity field:

$$u^t = u^* - \Delta t \nabla^2 \tilde{p} \quad (3.25)$$

Finally, the new pressure field is computed updating the previous time step with the new pseudo-pressure field:

$$p^t = p^{t-1} + \tilde{p} - \frac{\nu \Delta t}{2} \nabla^2 \tilde{p} \quad (3.26)$$

The final stage of the time-advancement loop of the running simulation is to compute the updated velocity field to the first-order and second order statistic which evaluates the time-averaged flow field and its turbulent fluctuations. Hydro3D exports these quantities in conjunction with multiple other outputs that the user will have selected prior to the simulation.

Chapter 4

Rectangular Diffuser: Influence of the geometrical aspect ratio on flow separation behaviour

4.1 Overview

Flow separation occurs under various flow conditions and environments, mainly when the viscous forces within the boundary layer are overcome by the fluid's momentum forces leading to local detachment of the fluid from the boundary. In turbulent flows, separation leads to the development of coherent turbulent structures and increased dynamic pressure disturbing the reduction in static pressure. The diffuser's expansion generates strong adverse pressure gradients acting against the streamwise velocity of the turbulent boundary layer, and once the velocity reduces to zero, flow detachment takes place. The backflow within the flow separation region acts as an obstructing volume inside the diffuser leading to local acceleration of the flow which affects negatively the diffuser's performance. The separation of the turbulent boundary layer is highly unsteady and three-dimensional in nature challenging both design engineers and the research community in understanding and classifying fluid flows in diffusers.

The lack of sophisticated and non-invasive experimental instrumentation and limited computational resources initially asked researchers to simplify the complexity of the flow separation phenomenon by investigating quasi two-dimensional diffusers. [Obi *et al.* \[1993\]](#) first experimentally (LDV) and then numerically (RANS) investigated the mean flow field of a 10° planar diffuser the flow of which is governed by a distinctive flow separation bubble. Subsequently, [Obi *et al.* \[1999\]](#) provoked an artificial perturbation at the beginning of the diffuser and demonstrated its impact on the detachment and reattachment location of the mean flow separation. [Wu *et al.* \[2006\]](#)'s numerical study provides the structural features of the internal layer located at the flat wall of the diffuser, it is generated by the low-frequency of the turbulent fluctuation. Another planar diffuser with 8° diverging angle was researched by [Törnblom *et al.* \[2009\]](#) in which the time-averaged flow field was monitored and the energy spectra, instantaneous flow and auto-correlations were analysed to reveal the existence of large-scale hairpin vortices. This experimental study subsequently led [Herbst *et al.* \[2007\]](#) to studying the influence of the Reynolds number on the mean-flow separation size and location. The results suggest that the boundary layer has less tendency to separate at the diffuser throat when the Reynolds number is high.

[Cherry *et al.* \[2008\]](#) were the first to develop an experimental methodology to measure accurately the hydrodynamics within two different three-dimensional asymmetric diffusers. This experiment successfully monitored the development and behaviour of a three dimensional flow separation induced by a strong adverse pressure gradient. The expansion part of their first diffuser (D1) and their second diffuser (D2) had the same duct inlet geometry while featuring a different outlet geometry (D1 and D2 are depicted in Fig.4.1). A medical magnetic resonance velocimetry (MRV) method monitored and collected magnetic resonance signals which were then post-processed and transformed into a velocity field. This non-intrusive method provided accurate results of the mean velocity field (+ -5%) and its mean fluctuation (+ -10%). The data set has been instrumental towards the calibration and validation of numerous computational methods and models. [Cherry *et al.* \[2010\]](#) later investigated the flow field and performance of an annu-

lar diffuser consisting of two different inlets, one had a fully developed flow while the other inlet was a wake induced by a row of struts. [Cherry *et al.* \[2008\]](#)'s experiment laid the groundwork for [Grundmann *et al.* \[2012\]](#)'s investigation which induced a different inlet secondary current using a plasma actuator and observed a significant difference in the mean flow-separation size and location which led to an improvement of the pressure recovery of 13-17% .

The first CFD study aiming to reproduce the hydrodynamics in the two diffusers of [Cherry *et al.* \[2008\]](#) was carried out by [Schneider \[2009\]](#), who performed a grid sensitivity analysis from multiple RANS and LES simulations investigating the time-averaged flow field of both D1 and D2. The RANS simulations failed in predicting accurately the location and size of the reverse flow region while the LES results on a fine grid were in good agreement with experimental data. Other studies including [Abe & Ohtsuka \[2010\]](#) and [Jakirlić *et al.* \[2010\]](#) compared the accuracy of hybrid LES/RANS (HLR) models with pure LES in terms of the mean flow separation within the first diffuser D1. These papers revealed that HLR is able to deliver similar results to LES at reduced computational cost as HLR simulations were run on coarser meshes. Additional numerical studies included [Ohlsson *et al.* \[2010\]](#)'s work validated and benchmarked their DNS in terms of turbulence statistics. In a second paper [Malm *et al.* \[2012\]](#) the authors furthered the understanding of the flow separation unsteadiness and the quasi-periodic meandering of the core flow using the backflow coefficient and a power-spectral analysis while revealing coherent structures inherent to flow separation through a POD investigation.

The present paper investigates the influence of the aspect ratio on the development and the hydrodynamic behaviour of the instantaneous flow separation for two different asymmetric rectangular diffusers. The numerical method is validated before the intermittency of the flow separation and its impact on the diffuser performance is evaluated. The coherent structures that trigger the instantaneous flow separation are visualised with the Q criterion and analysed using quadrant analysis.

4.2 Computational set-up

The geometrical set-up of the two diffusers under consideration, namely D1 and D2, is nearly identical to the geometry used in the laboratory experiment carried out by [Cherry *et al.* \[2008\]](#). The experimental geometry contains rounded corners while the numerical possess sharp corners for simplicity similar to [Schneider \[2009\]](#). The two diffusers are composed of four distinctive parts which are illustrated in Fig.4.1: a) first an inlet duct ($x/H \in [-2, 0]$), second the expansion part ($x/H \in [0, 15]$), the third part is the extension or tail section ($x/H \in [15, 27.5]$) and finally the outlet section ($x/H \in [27.5, 37.5]$). Fig.4.1 provides the detailed geometry of both diffusers, the only difference between diffusers D1 and D2 is the aspect ratio of the outlet cross-section of the expansion part of the diffuser, respectively featuring aspect ratios ($AS = h/b$, i.e. the height-to-width-ratio) of 1:1 (D1) or 1:1.34 (D2), respectively. This can be translated into a more comprehensive ratio, the asymmetric expansion ratio (AER) which describes the ratio of vertical expansion rate to the spanwise expansion rate. The diffusers D1 and D2 possess an asymmetric expansion ratio of $AER_{D1} = 4.46$ or $AER_{D2} = 2$, respectively for which significant differences in the development and behaviour of the flow separation is expected.

The Reynolds number of the inlet flows is $Re = 10,000$, based on the average bulk velocity $U_b = 1.0m/s$ in the inflow duct and its height $h = 0.01m$. For the purpose of a fully developed inflow at low computational cost a precursor periodic simulation of the inlet duct is performed separately. A periodic boundary condition in the streamwise direction is used which provides a fully-developed flow field to be provided as inflow conditions into the diffuser domains. As Fig.4.2 suggests first and second order statistic in the converged precursor simulation are in convincing agreement with the experimental data of [Cherry *et al.* \[2008\]](#) and the DNS of [Ohlsson *et al.* \[2010\]](#). Both LES and DNS overestimate slightly the velocity in the centre of the duct, probably because the computational inlet ducts are infinitely long while the experimental inlet duct is rather short. The distribution of streamwise turbulent fluctuations is similar for LES and DNS whereas the experimental data is a bit more scattered, however agreement with the exper-

RECTANGULAR DIFFUSER: INFLUENCE OF THE GEOMETRICAL ASPECT RATIO
ON FLOW SEPARATION BEHAVIOUR

Sim	$\Delta x(m)$	$\Delta y(m)$	$\Delta z(m)$	n_x	n_y	n_z	$N_e(10^6)$	$N_{De}(10^6)$
Precursor	0.0005	0.000125	0.00025	200	320	272	10.24	3.46
Diffuser 1	0.0005	0.000125	0.00025	800	320	320	40.96	30.18
Diffuser 2	0.0005	0.000125	0.00025	800	272	320	39.60	28.93

Table 4.1: Mesh resolution of the different simulation computational domains

iment is generally quite good. In order to provide a fully developed inflow into the main diffuser domain planes of the instantaneous flow are continuously saved at every time step from the precursor simulation and provide instantaneous velocities (u,v,w) at the inlet cross-section of the diffuser. A total of 20,000 time steps are saved corresponding to three flow through passages (FTP) of the entire length of the inlet duct.

The two simulations are performed with the same mesh resolution detailed in Table 4.1 providing the grid spacing (Δ_{xi}) and the number of grid points (n_{xi}) in the three spatial directions, the number of cells of the computational domain (N_E) and the number of cells located within the diffuser flow field (N_{DE}). A grid sensitivity is performed during the calibration of the D1 but is not shown for brevity. Coarser simulations are ran to test different SGS models such as Smagorinsky or the turbulent subgrid scale energy one-equation model including ($\Delta x = 0.015, \Delta y = 0.01, \Delta z = 0.01$) and ($\Delta x = 0.01, \Delta y = 0.0005, \Delta z = 0.0005$) meshes but on coarser grids the detachment of the flow separation occurs too early near the throat of the diffuser leading to large over-prediction of the mean flow separation bubble. The corresponding wall unit for the refined mesh (Table 4.1) used for this study are $\Delta x^+ = 3.2, \Delta y^+ = 1.5, \Delta z^+ = 1.5$ which is very similar to the LES mesh of [Jakirlić *et al.* \[2010\]](#).

The computational domain is divided into 400 sub-domains for the D1 simulation and 384 sub-domains for the D2 simulation. Each sub-domain is surrounded by two layers of ghost-cells containing the flow information of the neighbouring sub-domain herein enabling the numerical approximation of the derivatives at its

RECTANGULAR DIFFUSER: INFLUENCE OF THE GEOMETRICAL ASPECT RATIO
ON FLOW SEPARATION BEHAVIOUR

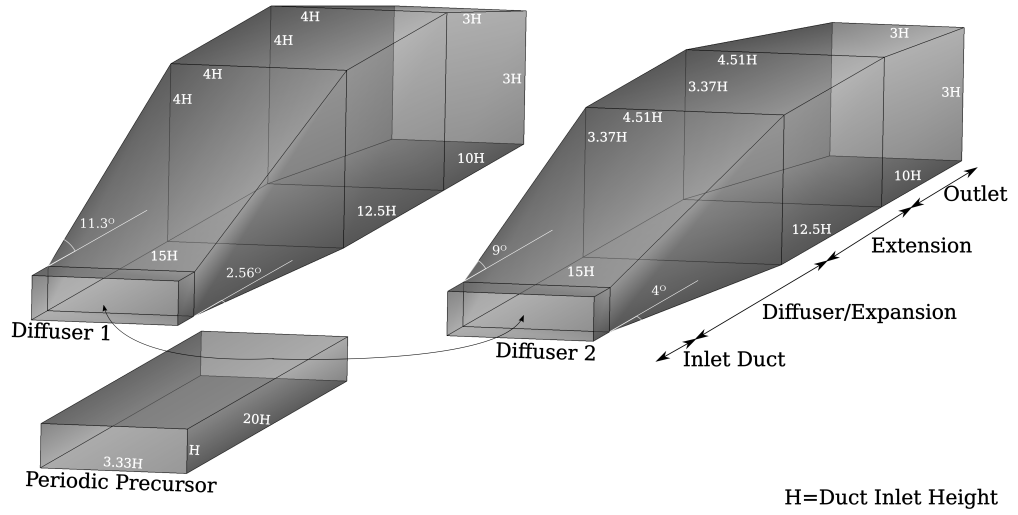


Figure 4.1: Three-dimensional dimensions of the precursor channel and the two asymmetric rectangular diffusers D1 and D2

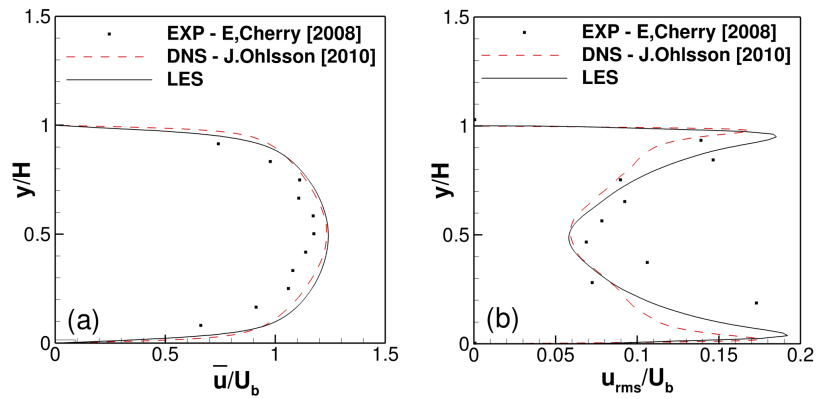


Figure 4.2: Inlet flow conditions: (a) Mean streamwise velocity, (b) Root mean square of streamwise fluctuation

boundaries. The ghost-cell approach in conjunction with the Message Passing Interface (MPI) provides an effective communication between the different sub-domains of the entire computational domain [Ouro *et al.* \[2019\]](#). The simulations are carried out on the Supercomputing Wales cluster using 200 Intel Xeon Gold 6148 cores for 188 hours, which corresponds to 37,600 CPU hours. The numerical stability is ensured with a fixed CFL=0.5 and a variable time step which averages to $dt_{av} = 6.7 \times 10^{-5}$ for D1 and $dt_{av} = 7.1 \times 10^{-5}$ for D2. The flow through passage (FTP) is calculated using of the mean cross-section area and mean velocity of each section of the diffusers, $FTP_{D1} = 1.44s$ and $FTP_{D2} = 1.38s$. The averaged flow field is collected for 25 FTPs while the time-averaged fluctuations are collected for 35 FTPs to ensure the convergence of the flow field within the diffusers. The data used for the instantaneous flow analysis in [Fig.4.10](#) and [Fig.4.11](#) are extracted after 30 FTPs.

4.3 Results and Discussion

4.3.1 Time-averaged flow

The first- and second order statistics of the LES predictions are first validated with the [Cherry *et al.* \[2008\]](#) experimental and the [Ohlsson *et al.* \[2010\]](#) DNS data. In the current paper, the spatial and velocity conventions are consistent with previous studies on these diffusers, (x,u) represents the streamwise direction/velocity, (y,v) corresponds to the vertical direction/velocity and (z,w) denotes the spanwise direction/velocity.

[Fig.4.3a](#) and [Fig.4.3b](#) respectively plot streamwise velocity profiles in the vertical planes located at $z/H = 0.5$ and $z/H = 7/8$ while [Fig.4.3c](#) plots streamwise velocity profiles in the horizontal plane positioned at $y/H = 1/8$. The [Cherry *et al.* \[2008\]](#) experimental data are only available for the vertical planes, however DNS-computed velocity profiles are available for all planes. The LES results of the five profiles along the centre plane ([Fig.4.3a](#)) are all in excellent agreement

RECTANGULAR DIFFUSER: INFLUENCE OF THE GEOMETRICAL ASPECT RATIO
ON FLOW SEPARATION BEHAVIOUR

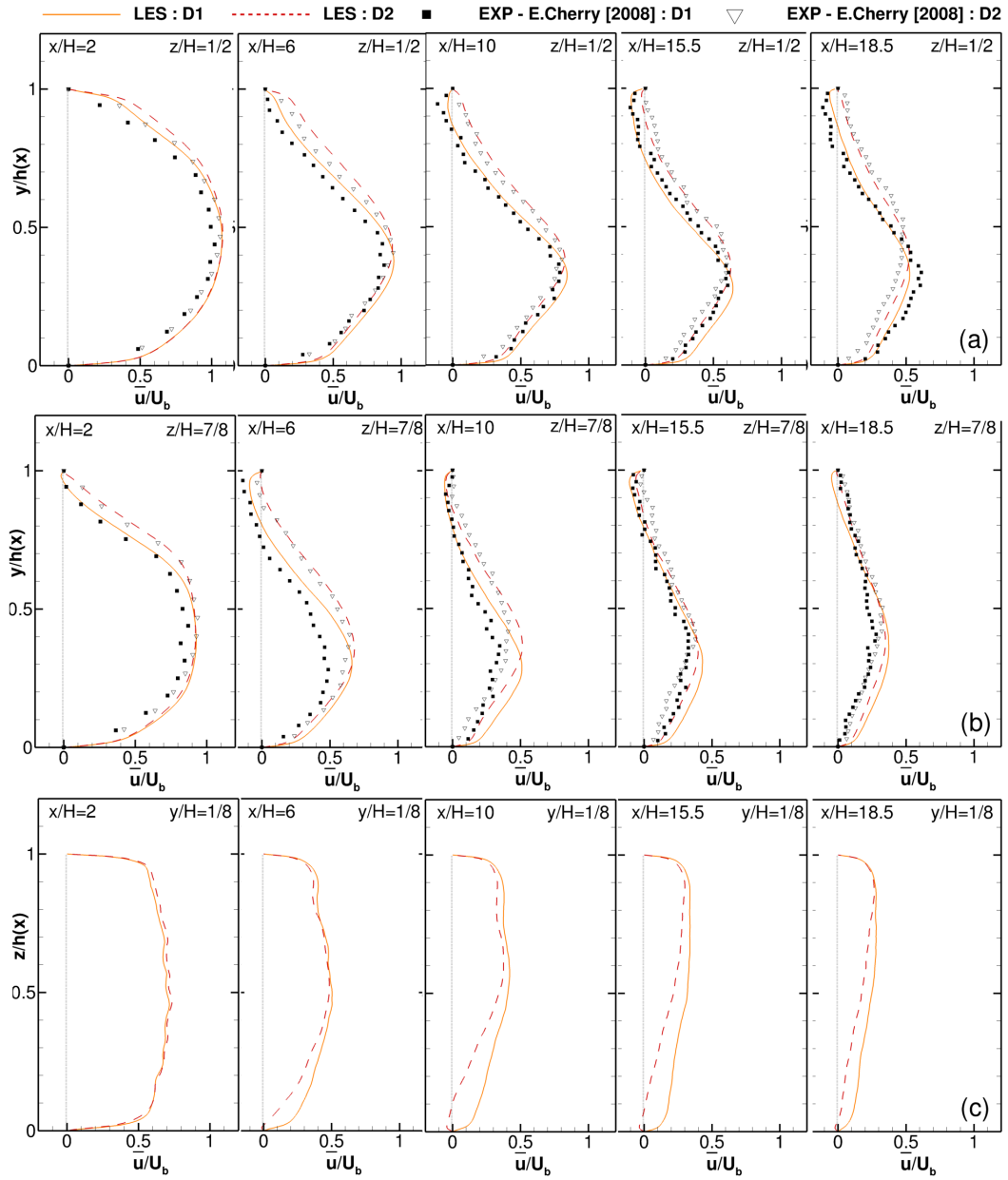


Figure 4.3: Normalised mean streamwise velocity \bar{u}/U_b : (a) Vertical plane $z/H=1/2$, (b) Vertical plane $z/H=7/8$, (c) Horizontal plane $y/H=1/8$

with the experimental data. Peak velocities, flow reversal and boundary layer development predicted by the LES match well the experiment and are within the 5% error of the experimental data. In the second horizontal plane near the wall at $z/H = 7/8$ (Fig.4.3b the time-averaged streamwise velocity profile of D1 at $x/H=6$ and $x/H=10$ features a stronger streamwise core momentum than the experiment, this difference is probably the results of the sharp corners present in the LES diffuser geometries which differs from the rounded-edges of experimental diffuser leading to higher velocities in the LES near the wall. Overall the LES velocity profiles at this location remain in fairly good agreement with the experimental data, accurately representing the size of the backflow region at $x/H=6$, $x/H=10$ and $x/H=15.5$. It is interesting to note that in both diffusers a clear deceleration of the high momentum core due to the adverse pressure gradient is observed reducing the core flow by 50% when reaching the station $x/H=18.5$. In Fig.4.3a an inflection point is depicted in the mean streamwise velocity of D1 at $x/H=6$ evidencing the presence of strong shear flow and separated flow in its vicinity. Inflection points consist of localised loss of momentum in the velocity profile transferred from a nearby low velocity region. This projection is validated as the flow separates at $x/H=10$ in D1, this phenomenon is also observable in D2 but to a lesser extent as it occurs at $x/H=10$ while exhibiting only a very small separated portion near the top wall at $x/H=15.5$. At location $z/H=7/8$ closer to the top right corner of the diffusers, the velocity profiles feature such inflection points much sooner at $x/H=2$ and both flows separate before $x/H=6$. It is interesting to observe that due to the steeper expansion of the top wall in D1 a stronger adverse pressure gradient is present enforcing a faster and larger top separation of the flow compared to D2. It results in a shift of the core and a slight increase in the high momentum region of the flow in D1 demonstrating the higher blockage effect that ensue from the backflow region. Further, in the spanwise direction, see Fig.4.3c, D2 is endowed with a higher side wall expansion revealing a recirculating zone from $x/H=6$ which seems to extend all the way to $x/H=18.5$.

Fig.4.4 presents an iso-surface of $\bar{u} = 0.001$ of the mean streamwise velocity for both diffusers, D1 (a) and D2 (b). It reveals the disparity in location and size of

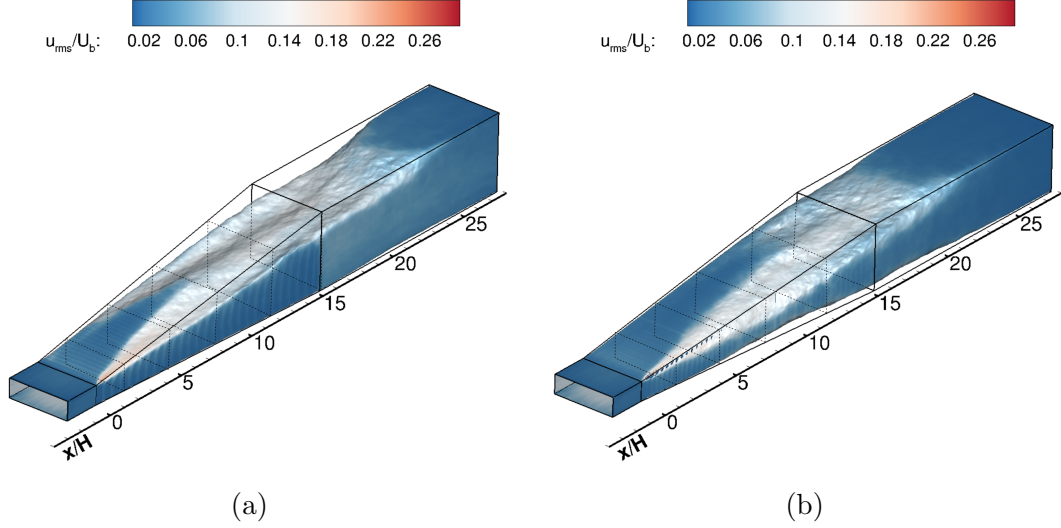


Figure 4.4: Iso-surface of the Flow separation ($\bar{u} = 0.001$) with a normalised root mean square of the fluctuation contour (u_{rms}/U_b) : (a) D1, (b) D2, the dotted rectangles represent the cross-section locations of Fig.4.5

the time-averaged backflow regions between the two diffusers. D1 features only one reverse flow emerging at the throat of the diffuser. It originates in the corner of the top and side walls which induces an abrupt deceleration and growth of the boundary layer which eventually detaches from its wall(s). The backflow region quickly grows diagonally downstream until the middle of the diffuser where it occupies the full width of the diffuser, from that point on the flow separation may nearly be considered two-dimensional as it progresses quasi-uniformly until its reattachment point at $x/H = 23$. The second diffuser's mean velocity field displays two distinctively different recirculation regions, similarly to D1 the first recirculation zone originates from the asymmetric top corner at the outset of the expansion section propagating more gradually and diagonally across the full width of the diffuser's top wall before reattaching earlier than in D1 at $x/H = 20$. The second mean backflow volume is much smaller than the first one, it emanates from the bottom right expanding corner at $x/h = 6$ and reattaches at $x/H = 22$. High levels of streamwise turbulence (u_{rms}/U_b) is present in both diffusers at the interface between mean reverse flow and the streamwise core flow. This characteristic is further examined and detailed in the next section.

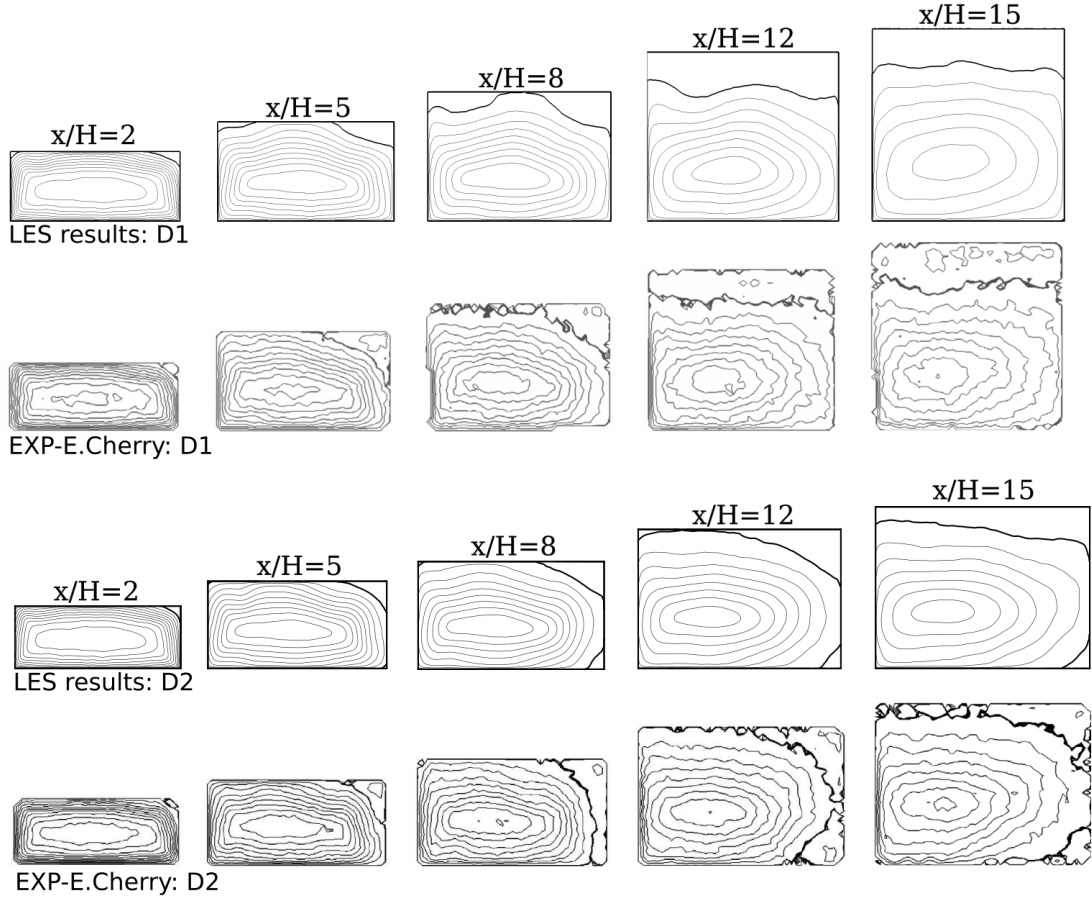


Figure 4.5: Normalised mean streamwise velocity contour (\bar{u}/U_b) of D1 and D2 at multiple cross-sections ($x/H=5,8,12,15$). Contour lines spaced 0.1m/s apart, bold line represents $\bar{u}/U_b = 0$.

Fig.4.5 presents LES-computed and measured contours of the normalised streamwise velocity in selected cross-sections for both diffusers. The figure shows that in the D1 diffuser, the flow separation emerges from the top right expanding corner and grows nearly equally on both sides of the diffuser ($x/H < 5$) before merging fully at the top wall ($x/H=12$) where the separated flow displays quasi-two-dimensional flow separation characteristics. The LES is in very good agreement with the measurements except that the second backflow area seems to appear earlier in the LES than in the experiment ($x/H=8$). Although this mechanism is less pronounced in the results of Schneider [2009] and Ohlsson *et al.* [2010], their

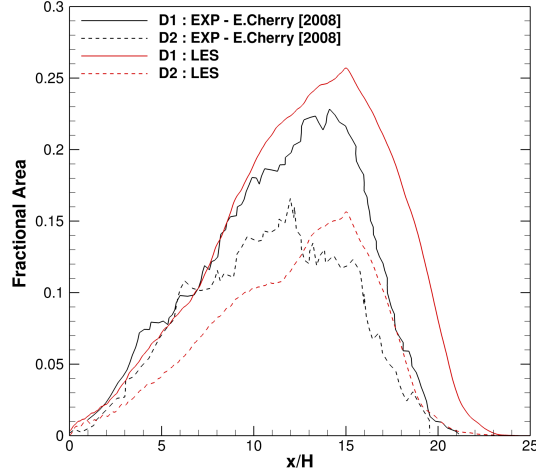


Figure 4.6: Fractional area occupied by the mean flow separation within the rectangular diffusers: D1 and D2

simulations also display a 'bubble' at $x/H=8$. For the diffuser D2, the mean flow separation behaviour is mostly in good agreement with the experiment, there is a slight difference in the formation of the bottom right corner bubble, which in the experiment seems to occur somewhere between $x/H=5$ and $x/H=8$. In the LES results two distinctive bubbles form at the top right corner and bottom right corner while in the experiment the top right corner bubble spreads fully onto the side wall ($x/H=8$) before splitting up further downstream ($x/H=10$).

The calculation of the fractional area occupied by the mean reversal flow quantifies the blockage effect enforced onto the flow field of the diffuser. The gradient of the fractional area near the entrance of D1 is in excellent agreement with the experiment until approximately $x/H=10$ where the two recirculating regions converge and the LES overpredicts the magnitude of the backflow region by approximately 3%. Although the gradient of the reduction of the separated flow is very similar to the experiment, the reattachment point is slightly delayed until $x/H=23$ in the LES simulation compared to $x/H=21$ in the experiment. Contrarily, the second diffuser D2 somewhat under-predicts the gradient of the fractional area translating to a smaller flow separation growth which delays its peak to $x/H=16$ compared to the experimental peak located at $x/H=12$. The

reattachment point of the flow separation in both the experiment and simulation coincide at $x/H=21$. The hydrodynamics of three-dimensional flow separations are challenging to capture accurately both experimentally and computationally. [Abe & Ohtsuka \[2010\]](#) provides the experimental fractional area which accounts for instrumentation error margin, the spatial disparities of the LES results reside well within these error margins.

4.3.2 Turbulence statistics and kinetic energy

Fig.4.7(a) presents profiles of the normalised root mean square of the streamwise velocity fluctuation (u_{rms}/U_b) at five locations ($x/H=2,6,10,15.5,18.5$) of D1 and D2 along the centre vertical plane, i.e. $z/H=1/2$. The experimental data is only available for the streamwise intensity for D1. The LES results are overall in excellent agreement with the experimental data. The two diffusers share similar characteristics in the development of the streamwise turbulence intensity along the vertical slice of both diffusers. In the first section at $x/H=2$, the streamwise turbulence intensity presents a similar profile as the one found in the flow development duct, the high turbulence intensity zones are located both near the top wall and bottom wall of the diffusers while a low intensity zone is found at half the height of the section within the core flow. Subsequently, the high shear stress zone at the bottom of the diffusers is slightly reduced along the expansion; further the high shear stress peak located at the top of the diffusers is gradually shifted toward the middle of the sections' heights from $x/H=5$ to $x/H=18.5$. This is due to the development of the mean flow separation, for which the developing shear layer due to the contact of the no-slip wall and streamwise velocity is now transferred to the interface between the recirculation zone and the streamwise flow. The high streamwise intensity zone is of slightly smaller magnitude in D2 when compared to D1, it reflects the smaller portion of the top wall occupied by the mean flow separation in D2.

Profiles of the $\langle u'v' \rangle / U_b$ shear stress in the centre line of the same five cross-section of diffusers D1 and D2 are plotted in Fig.4.7(b). The LES profiles of D1 are

RECTANGULAR DIFFUSER: INFLUENCE OF THE GEOMETRICAL ASPECT RATIO
ON FLOW SEPARATION BEHAVIOUR

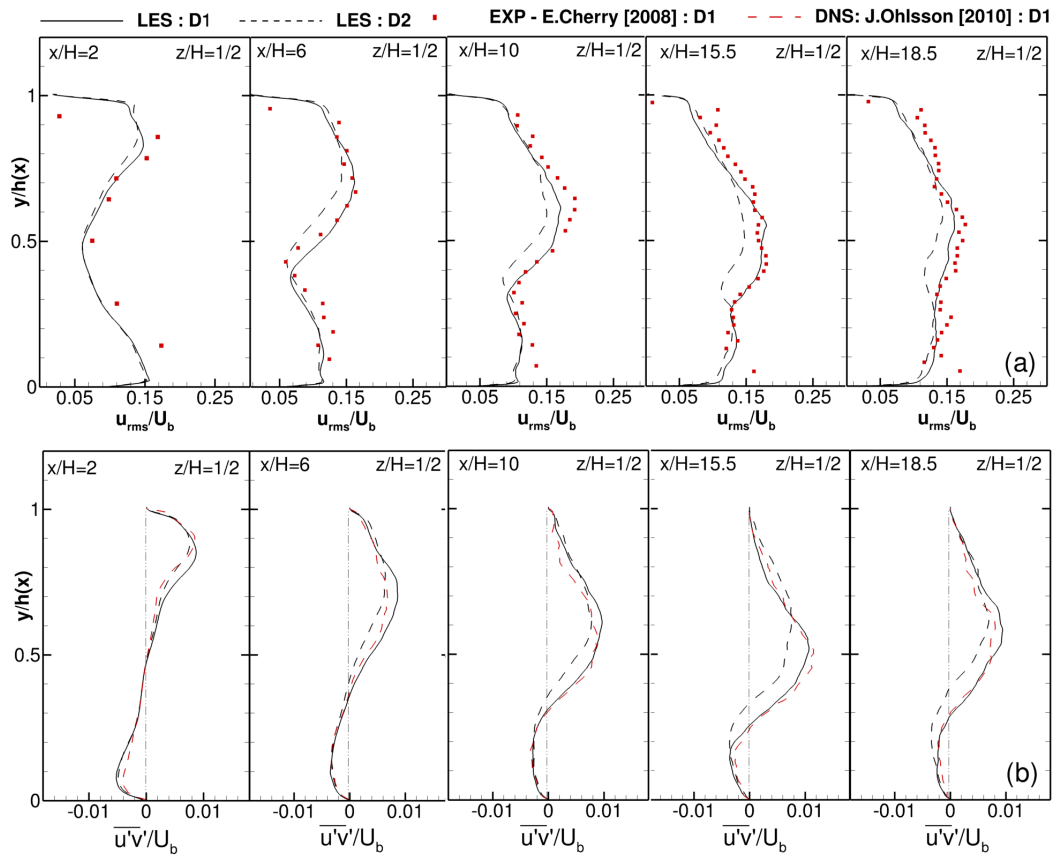


Figure 4.7: Vertical profiles located on the vertical plane $z/H=1/2$: (a) Normalised root mean square of the streamwise turbulent fluctuations u_{rms}/U_b , (b) Normalised shear stress $\overline{u'v'}/U_b$

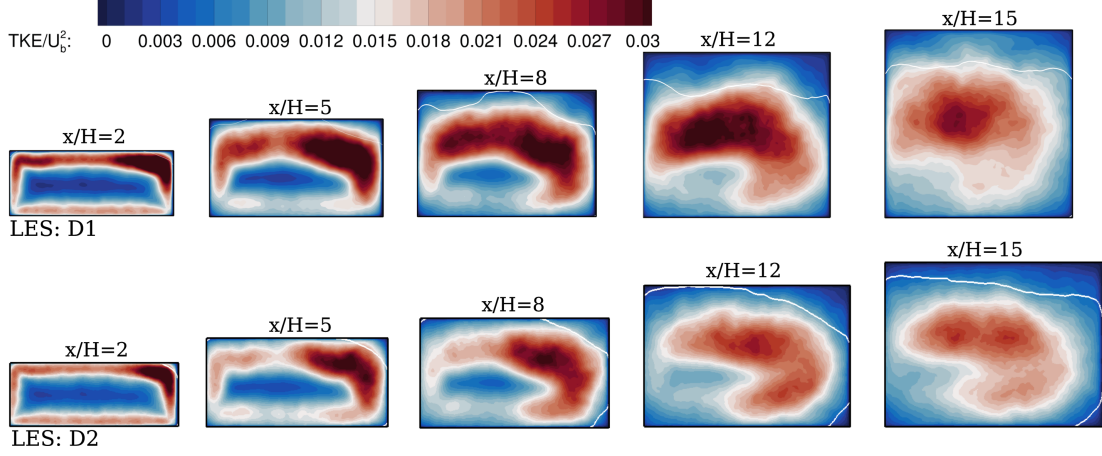


Figure 4.8: Contours of the turbulent kinetic energy at multiple cross-sections ($x/H=5,8,12,15$) along the D1 and D2, the white line represents the mean zero-streamwise velocity $\bar{u} = 0$

in excellent agreement with the DNS data of [Ohlsson *et al.* \[2010\]](#). As expected, the shear stress profile is symmetric at the beginning of the diffuser exhibiting equivalent shear stress magnitude on both top and bottom walls. Similarly to the streamwise turbulence the shear stress peaks increase in the downstream direction and gradually shift away from the top wall while the peaks remain constant near the bottom wall while only slightly shifting away. The profiles of the shear stresses are nearly identical in both diffusers, the smaller volume of the backflow near the top wall in D2 results in a slight vertical shift of the shear stress peak.

Fig.4.8 presents contours of the normalised turbulent kinetic energy (TKE) in cross-sections at the same x/H locations as above profiles. At the beginning of the expansion, $x/H=2$, both diffusers exhibit a high kinetic energy zone in the top right corner and D1 also has a high TKE zone located at the top left corner heralding the development of separated flow at these locations. Major differences in the distribution of TKE between D1 and D2 are appreciated at $x/H=8$, where the TKE zone in D1 is larger and the magnitude of the TKE is greater than in D2. At $x/H=12$ the high TKE zone of D1 has shifted left of the centre and the peak TKE of D2 has already reduced somewhat. In both diffusers, the magnitude of the highest zone in each section decreases downstream, the highest TKE/U_b^2

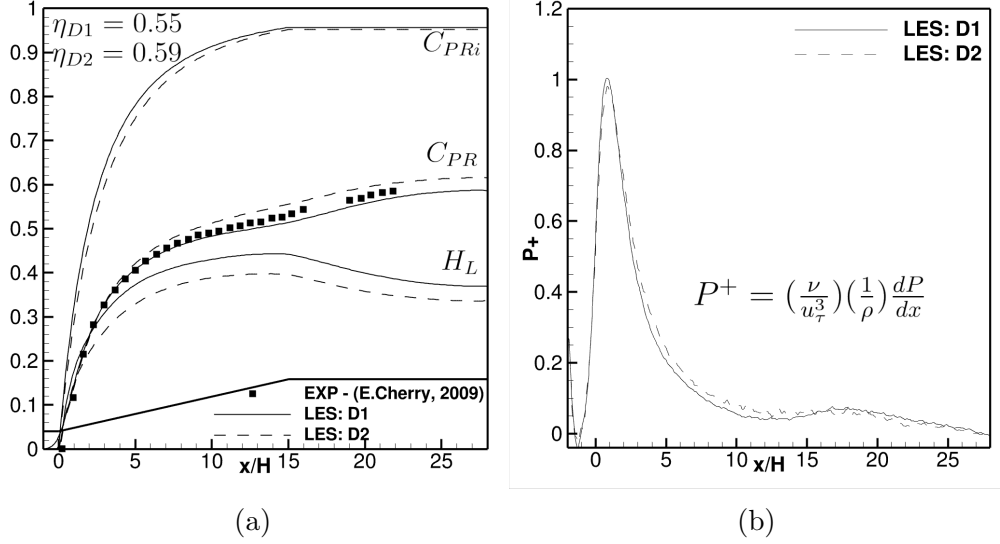


Figure 4.9: (a) One-dimensional pressure coefficient C_p , (b) Dimensionless pressure gradient P^+ along the two rectangular diffusers

magnitude zones are located in the first section of D1 (0.047) and D2 (0.04) while the peak magnitude in the last cross-section has reduced by 40% in D1 or by 30% in D2.

4.3.3 Pressure and efficiency

The pressure coefficient, C_P , is a long established and key measurement in diffuser design to evaluate their performance and efficiency. C_P represents the change of the static pressure normalised with the dynamic head at the diffuser inlet. Two distinctive methods exist: the first and most widely used is the one-dimensional pressure coefficient, it assesses the local pressure along the centerline near the wall of the diffuser while the second method, deemed more accurate and is used in this study, calculates the pressure coefficient using the pressure area average of each cross-section within the diffuser (Eq.4.1). The efficiency and non-dimensional head losses is conveniently derived from the pressure coefficient. The efficiency ($\eta = C_{PR}/C_{PRi}$) corresponds to the ratio between the measured pressure coefficient and the ideal pressure coefficient of uniform inviscid and frictionless flow ($C_{PRi} = 1 - 1/(AR)^2$) while the non-dimensional head loss is the difference be-

tween the two aforementioned terms ($H_L = C_{PRi} - C_{PR}$).

$$C_{PRS} = \frac{(1/A_s) \int P_s dA_s - (1/A_{ref}) \int P_{ref} dA_{ref}}{0.5\rho(1/A_{ref}) \int U_1^2 dA_{ref}} \quad (4.1)$$

Fig.4.9a presents the average pressure coefficient of each section along the diffuser. The LES slightly underpredicts the pressure recovery in the D1 diffuser after $x/H=10$ but is overall in very good agreement with the experimental data of [Cherry *et al.* \[2009\]](#). This slight difference is directly correlated with the size of the mean flow recirculation area. In both diffusers, a strong adverse pressure gradient develops between $x/H \in [0, 2]$ near the throat of the diffuser before considerably reducing after $x/H > 2$ once the mean flow separation starts to spread across the diffusers (Fig.4.9b). Subsequently, the adverse pressure gradient follows similar trends to the growth gradient of the backflow fractional area in Fig.4.6. The non-dimensional headloss (H_L) reveals an inflection point at the interface between the end of the expansion part and the tail section of the diffuser ($x/H=15$) from which the losses decrease inversely proportional to the pressure coefficient due to the reduction and dissipation in fractional area of the recirculating flow. Similar findings are observed in planar diffuser of [Törnblom *et al.* \[2009\]](#). The efficiency of D2 is slightly higher than D1 with values of 59% or 55%, respectively.

4.3.4 Instantaneous flow

Prior to the quantification of the temporal unsteadiness of the backflow region the unsteadiness of the backflow inside each the two diffusers is visualised. Fig.4.10 and Fig.4.11 provide contours of the instantaneous streamwise velocity at three different instants in time in the X-Y plane along $z/H=7/8$ and the X-Z plane at $y/H=1/8$. The instantaneous flow in both diffusers does not exhibit a single large recirculation zone as suggested in Fig.4.4, but instead the meandering of the flow entering the diffuser leads to multitude of high shear stress zones close to the wall that in turn forces the streamwise flow to separate from its turbulent boundary layer and to reverse. The snapshots highlight specific locations of the

RECTANGULAR DIFFUSER: INFLUENCE OF THE GEOMETRICAL ASPECT RATIO
ON FLOW SEPARATION BEHAVIOUR

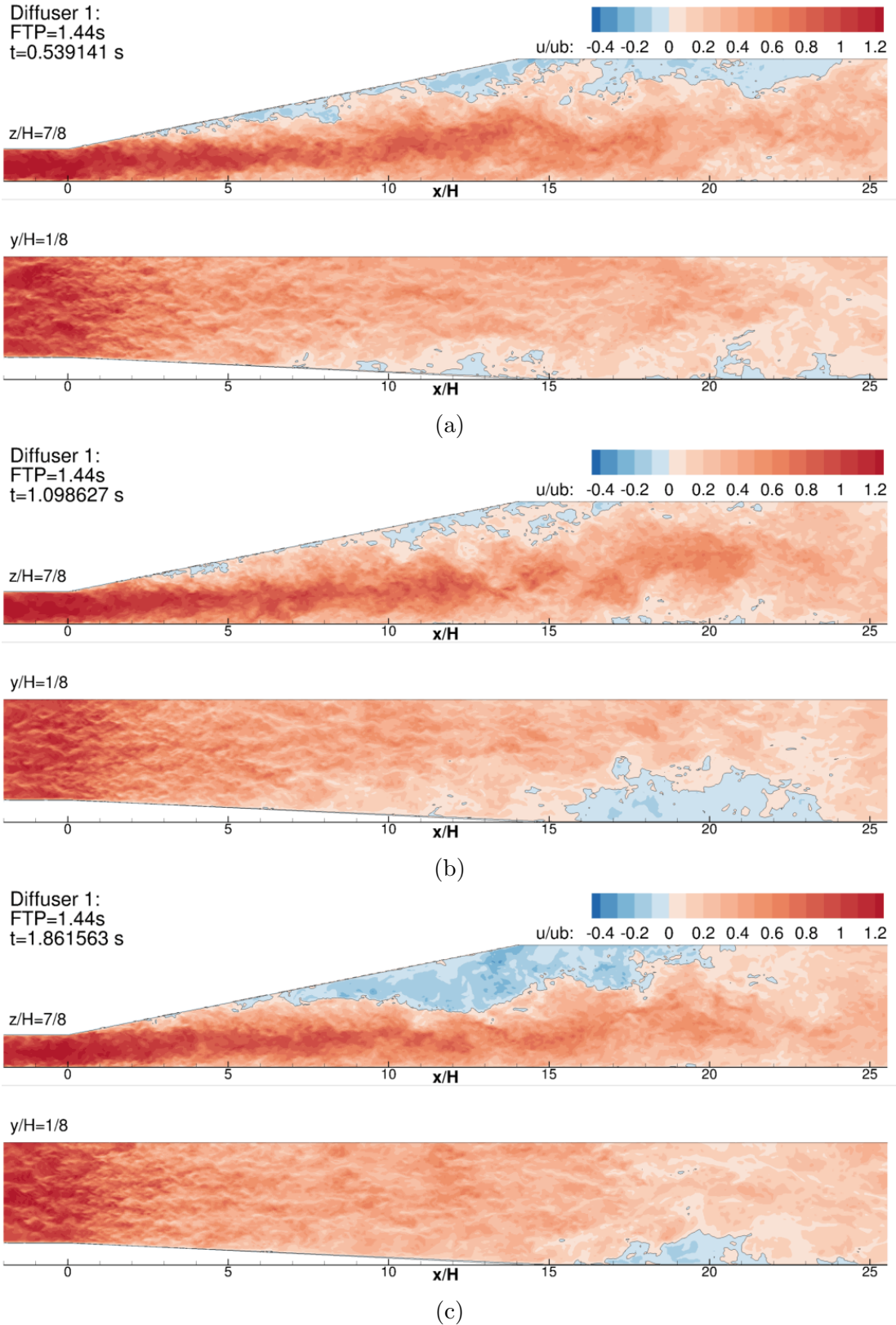


Figure 4.10: D1: Side and top views of normalised instantaneous streamwise velocity u/U_b at three selected instants in time: $t=0.54, 1.1, 1.86$

RECTANGULAR DIFFUSER: INFLUENCE OF THE GEOMETRICAL ASPECT RATIO
ON FLOW SEPARATION BEHAVIOUR

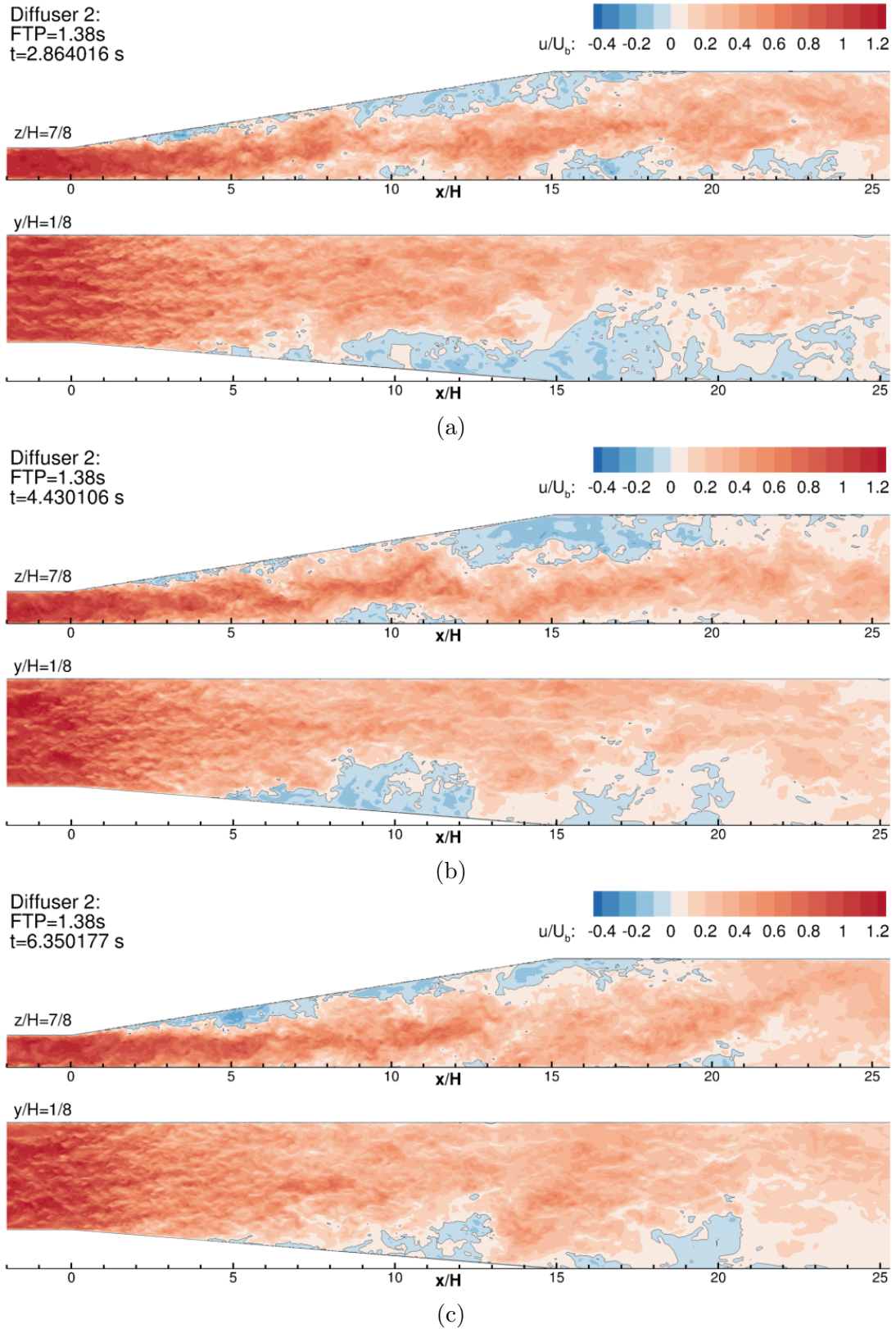


Figure 4.11: D2: Side and top views of normalised instantaneous streamwise velocity u/U_b at three selected instants in time: $t=2.86, 4.43, 6.35$

separated flow and the behaviour is perceived from visualisation and animation of more than 1000 snapshots representing 10 FTPs through both diffusers. These reveal a core meandering generated through the constant action-reaction feedback between the streamwise high velocity core and the different reverse flow pockets. In Fig.4.11b, the recirculation zone located at $x/H=10$ is easily distinguished from the core velocity near the top inclined wall. Although, the meandering phenomenon is present in both diffusers, it is evident from the respective snapshots that the aspect ratio results in the flow separating at different locations.

The large angle expansion in D1 drives the instantaneous flow to separate away from the boundary layer of the top inclined wall. The backflow pockets contain high reverse momentum attempting to travel upstream toward the throat of the diffuser (Fig.4.10a). These pockets often stagnate around $x/H=5$ and $x/H=15$ and are only occasionally washed away before dissipating on their way towards the end of the diffuser whilst forming large reverse flow zones as seen in Fig.4.10b. Near diffuser D1's wall, reverse flow significantly detaches at $x/H=10$ and is subsequently transported toward the end of the diffuser to form a large instantaneous backflow region with low kinetic energy. The separated flow located at the top wall of diffuser D1 dictates the meandering of the core.

The behaviour of flow separation and interaction with the core flow is slightly different in the second diffuser, D2, its lower asymmetric expansion ratio $AER_{D2} = 2$ results in the development of significant reverse flow on both expanding walls (Fig.4.10a). Similarly to diffuser D1, the reverse flow pockets travel towards the throat of the diffuser (Fig.4.11c), but remarkably in D2, stationary pockets form both on the top and side expansion walls around $x/H=10$ (Fig.4.11b).

4.3.5 Unsteadiness of the flow separation

The backflow coefficient (γ) is an excellent indicator for quantifying the flow separation unsteadiness, Simpson [1996] first introduced the method which consist of computing the period during which the flow moves in the streamwise direction. A backflow coefficient of $\gamma = 1$ corresponds to a region where no instantaneous

RECTANGULAR DIFFUSER: INFLUENCE OF THE GEOMETRICAL ASPECT RATIO
ON FLOW SEPARATION BEHAVIOUR

FV1=Backflow FV in the expansion , FV2=Backflow FV in the extension , FVT=Backflow FV in the total diffuser

FS Type	D1 : FV1 (%)	D1 : FV2 (%)	D1 : FVT (%)
ID ($\gamma = 0.99$)	48.03	50.69	49.58
TD ($\gamma = 0.5$)	16.33	8.12	11.55
PTD ($\gamma = 0.2$)	6.98	3.18	4.75
FS Type	D2 : FV1 (%)	D2 : FV2 (%)	D2 : FVT (%)
ID ($\gamma = 0.99$)	42.15	37.79	39.59
TD ($\gamma = 0.5$)	9.20	3.27	5.71
PTD ($\gamma = 0.2$)	2.00	0.21	0.97

ID=Incipient Detachment , TD=Transitory Detachment , PTD=Persistent Transitory Detachment

Table 4.2: Fractional Volume (FV) occupied by the backflow coefficient: $\gamma = 0.99, 0.5, 0.2$ within the rectangular diffusers D1 and D2

flow reversal is recorded during the simulation, inversely if $\gamma = 0$ the region only comprises reverse flow. [Simpson \[1996\]](#) classifies the unsteadiness of a region in three categories, $\gamma = 0.99$ corresponds to an Incipient Detachment (ID), $\gamma = 0.8$ satisfies an Intermittent Transitory Detachment (ITD) and $\gamma = 0.5$ represents a Transitory Detachment (TD) equivalent to mean flow separation results in Fig.4.4. The current classification does not include the location of reversal of high momentum pockets within the diffuser. In an effort to complement and harmonise the current classification one could consider $\gamma = 0.2$ as Persistent Transitory Detachment (PTD) and $\gamma = 0.01$ as Permanent Detachment (PD).

Table 4.2 complements Fig.4.13 and Fig.4.12 to enable the quantification and location of these quasi-permanent stagnation zones and other classified unsteadiness regions. The 2D contours of the backflow coefficient suggest that the ID region is similar in both diffusers but Table 4.2 reveals that the fractional volume of this region is 10% greater in D1(49.6%) than in D2(39.6%). This ID region describes the delimitation volume in with all the reversal separated flow emerges, develops and dissipates. The mean flow separation (TD) is inevitably larger in D1(11.55%)

RECTANGULAR DIFFUSER: INFLUENCE OF THE GEOMETRICAL ASPECT RATIO
ON FLOW SEPARATION BEHAVIOUR

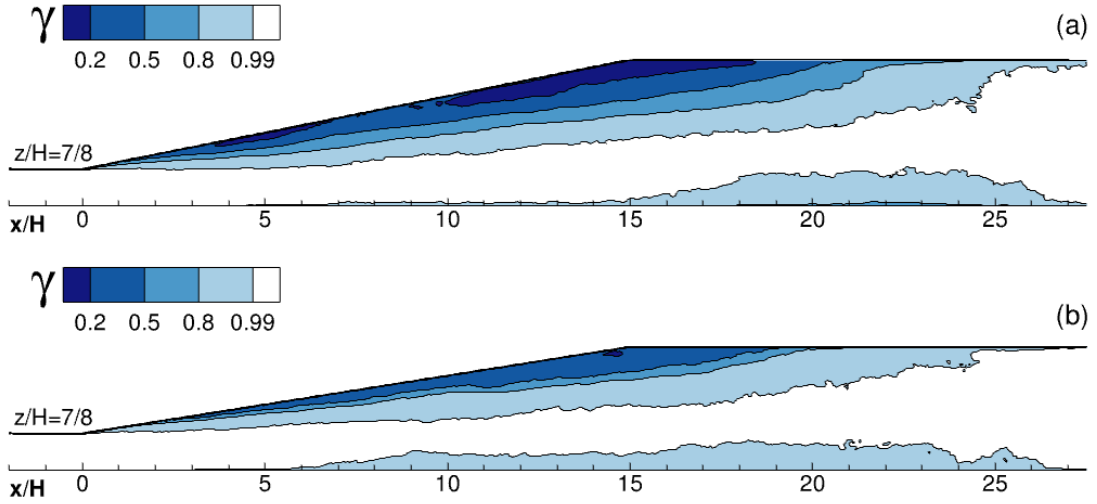


Figure 4.12: Backflow coefficient contours of the vertical plane $z/H=7/8$: (a) D1, (b) D2

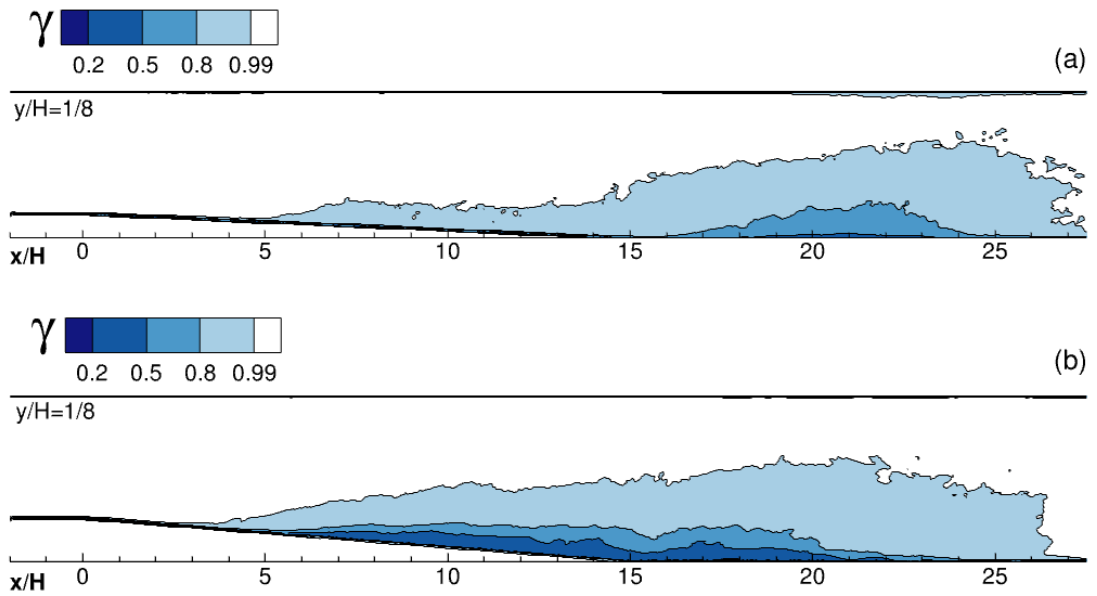


Figure 4.13: Backflow coefficient contours of the horizontal plane $y/H=1/8$: (a) D1, (b) D2

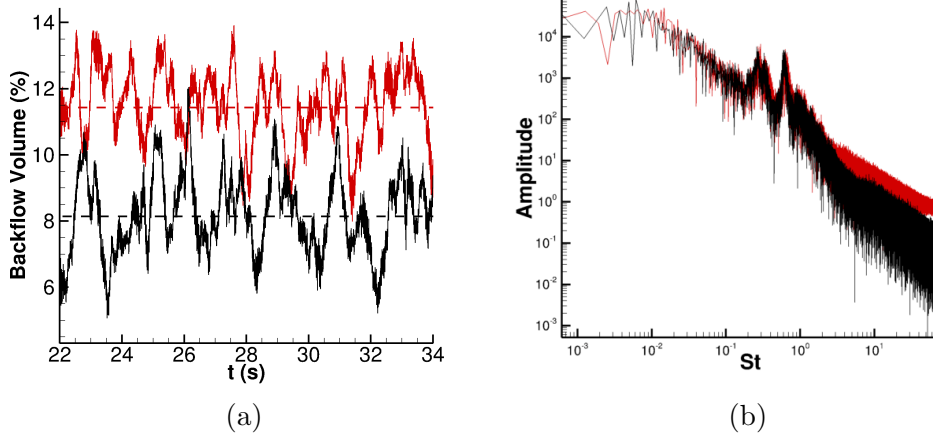


Figure 4.14: (a) Flow separation total volume time series across expansion and extension sections of the two rectangular diffusers and (b) PSD of the flow separation total volume series

than in D2(5.71%) and the respective location of these zones are in line with previous observations (from Fig.4.4), the D1 TD zone is much larger than in D2 in Fig.4.12, inversely D2 TD zone expands between $x/H \in [5, 23]$ while the D1 TD is considerably smaller between $x/H \in [18, 22]$ in Fig.4.13. The PTD region is depicted at two different locations in D1 vertical plane between $x/H \in [3.5, 7]$ and $x/H \in [10, 17.5]$ while only a small-scale zone around $x/H=15$ is present in D2, no PTD regions are observed in the horizontal plane (Fig.4.13). The fractional volume occupied by the PTD region within D1(4.95%) is nearly 5 times larger than in D2(0.97%) further explaining the greater drop in efficiency of D1 as these regions act as long lasting localised blockage effect within diffusers. In [Cherry *et al.* \[2008\]](#) the fractional volume of the mean flow separation within the expansion part of the diffuser (FV1) is examined and the LES data of D1(16.33%) and D2(9.20%) are in relatively good agreement with the experimental data of both diffuser respective 14.1% and 10.7%. It is interesting to note the importance of the tail section (FV2) specifically in diffuser design as both flow separation zones recover in this section. The volume occupied by the mean flow separation in the tail section is halved in D1 in comparison with D2 and nearly three times smaller in D2 which exhibits a much faster recovery.

Fig.4.14a presents the temporal evolution of the cumulative instantaneous separated flow normalised by the cumulative volume of both expansion and extension sections of the two diffusers. It calculates the ratio between cells having flow reversal (negative streamwise velocity) and the total number of cells constituting the expansion and extension sections, i.e. the volume in percentage of the back-flow region will be of smaller magnitude than previously. The mean cumulative backflow volume are 11.4% and 8.1% of the D1 and D2 volumes, respectively. The diffusers' time series both exhibit a clear phase of growth followed by a reduction phase of the total instantaneous separated flow. The Fast Fourier Transformation of the time series fluctuations (Fig.4.14b) clearly captures these distinctive phases in both diffusers. The growth phase has a non-dimensional periodicity (Strouhal number) of $St = 0.7$ while the reduction phase periodicity is $St = 0.1$. It is interesting to note that at no point in time the reverse flow fully disappears. For diffuser D1, the cumulative backflow volume ranges from 7% to 13.94% while for D2 it fluctuates between 5.1% and 12%. The root mean square values which evaluate the level of fluctuation around the mean value of the time series suggests that the flow separation is more unsteady in D2 than in D1 having values of $BV_{rms} = 14.3\%$ (D2) and $BV_{rms} = 9.8\%$ (D1). It suggests that a high level of unsteadiness is beneficial toward improving the efficiency of diffusers as it prevents the development of Persistent Transitory Detachment.

4.3.6 Turbulent boundary layer and coherent flow structures

The instantaneous flow separation emerges from high instantaneous shear regions near the walls of the diffusers, which are manifested through the formation of energy-containing motions, also called coherent structures. The topology and classification of these coherent structures remain challenging for experimentalists due to their unsteadiness, scale and versatility. The method of quadrant analysis was first developed by Wallace *et al.* [1972] to reveal the presence of energy-containing motions in a boundary layer and was soon adopted to investigate near-wall turbulence of open-channel flow (Kim *et al.* [1987] and Zhou *et al.*

[1999]). The quadrant analysis relies on a time series of the velocity fluctuations comprising the anisotropic Reynolds Stresses at specified probe locations. Quadrant one ($u' > 0, w' > 0$) reveals a forward and upward motion (also referred to as outward interaction). The second quadrant ($u' < 0, w' > 0$) describes a backward and upward motion, referred to as ejection, while the third quadrant ($u' < 0, w' < 0$) causes a backward and downward momentum, or inward interaction. The fourth quadrant ($u' > 0, w' < 0$) describes a forward and downward motion, known as a sweep. In the two diffusers, all directions are bounded by smooth walls depending on the probe location the motion is analysed relative to its closest wall to understand if the fluid is breaking away from the wall toward the core of the flow or if it is conveying towards the wall.

In order to identify, visualise and examine coherent structures in the diffuser flow, velocity probes are placed in the core of the high momentum zone, in the vicinity of the top and bottom wall and near the boundary of the time-averaged flow separation zone. The probes' locations are denoted from P1 to P9 in Fig.4.17. Quadrant analysis is carried out using a matrix of 100×100 using 300,000 data pairs for each of the nine points within the two diffusers (Wallace & Brodkey [1977]). It is equivalent to a computational time of D1=14 FTPs and D2=15 FTPs. The most centre and smallest contour corresponds to the maximum occurrence event (=1); subsequently, each line contour is spaced with 0.1 increments. For instance, the turbulent events located in between the third and second line contour have an occurrence of 80% compared to the first contour. It enables better visualisation of the distribution and density of the events.

Fig.4.15 and Fig.4.16 plot the normalised streamwise (u'/u_{rms}) and vertical (v'/v_{rms}) fluctuations at these 9 locations which are spread over the $z/H=1/2$ plane. The nature of the turbulent motion is evaluated at 3 different sections, near the entrance of the diffuser $x/H=2$ (P1, P2, P3), in the middle of the expansion section at $x/H=10$ (P4, P5, P6) and within the tail section at $x/H=20$ (P7,P8,P9). Three probes are respectively placed near the bottom wall, near the top wall and in the middle of the section. In all three sections, the probes located near the top wall and the bottom present similar quadrant characteristics in both dif-

RECTANGULAR DIFFUSER: INFLUENCE OF THE GEOMETRICAL ASPECT RATIO
ON FLOW SEPARATION BEHAVIOUR

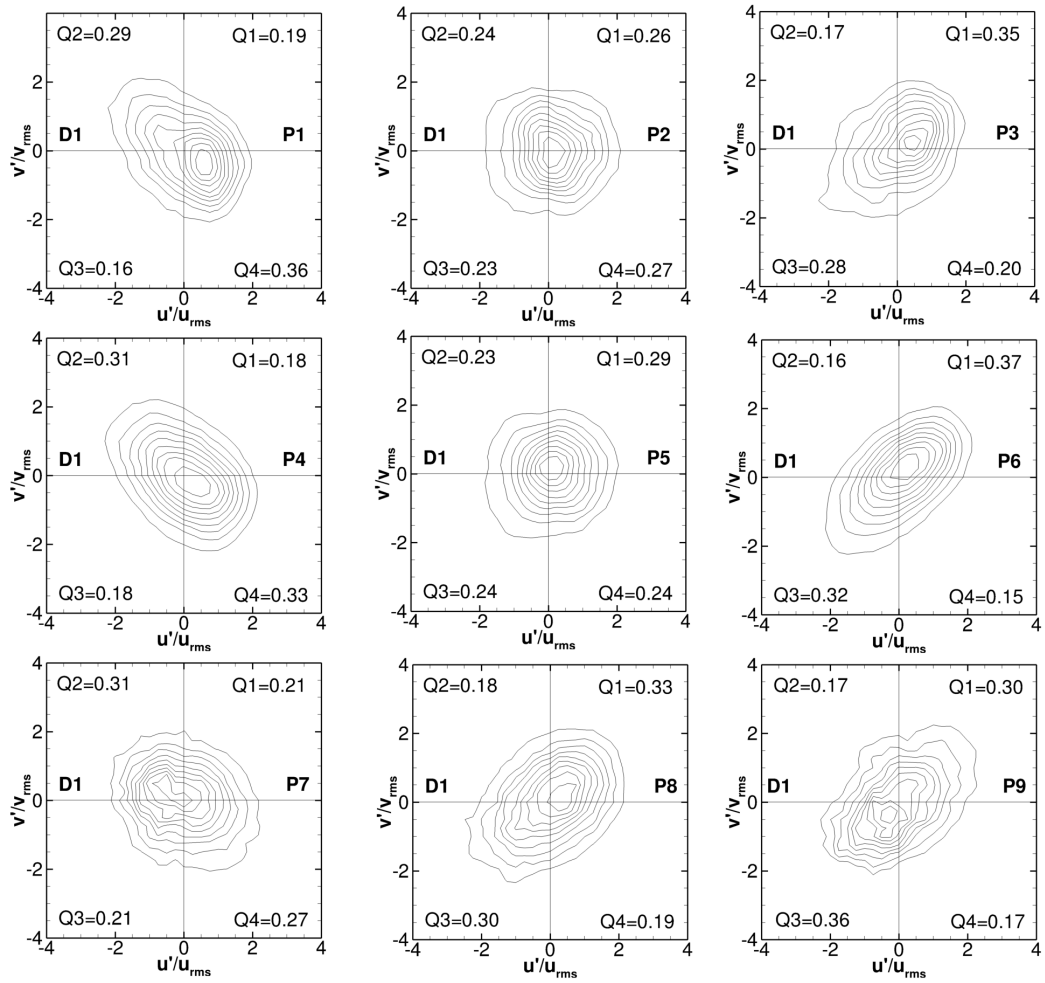


Figure 4.15: Quadrant Analysis of the shear stress $u'v'$ at specific locations across D1

RECTANGULAR DIFFUSER: INFLUENCE OF THE GEOMETRICAL ASPECT RATIO
ON FLOW SEPARATION BEHAVIOUR

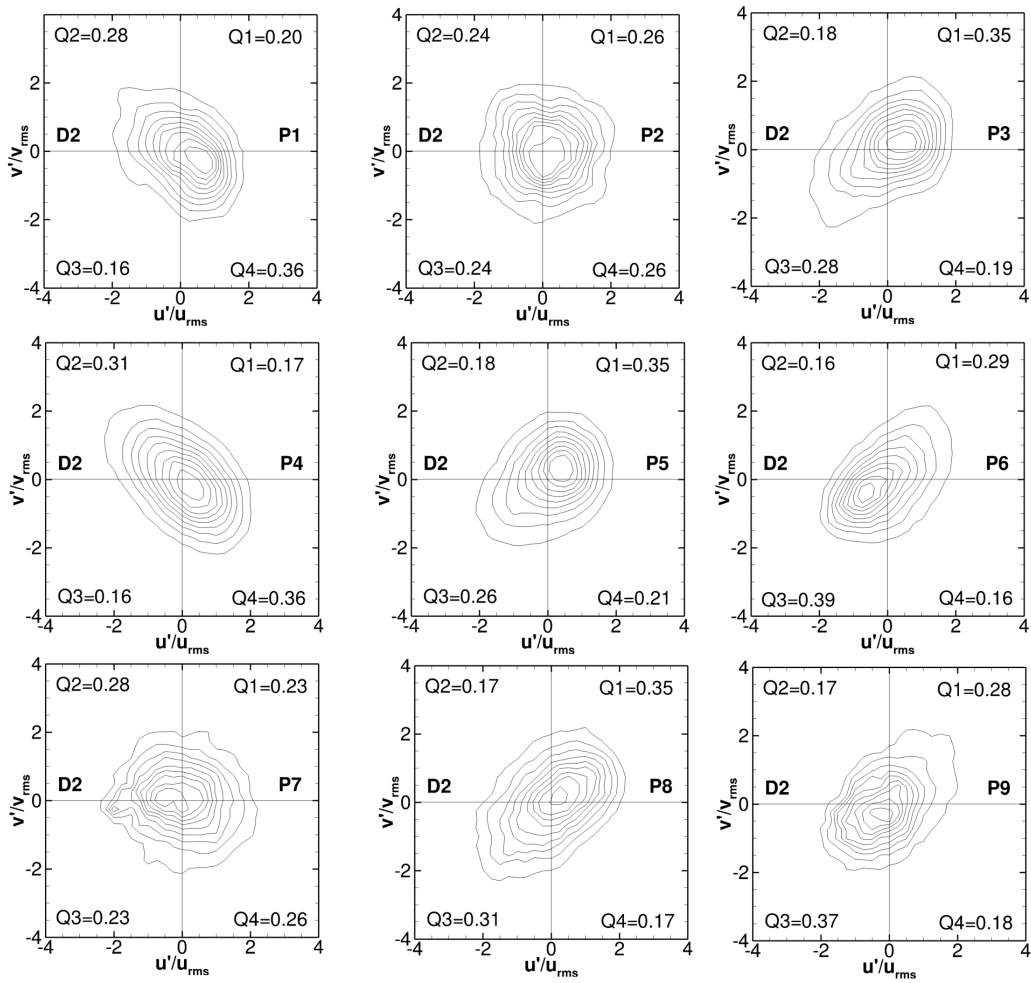


Figure 4.16: Quadrant Analysis of the shear stress $u'v'$ at specific locations across D2

fusers. The motion near the bottom wall P1, P4, P7 possess similar temporal coherence and share dominating Q2 (sweep) and Q4 (ejection) events, suggesting the occurrence of hairpin vortices from the flat bottom wall of the diffusers (Adrian [2007]). Near the top inclined wall, the primary motions are forward and upward (Q1) and backward and downward (Q3). These motions are not characteristic of the development of hairpin vortices (Zhou *et al.* [1999]) when the referenced wall is located below the probe. However, in this specific case, the inclined wall is located above the probe inverting the quadrant mechanism, the Q1 corresponds to a forward upward motion toward the wall (sweep) while Q3 is backward downward motion away from the wall. These motions at P3, P6 and P9, are attributed to the presence of coherent structures near the top inclined wall. In both diffusers, evidently, the distribution at P2 located in the core flow is more isotropic and the Reynolds shear stresses are homogeneous. It is the region of lowest shear hence without the development and conveying of significant turbulence structures. Further, after reaching the end of the expansion section the meandering core flow has dissipated. At P7,P8 and P9, the quadrant analysis captures the energy-containing motion that are convected from the top and bottom wall of the expansion part of the diffuser (see Fig.4.17). The sweep motion towards the wall is the dominant turbulence event of the probes located near the top (P1,P4) or bottom wall (P3,P6) of the diffusers' expansion section.

The quadrant analysis does provide not only information regarding the formation of energy-containing motion but also reflects on the state of the flow. In the middle probe of the second section, P5 is more isotropic in D1 than in D2 but both respectively have sweep dominant quadrants Q1=29 and Q1=35. The location and dominance of sweeps at this location suggests that sweeps towards the top inclined wall that acts as an opposing force to the reversal flow interface attempting a reattachment. The two diffusers display some discrepancies nonetheless, at P6 the sweep motions are dominant in D1 (Q1=37) while ejection events are prominent in D2 (Q3=39). In the tail section, the third quadrant Q3 is clearly dominant in P9 (Q3: D1=0.36, D2=0.37) heralding the presence of recirculating flow at these locations. Near the bottom wall at P7, the turbulence events are relatively isotropic in D2 while strong ejection events remain in D1 (Q3=31)

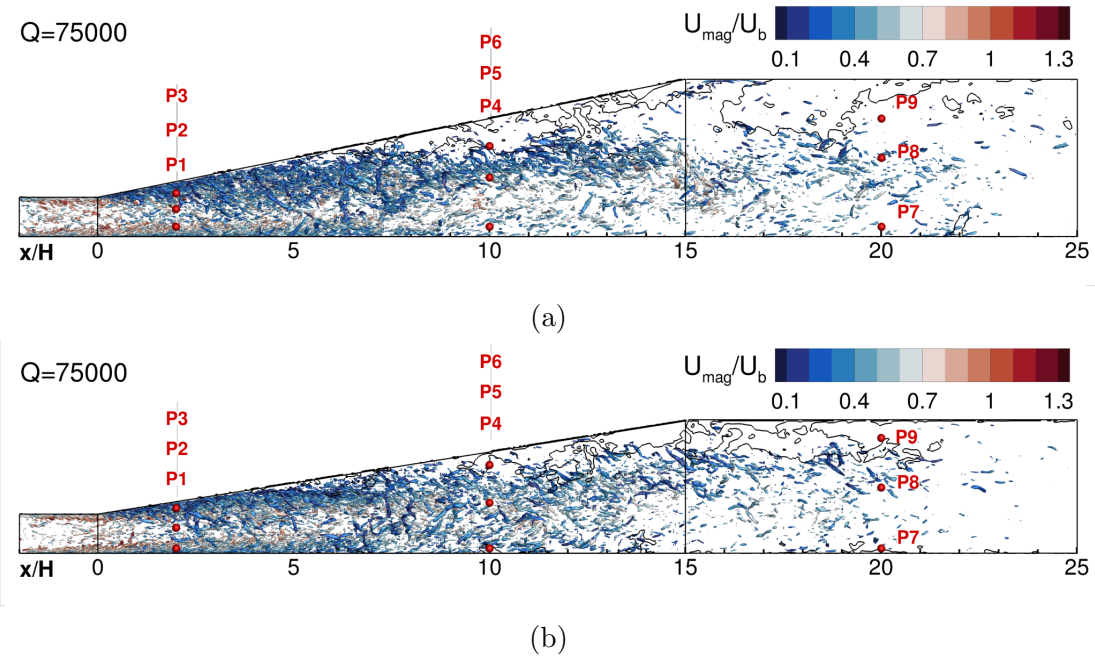


Figure 4.17: Iso-surface Q Criterion (75000) contoured with the normalised Velocity magnitude (U_{mag}/U_b) : (a) D1 , (b) D2

which may be due to the development of ITD during the monitoring of that probe.

Experimental investigations mostly rely on quadrant analysis, or 2D-planes, to depict the characteristic motions of coherent structure in the vicinity of the turbulent boundary layer. Numerical investigations possess a significant visualisation advantage enabling the classification and revelation of the topology of the coherent structures. The Q criterion is the difference between the symmetric (Strain rate= $S_{ik}S_{kj}$) and the anti-symmetric (Rotation rate= $\Omega_{ik}\Omega_{kj}$) part of the velocity gradient tensor of $u_{i,j}$. If Q is positive, the coherent structures are dominated by rotation, when Q is negative, the energy-containing motion is inversely driven by strain. The coherent structures illustrated in Fig.4.17 presenting isosurfaces of $Q=75,000$, are only composed of small scale turbulent eddies and large structures are absent from the flow field. One can depict two distinctive phenomena, the eddies bursting from the top turbulent boundary layer ($x/H \in [0, 5]$) and their conveyance to the tail section through a passage bounded by the core flow and the separated flow, while the coherent structures emerging

from the bottom turbulent boundary layer are constrained by the wall and the core flow. The core flow dissipates around $x/H=15$, the energy-containing structures from the top wall and bottom wall mix together and are convected by the streamwise flow. An isometric view of the Q criterion three-dimensional visualisation reveals the emergence and conveying of quasi-streamwise vortices including low-speed streaks, high-speed streaks and short spanwise hairpin vortices when conveyed away from the wall. The presence of these quasi-streamwise hairpins is also supported by Fig.4.10 and Fig.4.11 $y/H=1/8$ contour. These contours exhibit high-momentum and low momentum streaks between $x/H \in [-2, 5]$ which is characteristic to these quasi-streamwise hairpins (Tomkins & Adrian [1999]). Malm *et al.* [2012] arrived at similar findings with a POD analysis, which did not depict any large horseshoes vortices. The observed coherent structures can be considered as vorticity transporting entities Adrian [2007], supposedly the meandering of the core flow does not provide enough stability in the high shear region to sustain the development of large horseshoes vortices.

4.4 Summary

Large-eddy simulations of flow in two asymmetric diffusers (D1 and D2) have been performed. The accuracy and quality of the LES results in terms of the time-averaged flow and its fluctuation characteristics have been assessed using experimental data of Cherry *et al.* [2008]. After successful validation of the simulations, the efficiency and pressure recovery of the two diffusers were evaluated. The mean recirculation zones in the diffuser are bounded by high shear stress and subsequently regions of elevated turbulent kinetic energy (TKE). The second diffuser with an area aspect ratio of 2.01 shows better performance in terms of pressure loss and efficiency than the first diffuser with an area aspect ratio of 4.46. The hydrodynamic behaviour of the instantaneous flow separation in both diffusers has been described through visualisation of the instantaneous flow in vertical and horizontal planes at selected instants in time, exhibit the quasi-periodic behaviour of the flow separation consisting of numerous smaller pockets of reverse flow near the top and side expanding walls which travel upstream toward

the throat of the diffuser. Depending on the size and the velocity magnitude of the reverse flow, these pockets either dissipate or merge with other reverse flow pockets to form larger recirculation bubbles. Whilst in D2 these large recirculation pockets are washed away quite rapidly by the meandering core flow, in D1, some of these large backflow regions stagnate for more than 80% of the computational time and are hence being considered Persistent Transitory Detachment (PTD). The PTD pockets reduce the unsteadiness of the flow significantly create long-lasting local flow blockage thereby reducing greatly the deceleration rate of the incoming flow, which translates into higher pressure losses and less efficient pressure recovery. The Power Spectral Density (PSD) of the fractional volume of the instantaneous reversal flow time series revealed a growth and reduction phase of the instantaneous flow separation. The two diffusers exhibit similar growth ($St=0.7$) and reduction ($St=0.1$) phases suggesting a gradual accumulation of reversal flow during the growth followed by a rapid detachment and downwash of the large recirculation zones. The root mean square of this time series evaluates the unsteadiness of the flow separation, it detected the influence of the PTD as D1 $BV_{rms} = 9.8\%$ and D2 $BV_{rms} = 14.3\%$ translating into a greater unsteadiness of the flow separation. It suggests that high unsteadiness in the flow separation leads to improvement in efficiency and performance of the diffuser. Lastly, quadrant analyses at various locations inside D1 and D2 have revealed the characteristics of the shear stress propitious to the emergence of coherent structures. The Q criterion iso-surface of the flow depicts the occurrence of low-speed streak, high-speed streak and small spanwise roller within the flow field of both diffusers.

Chapter 5

Conical Diffuser: Impact of a swirling inlet onto the flow-separation behaviour

5.1 Overview

Axisymmetric conical diffusers were extensively investigated during the 20th century, leading to the production of performance graph which correlates geometrical and inlet condition parameters with the diffuser's efficiency. Moreover, ensuing from these studies design guidelines were elaborated to produce the most efficient diffuser, for conical diffuser the most optimal opening angle proved to be $2\theta \in [6^\circ, 8^\circ]$ with a normalised length of $L/R \in [25, 30]$ (Kline [1959]) and a short tail section preceding the diffuser (Patterson [1938]). These experiments were solely based on the pressure coefficient monitored along the diffusers using Pitot tubes. The first extensive research on the flow field of a conical diffuser was performed by Azad [1996] research group. Over 28 years the group produced more than 10 papers, including Azad & Hummel [1971] who first quantified and profiled the location of the intermittent flow separation, the flow was classified as four distinct regions, the core region where no reversal flow (ID), the core intermittent

region, the constant shear layer and the wall intermittent region (ITD). These findings were furthered in Singh & Azad [1995c] reveal that the magnitude of the instantaneous reversal flow appears to be reduced at high to Reynolds number, the triple correlation (Singh & Azad [1995b]) captures the high turbulence intensity around this reversal flow. The time-averaged characteristic in conjunction to with the turbulent kinetic energy budget revealed that for a 8° angle opening diffuser at the edge of the boundary layer the production of energy is roughly 100 times greater than the viscous dissipation (Okwuobi & Azad [1973]). Azad & Burhanuddin [1983] studied the near-wall velocities in the vicinity of the buffer layer and discovered that the skewness decrease towards the wall while the kurtosis of the power density function increases. Arora & Azad [1980] evaluated and revealed that the production is much greater than the dissipation near the throat of the diffuser using the turbulent kinetic budget. Ensuing from Azad [1996]’s experimental results, Lee *et al.* [2012]’s DNS numerical study to investigate the effect of the opening angle on the mean and instantaneous flow field, visualisation and Linear Stochastic Estimation of the coherent structure near the wall of the diffuser evidence the increase of the streaky shortened structure in the outer region of the diffuser.

The inlet flow condition is a key parameter in diffuser design. Extensive research was produced on the distortion, the boundary layer and the blockage effect of the flow entering the diffuser. Laboratory experiments revealed the potential of swirling inlet in preventing the development of large flow detachments, which ultimately benefit the performance of the diffuser. So [1967] studied the effect of the swirling number on the diffuser flow field, for strong swirling intensity, a two-celled vortex, which is a stagnant spherical recirculation, was observed at the middle of the diffuser. McDonald *et al.* [1971] quantified the performance improvement of a wide range of diffuser under three different swirling inlet. When the area ratio of the diffuser was too low ($AR < 2$) or the expansion angle too high ($2\theta > 30^\circ$) the inlet tangential velocity had a negligible effect on the pressure recovery of the flow. Clausen *et al.* [1993] provided a detailed study of the Reynolds shear stress near the wall of a $2\theta = 20^\circ$ diffuser under a fully developed inlet and a swirling inlet $Sw = 0.59$. The findings suggest that the swirl stabilise

the curvature of the flow while its direct impact on the turbulent structure within the boundary layer is minimal compared to the pressure gradient. Senoo [1974] investigated the effect of trailing vortices onto the boundary layer, depending on the opening angle of the diffuser the vortices can lead to a reduction or an increase of static pressure fluctuation within the diffuser. Moreover, Yasutoshi Senoo *et al.* [1978] furthered their research and studied the performance of a diffuser under five different swirling regimes. The results correlate the pressure gradient, the magnitude of the core centerline and the axial deceleration with the strength of the swirling inlet. Mcdonald *et al.* [1971] and Yasutoshi Senoo *et al.* [1978] indicated that the opening angle (geometrical parameter) had substantially more influence on the diffuser performance than the swirling inlet parameter.

The benefit of prescribing a moderate swirling number at the inlet of a conical diffuser to improve its performance has already been established. Nonetheless, the influence of high tangential momentum on the hydrodynamics of the instantaneous flow and the development of the energy-containing motion is still unclear. This paper first validates the time-averaged flow field of Okwuobi & Azad [1973] 8° diffuser when subjected to a fully developed incoming flow. Moreover, a new methodology is developed to prescribe accurately a turbulent axisymmetric swirling inlet as a boundary condition. The solid-body swirling inlet and the evolution of its tangential velocity within a pipe are validated using Rocklage-Marliani *et al.* [2003] experiment based on a swirling number $Sw=0.6112$. The Okwuobi & Azad [1973] diffuser has one the most optimised opening angle, which prevents the emergence of large and long-lasting recirculation zones (Patterson [1938]). For this reason, the parametric study investigating the influence of the swirling inlet on the flow separation is undertaken within a conical diffuser with an opening angle of $2\theta = 16^\circ$ based on Mcdonald *et al.* [1971] and Armfield [1988]. It is to enforce a flow separation when the diffuser is subjected to a fully developed flow. The time-averaged velocity field is analysed before evaluating the instantaneous flow separation behaviour and unsteadiness. Lastly, the correlation between the emergence of separated flow and the distribution of the coherent structure is established.

5.2 Computational Set-Up

Prior to the parametric investigation of the wide opening angle diffusers $2\theta = 16^\circ$ subjected to a fully developed non-swirling inlet and solid-body swirling inlet, it is essential to first validate the time-averaged flow properties of the swirling inlet implementation and the conical diffuser with an opening angle $2\theta = 8^\circ$. As previously stated, the swirling implementation is validated with the pipe experiment undertaken by [Rocklage-Marliani *et al.* \[2003\]](#) while the conical diffuser calibration and validation ensue from the experimental study of [Okwuobi & Azad \[1973\]](#). All the simulations performed in this paper are summarised in [Table.5.1](#), PipeFu corresponds to the precursor simulation from which the cross-section instantaneous flow field (u,v,w) was extracted for 20000 time-steps after 40 Flow Through Passages to ensure the full development and convergence of the flow. The extracted data was prescribed as input to ensure accurate levels of turbulence into the swirling pipe simulation (PipeSw) and the conical diffuser simulations (CD8degFu, CD16degFu, CD16degSw), which respectively correspond to a $2\theta = 8^\circ$ diffuser with a fully developed inlet, a $2\theta = 16^\circ$ diffuser with a fully developed inlet and a $2\theta = 16^\circ$ diffuser with a prescribed swirling inlet. The first and second-order statistics ([Fig.5.3](#)) of the extracted flow were in good agreement with [Okwuobi & Azad \[1973\]](#) and [Laufer \[1954\]](#) experimental data. For this reason, the extracted data was prescribed without any modifications to the fully developed non-swirling conical diffusers simulation, CD8degFu and CD16degFu.

The most widely used methodology to prescribe a swirling inlet accurately in numerical investigations consists in representing the geometry of the swirling generator within the computational domain as demonstrated in [David \[2015\]](#) and [Mushatet *et al.* \[2020\]](#). For the representation of [Rocklage-Marliani *et al.* \[2003\]](#) rotating honey-comb swirling generator, the use of IBPs would be computationally expensive and cumbersome due to its complex geometry. It would require an extremely refined mesh to accurately capture the effective area of the 260 tubes composing the swirling generator. The implementation of the swirling inlet was inspired from [Escue & Cui \[2010\]](#) methodology, the mean axial and tangential velocities located at the station $x/D=4$ of the experiment are prescribed to the

CONICAL DIFFUSER: IMPACT OF A SWIRLING INLET ONTO THE
FLOW-SEPARATION BEHAVIOUR

$\Delta x(m)$	0.001	$\Delta y(m)$	0.0005	$\Delta z(m)$	0.0005			
Sim	lx (m)	ly (m)	lz (m)	nx	ny	nz	Ne (M)	Ne-Op (M)
PipeFu	0.3	0.12	0.12	300	240	240	17.28	17.28
PipeSw	1.1	0.12	0.12	1100	240	240	63.36	63.36
CD8degFu	0.92	0.24	0.24	920	480	480	211.97	105.63
CD16degFu	0.6	0.24	0.24	600	480	480	138.24	55.9
CD16degSw	0.6	0.24	0.24	600	480	480	138.24	55.9

Table 5.1: Mesh resolution and configuration of the simulations

inlet condition while the mean radial velocity is set up to zero. [Rocklage-Marliani *et al.* \[2003\]](#)'s rotating honey-comb swirling generator alters significantly the turbulence profile of the incoming pipe flow. For this reason, the fluctuation data extracted from PipeFu was subjected to numerous modifications to closely match the second-order statistics of experimental station $x/D=4$. In [Fig.5.2](#) a parabolic damping function was used to correct PipeFu's level of fluctuations. The juxtaposition of the mean flow properties and the damped fluctuation data enables a precise representation of the incoming swirling inlet instantaneous flow field. The main advantages of this methodology is its ability to reproduce any axisymmetric swirling outlet exiting a swirling generator if the first order and second-order statistic profiles are available. Another challenge lied in transforming the Polar velocity field into Cartesian velocity field to enable its resolution in Hydro3D, the procedure is detailed as followed:

- The instantaneous Cartesian velocity fluctuations (u',v',w') are extracted from the precursor simulation PipeFu.
- The instantaneous Cartesian velocity fluctuations (u',v',w') data is changed into Polar velocity fluctuations (Vx',Vr',Vt') data applying a rotation matrix ([Eq.3.3](#)).
- Calibrate the coefficient of the parabolic damping function to match [Rocklage-Marliani *et al.* \[2003\]](#)'s inlet experimental data.

- Apply the damping function onto all the instantaneous polar velocity fluctuation data files.
- Import the mean radial flow characteristic $\overline{Vx}, \overline{Vr}, \overline{Vt}$ from the Rocklage $x/D=4$ section.
- At each time step import the processed instantaneous polar velocities fluctuations data, calculate instantaneous polar velocities ($Vi = \bar{V}i + Vi'$).
- Transform the instantaneous polar velocities into instantaneous Cartesian velocities using the rotation matrix.
- Prescribe the instantaneous Cartesian velocities as inlet boundary condition.
- Once the flow field is resolved for one time-step transform the Cartesian instantaneous velocities into Polar instantaneous values the inverse of the rotation matrix.

The average of the inlet velocity profile of all simulations converges to bulk streamwise velocity of $U_b = 0.6791m/s$, which corresponds to a Reynolds number $Re = 69000$. A Neumann condition was set up as outlet boundary while the top, bottom, south and north boundary conditions of the computational domain consist of a no-slip condition.

The simulations all have the same circular inlet of radius $R = 0.0508$, the precursor pipe is 0.3m long while the swirling pipe length is 1.1m. The conical diffuser shares the same area ratio of $AR=4$ with an outlet radius of $R_{out} = 0.10116$ but Okwuobi & Azad [1973] diffuser is approximately twice as long as the wide-angle diffusers with a respective length of 0.7196m and 0.3583m. The small-angle diffuser is imparted of a cylindrical tail section measuring 0.2m while the wide-angle diffuser tail-section length is 0.24m. The tail-sections were added to the computational domain because Cherry *et al.* [2008] experimental research depict large pressure gradient in these sections suggesting that pressure recovery does not exclusively occur in the expansion part of the diffuser. The wide-angle diffuser was chosen to enforce flow separation development when prescribing a fully developed

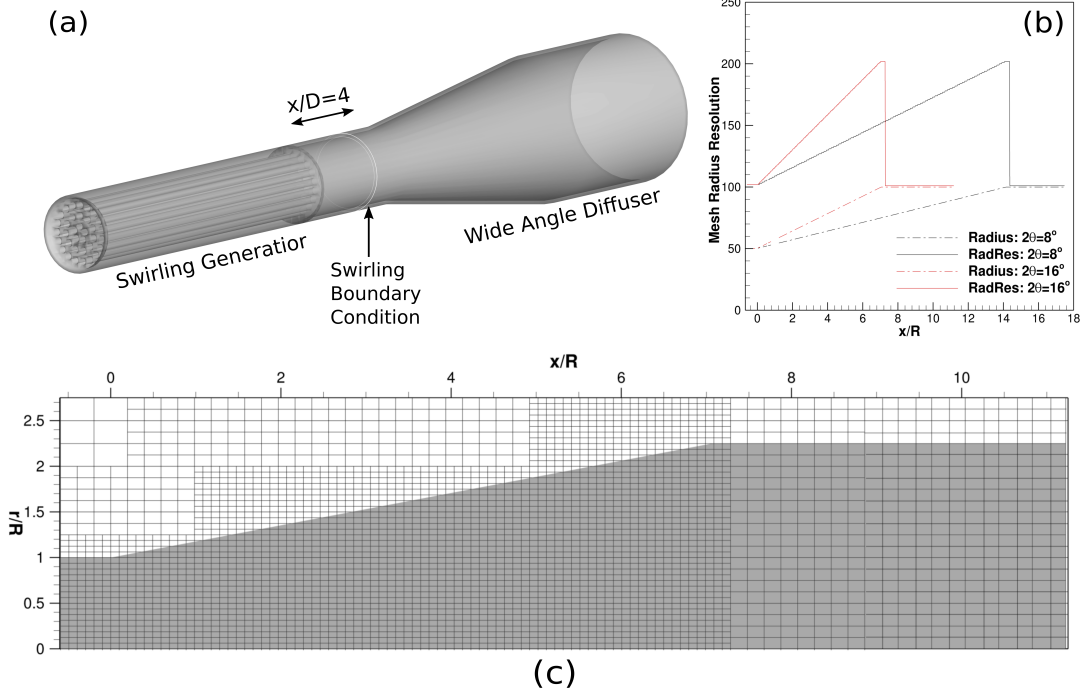


Figure 5.1: (a) Three-dimensional representation of the swirling generator and the wide opening angle conical diffuser, (b) Evolution of the radius number of cells along the diffuser, (c) Two-dimensional representation of the computational domain for the wide opening angle conical diffuser (Grid points only plotted every four points for clarity)

non-swirling inlet so inevitably the pressure recovery will still be ongoing in the tail-section.

The staggered Cartesian mesh does not body fit the flow field of the diffusers, herein an LMR strategy with three different levels illustrated in Fig.5.1c was set-up to coarsen the computational sub-domains extensively outside the diffuser effective flow field. The tail-section was also coarsened by one level; overall it significantly reduces the computational cost of the conical simulations. Table.5.1 shows the mesh refinement before the optimisation Ne and after Ne-Op, the LMR strategy reduces the computational mesh by 50% in CD8degFu and 40% in CD16degFu, CD16degSw. The most refined LMR level present a resolution of $\Delta x = 0.001, \Delta y = 0.0005, \Delta z = 0.0005$ which translate in wall unit to

$\Delta x^+ = 3, \Delta y^+ = 1.5, \Delta z^+ = 1.5$. The selection of this specific mesh refinement ensue from a grid sensitivity analysis; this detailed analysis is not presented in this paper. The results revealed the development of instabilities and mean reversal flow at the throat of Okwuobi & Azad [1973] conical diffuser when the radius of the inlet pipe contained less than 100 cells. All the simulations, PipeFu, PipeSw, CD8degFu, CD16degFu and CD16degSw were performed on the Supercomputing-Wales cluster using respectively 192,640,960,932 and 932 AMD EPYC (Rome) processor chips. Apart from the precursor simulation, the first-order statistics were calculated after 25 FTPs while the second-order statistics were monitored after 35 FTPs. A variable time step with a constant Courant-Fredrichs-Lewy (CFL) equal to 0.5, ensuring the numerical stability of the simulations.

5.3 Results and Discussion

5.3.1 Simulation calibration and validation

As previously stated, this research focuses on evaluating the characteristics of the mean and instantaneous flow separation within wide-angled conical diffuser when subjected to two different types of inlets: a fully developed axial inlet and a swirling inlet. To the author knowledge, there is no existing experimental research that provides detailed time-averaged flow properties of the aforementioned conditions. Herein, this section separately validates the ability of the LES software Hydro3D in representing accurately the flow field of Okwuobi & Azad [1973] diffuser and represent the swirling development within a Rocklage-Marliani *et al.* [2003].

The mean axial and tangential velocity profiles at five different stations along the pipe are represented in Fig.5.2c and Fig.5.3a. The mean axial velocity is quasi-constant along the five different stations $x/D=4,6.5,9,11.5,14$ along the pipe. The tangential momentum retains a solid-body distribution across the pipe but a small decay of the overall magnitude is displayed. The axial and tangential velocity

CONICAL DIFFUSER: IMPACT OF A SWIRLING INLET ONTO THE
FLOW-SEPARATION BEHAVIOUR

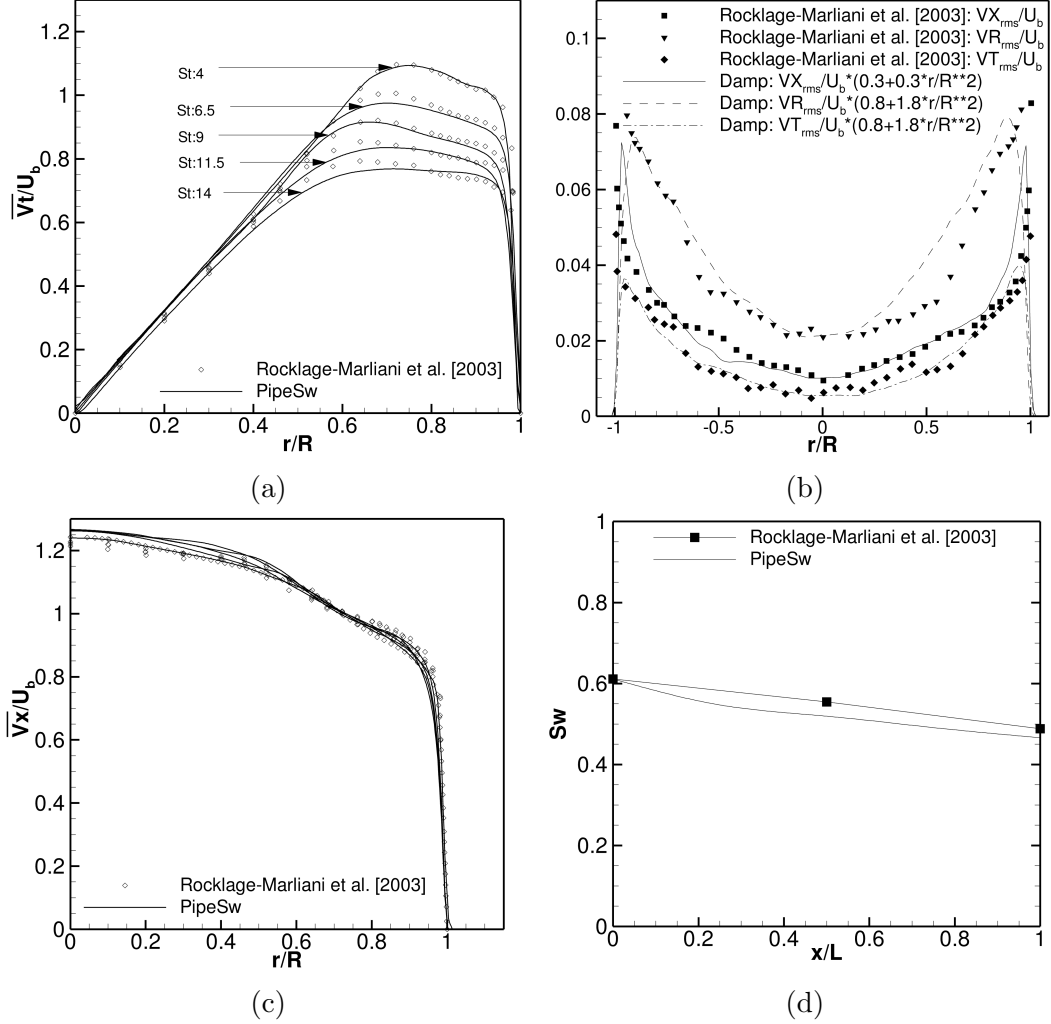


Figure 5.2: (a) Normalised mean tangential velocity \overline{V}_t/U_b at five different stations along the pipe, (b) Inlet normalised root mean square of the axial, radial and tangential velocity fluctuations and (c) Normalised mean axial velocity \overline{V}_x/U_b at five different stations along the pipe, (d) Swirling decay along the pipe

distribution results in swirling number dropping from $Sw=0.6112$ to $Sw=0.4666$, which is equivalent to swirling decay of 24%. The results of the mean flow properties are in good agreement with [Rocklage-Marliani *et al.* \[2003\]](#) experimental data, the LES results marginally under-predict the peak value of the tangential velocities near r/R , while the axial velocities are slightly over-predicted. It results in a small over-prediction of the swirling decay, nevertheless, the accuracy of the

CONICAL DIFFUSER: IMPACT OF A SWIRLING INLET ONTO THE
FLOW-SEPARATION BEHAVIOUR

simulation results are more than satisfactory to prescribe this swirling inlet for the parametric study with confidence.

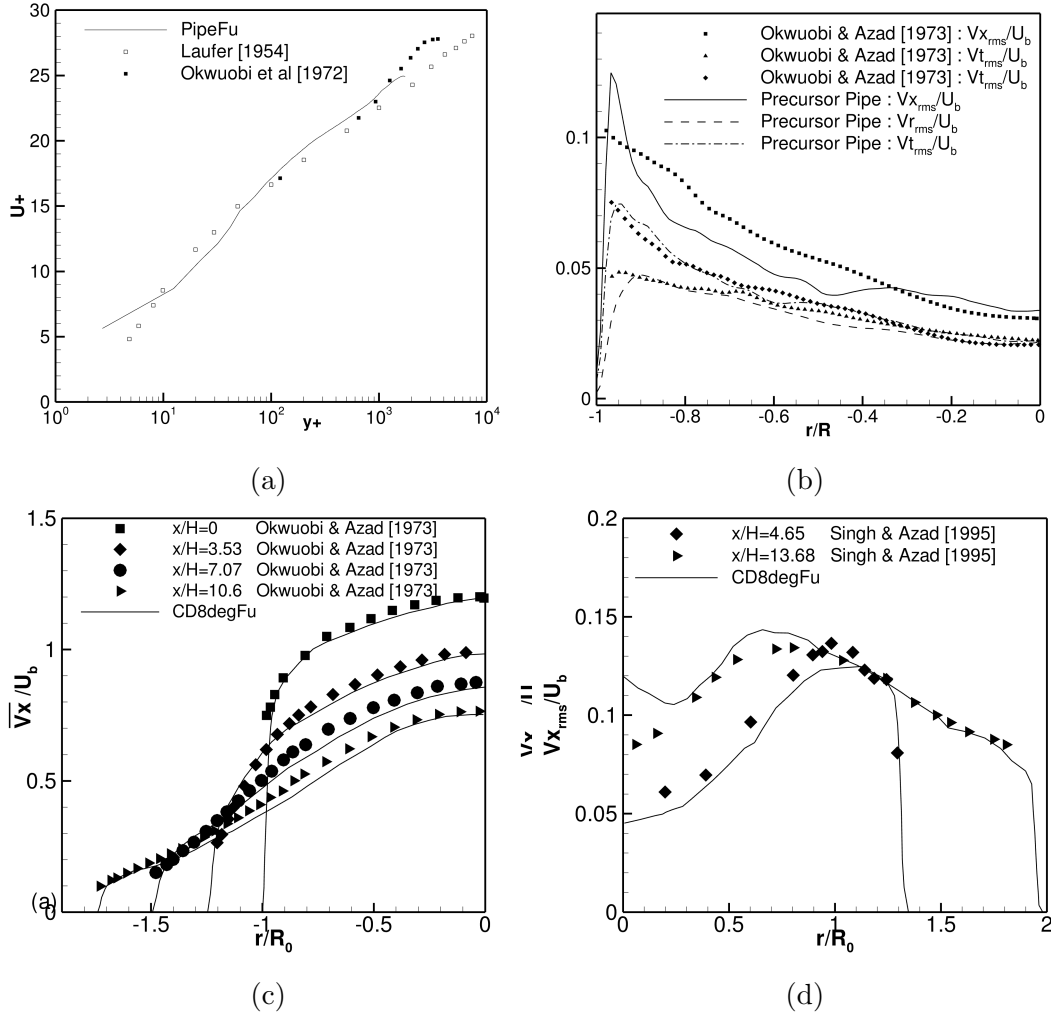


Figure 5.3: (a) Dimensionless mean axial velocity profile U^+ , (b) Inlet normalised root mean square of the axial, radial and tangential velocity fluctuations, (c) Normalised mean axial velocity profiles \bar{V}_x/U_b at four locations along CD8degFu, (d) Normalised root mean square of the axial velocity fluctuations Vx_{rms}/U_b at two locations along CD8degFu

The validation of the conical diffuser is shown in Fig.5.3a-d, Fig.5.3a corresponds to the flow property profile extracted from the precursor flow, it represents to dimensionless streamwise mean velocity profile across the radius of the fully de-

veloped pipe flow and is in good agreement with the law of the wall and previous experimental pipe Laufer [1954] and the experimental diffuser Okwuobi *et al.* [1972] studies. Fig.5.3b corresponds to the root mean square of the axial, radial and tangential fluctuations at the inlet of the CD8degFu. The radial and tangential fluctuations are in excellent agreement with the Okwuobi & Azad [1973] experimental data while axial fluctuation gradient along r/R is slightly more abrupt in the LES results but remains a relatively good agreement with the data. The simulation captures with great accuracy the progressive deceleration of the mean axial flow when compared with experimental data at the $x/R=0,3.53,7.07,10.6$ when subjected to a high adverse pressure gradient. The root mean square of the axial fluctuation exhibits a small asymmetry, the lowest fluctuation peak is located at $r/R_0 = 0.25$ of $x/R = 4.65$. The fluctuation distribution and magnitude remain in relatively good agreement with Singh & Azad [1995a] experimental data. The high-resolution LES simulations of the two cases performed and provided accurate results to support the parametric study of CD16degFu and CD16degSw.

5.3.2 Time-averaged flow field

The deceleration of the mean axial flow within the three diffusers CD8degFu,CD16degFu and CD16degSw is compared in Fig.5.4. As previously mentioned, the CD8degFu is doubled the length of CD16degFu and CD16degSw, herein to facilitate the comparison of the flow field the length is expressed in term of area ratio defined by McDonald & Fox [1966] as:

$$AR = 1 + 2 * \frac{x}{R_0} * \tan(\theta) + \left(\frac{x}{R_0} * \tan(\theta)\right)^2 \quad (5.1)$$

where R_0 corresponds to the inlet radius and θ is the opening angle. The axial momentum distribution differs slightly near the throat of the diffuser between CD8degFu and CD16degFu but rapidly CD16degFu exhibit low momentum zones near the bottom wall shifting the position axial position of the core flow. The

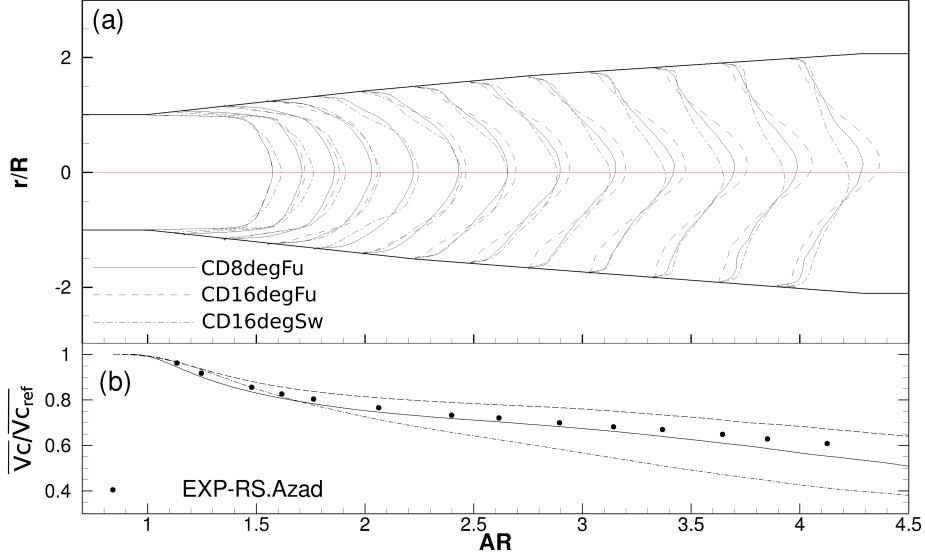


Figure 5.4: (a) Normalised mean axial velocity \overline{V}_x/U_b along the conical diffusers normalised length (AR), (b) Normalised mean axial velocity of the conical diffusers centerline $\overline{V}_c/\overline{V}_{c_{ref}}$ along the normalised length AR

magnitude of the core flow is also significantly stronger at the exit of CD16degFu than CD8degFu. The strong adverse pressure gradient of CD16degFu impeded on the stability and the deceleration of the axial velocity. The axial momentum exiting the swirling generator and incoming the conical diffuser exhibits a profile distribution with a slightly stronger core. CD16degSw evinces localised low-momentum areas between $AR \in [1, 2]$ reduces the negative velocity gradient compared to CD8degFu. Subsequently, the tangential velocity appears to enforce a more significant deceleration to the axial flow field within CD16degSw in contrast to CD8degFu. The axial flux appears to be greater in CD8degFu than in CD16degSw. This difference is quantified by extracting and analysing the axial velocity centreline of the diffusers as demonstrated in Fig.5.4b. Firstly, the centreline axial velocity of CD8degFu is in relatively good agreement with Azad [1996] experimental results, at this location the flow exhibit a deceleration of 43%. When the conical diffuser is only subjected to a geometrical change (length divide by 2), CD16degFu axial velocity only drops by 32% revealing the impact of the adverse pressure gradient onto the conversion of the dynamics pressure into static pressure. The negative effect can be counter-pressure with tangential

momentum enforced by the swirling inlet. Its influence is significant; it reduces the inlet velocity by 53% when reaching the exit. The impact of low momentum zone near the throat of CD16degSw is also perceived in Fig.5.4b. The centerline of the axial velocity of CD8degFu and CD16degSw intersect at AR=1.7. At the beginning of the diffuser, CD8degFu has a stronger negative velocity gradient than CD16Sw, it can be explained by the presence of a small recirculation zone at this location in CD16Sw as shown in Fig.5.8b.

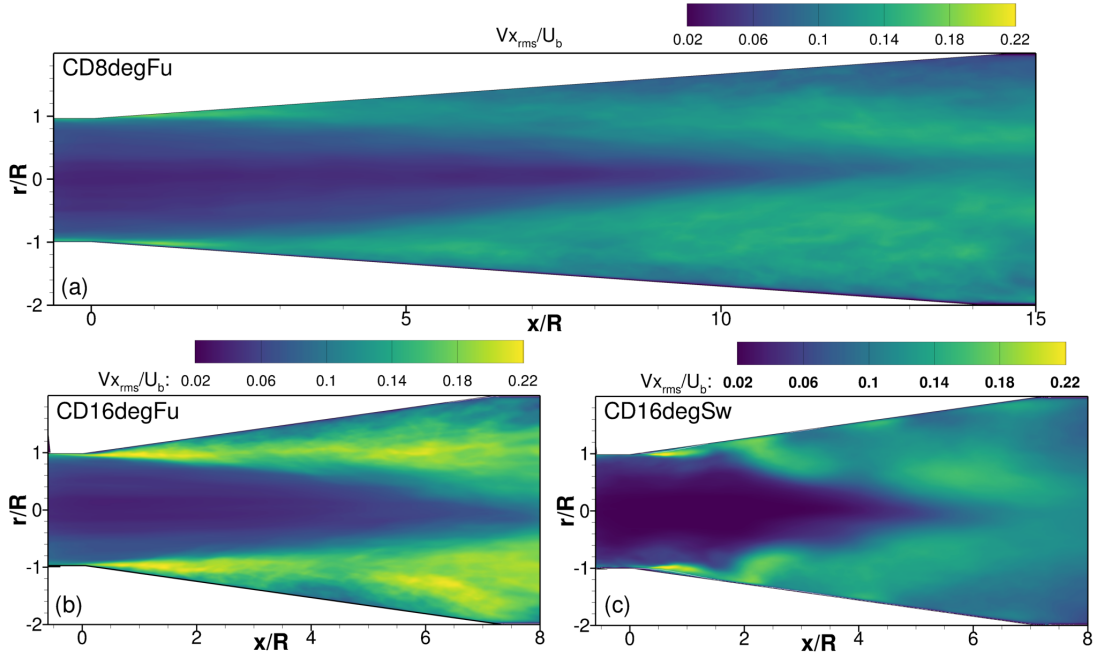


Figure 5.5: Normalised root mean square of the axial fluctuations Vx_{rms}/U_b along the three conical diffusers

The contour of the normalised root mean square of streamwise fluctuation for each diffuser is shown in Fig.5.5. There is a significant difference in the development of shear stress in between the infinitesimal layers of the flow when the inlet boundary condition is fully developed or swirling. The highest shear zones are located immediately after the opening of the diffuser ($x/R=0.3$) in all cases. For the fully turbulent inlet, the line of the highest turbulent level is located just under their interfaces with the core where the shear stress level are the lowest. The magni-

tude of the streamwise shear stress is double in CD16degFu when compared to CD8degFu. One might suggest that this difference in magnitude is proportional to the opening angle and in turn, the adverse pressure gradient. In CD16degFu, a clear asymmetry is observed, including a very high shear region in between the core low shear region and the recirculation zone represented by the white line contour. The presence of high streamwise shear stress in the vicinity of the back-flow region is a typical phenomenon depicted in many other studies on separated flow. This high turbulent zone is not present at the top of the diffuser because no mean flow separation is depicted at this location. The swirling inlet induced completely different dynamics into the development of the streamwise shear layers. The tangential velocity is altered and dissipated much more efficiently the initial high shear zone located at ($x/R=0.3$). The flow separation emerges from the great strain events accounted by the turbulent kinetic energy (TKE). The TKE displays similar proclivities to the streamwise shear stress in Fig.5.6. A high magnitude momentum zone is located at the vicinity of the flow separation in CD16degFu while being absent in CD16degSw. The low TKE regions represent the core flow, it extends up to $AR=3.5$ in CD16degSw, while reaching $AR=3.75$ and $AR=4.25$ respectively in CD8degFu and CD16degSw. The core flow dissipates at a much faster pace in CD16degSw where the null TKE region is much greater than in CD8degFu and CD8degFu. It suggests that the tangential momentum improve the stability of the core flow.

The Fig.5.7b presents the one-dimensional wall pressure coefficient also defined as the recovery. The efficiency and performance of the conical diffusers are evaluated by the ratio actual pressure recovery against the ideal pressure recovery in which the flow is considered inviscid. This pressure coefficient is good agreement with Okwuobi & Azad [1973] experiment, at the exit of the diffuser, 71% of the dynamics pressure incoming the diffuser has been transformed into static pressure. CD16degFu experienced a much greater adverse pressure gradient reducing significantly its performance (50%), experiencing a drop in efficiency of 21% compared to CD8degFu. The tangential momentum exiting the swirling generator improves substantially the performance in CD16degSw, reaching nearly the same efficiency as CD8degFu for half the length of this diffuser. However, its recovery

CONICAL DIFFUSER: IMPACT OF A SWIRLING INLET ONTO THE
FLOW-SEPARATION BEHAVIOUR

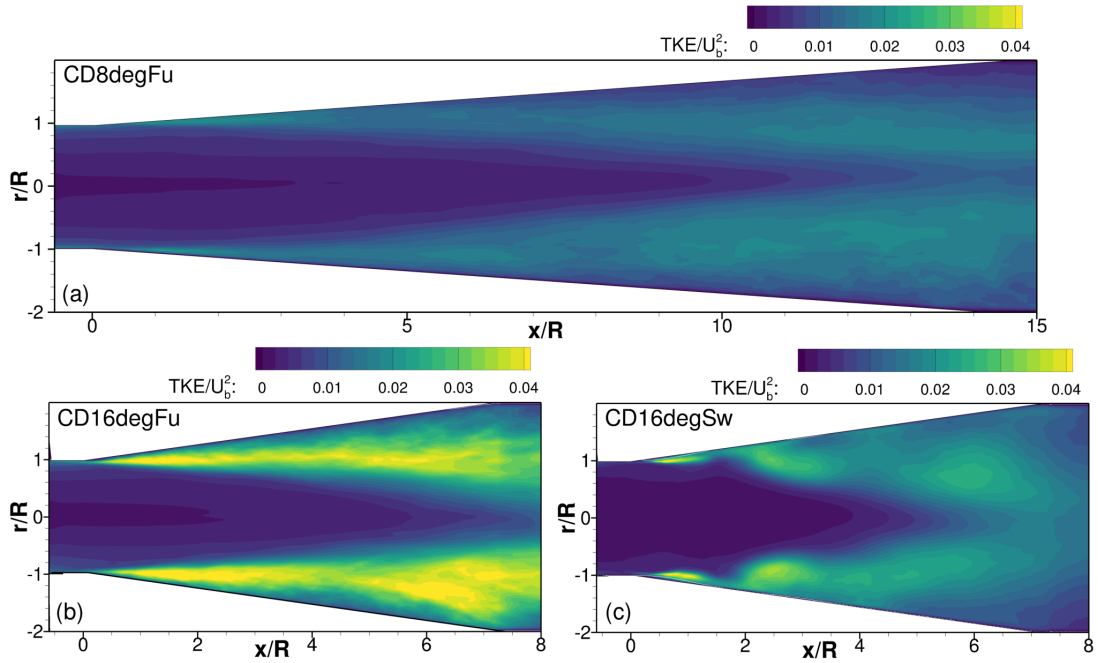


Figure 5.6: Normalised turbulent kinetic energy TKE/U_b^2 along the three diffusers

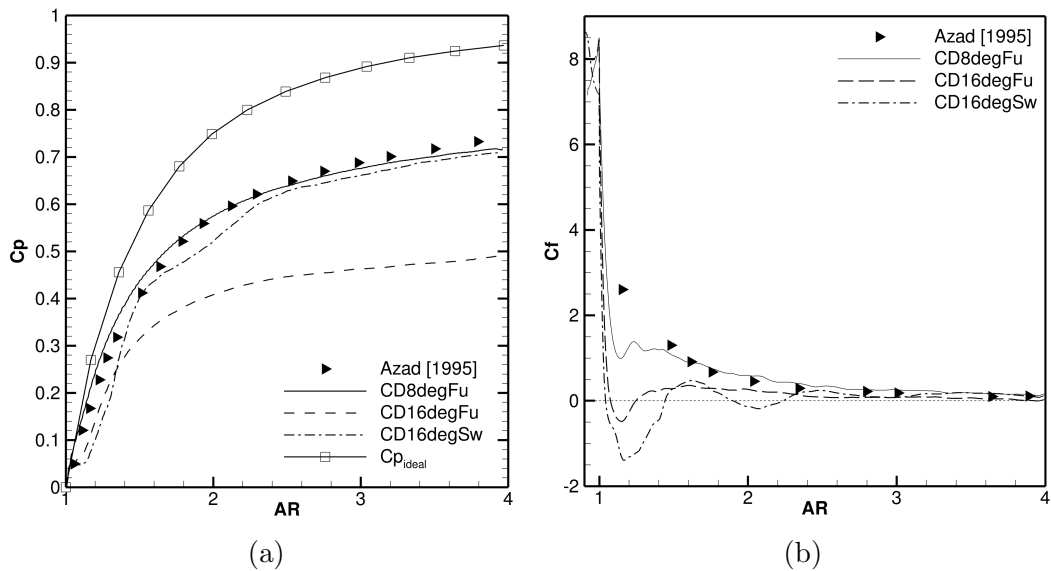


Figure 5.7: (a) One-dimensional wall pressure coefficient C_p , (b) Skin Friction coefficient C_f along the conical diffusers

is not as smooth and continuous as the narrow-angle diffuser. It is consistent with the experimental findings of *McDonald et al.* [1971]. For an expansion angle of 15.8° and an area ratio of 4.48 subject to three different solid body swirls the improvement in efficiency range from 9% to 25%. Near the throat of the diffuser at $AR=1.1$ it reveals an inflection point, another one can be depicted at $AR=2$. The friction coefficient evidently explains why the drop in the pressure recovery gradient occurs (Fig.5.7b). For CD16degSw, the friction coefficient displays a large negative peak at $AR=1.2$ which herald the existence of a mean backflow region, another peak with a much-reduced magnitude is observed at $AR=2$. It puts into evidence the significant impact that has the development of separated flow onto the pressure recovery and the performance of a diffuser.

5.3.3 Unsteadiness of the flow separation

The impact of the flow separation on the efficiency was previously identified with the pressure coefficient (Fig.5.7a) and the skin friction at the wall. The flow separation blockage effect impeded of the negative velocity or deceleration gradient of the incoming flow, which translated in a decrease of the pressure recovery. The section quantifies the size of this separated flow and investigates the unsteadiness of the instantaneous separated flow.

Independently to the inlet condition, a mean backflow region is detected at the beginning of both CD16degFu and CD16degSw in Fig.5.8. The iso-surface of CD8degFu is not provided as only mean residual flow separation bubbles due to the IBPs are present. Moreover, the shape of the recirculation zones near the inlet differs, the shape is annular when the incoming flow is non-swirling and is supposedly due to the sharp corner connecting the inlet pipe to the diffuser. When the flow is endowed with a high tangential momentum, four larger backflow bubbles form at the top, bottom and sides of CD16degSw which will in a later analysis be linked to the detachment of high energy containing motions. The Fig.5.8 reveals the impact that has the tangential momentum onto the development of the mean flow separation. Contrarily to the fully developed inlet where a small portion of

CONICAL DIFFUSER: IMPACT OF A SWIRLING INLET ONTO THE
FLOW-SEPARATION BEHAVIOUR

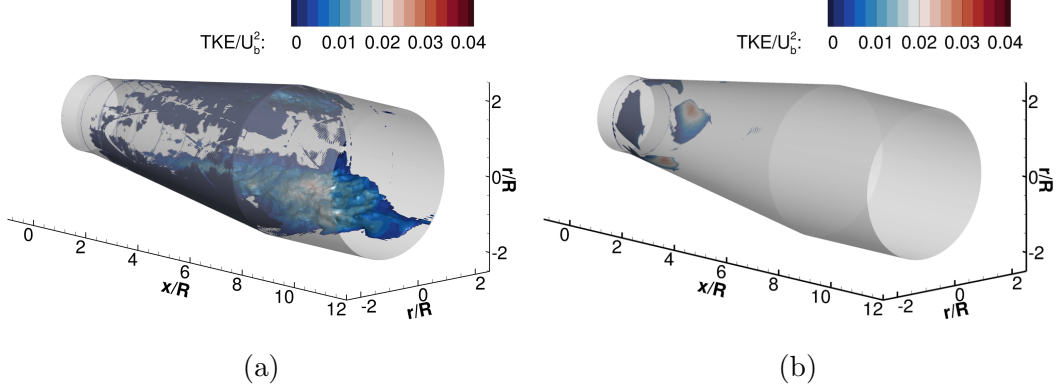


Figure 5.8: Iso-Surface of the mean streamwise velocity $\overline{V}_x = -0.005$ with TKE/U_b^2 contour: (a) CD16degFu (b) CD16degSw

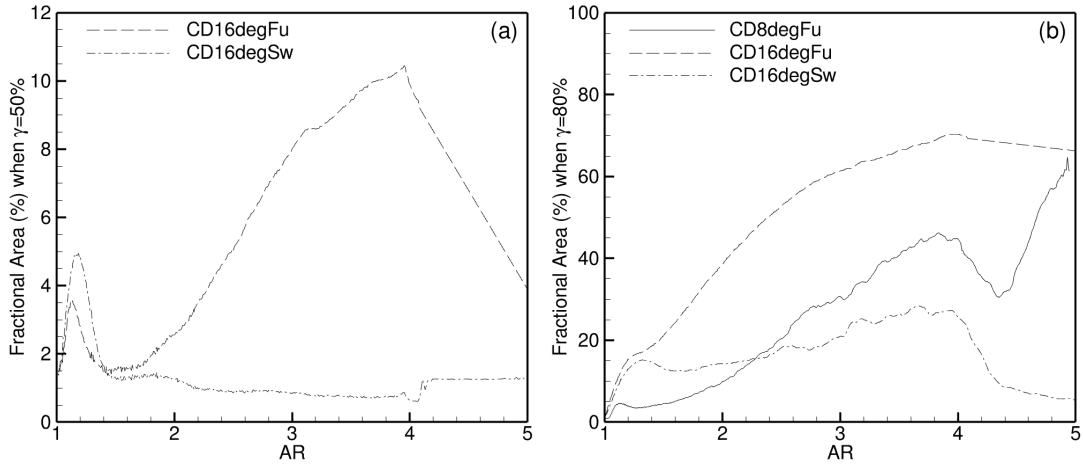


Figure 5.9: Fractional area of the reversal flow along the three conical diffusers with backflow coefficient: (a) Mean : $\gamma = 50\%$, (b) Intermittent : $\gamma = 80\%$

the throat separated flow trails and grows toward the exit of the diffuser, the mean backflow region does not develop further than its four localised bubbles between $x/R=0$ and $x/R=1$. This qualitative analysis is supported and quantified by the fractional area (FA) of the reversal flow across the diffuser (Fig.5.9). The analysis was previously used by [Cherry *et al.* \[2008\]](#) to assess the development of the three-dimensional asymmetric rectangular diffuser. The fractional area of the mean recirculation zone extends between $AR=1$ and $AR=1.4$ regardless of the inlet flow conditions. Nevertheless, the separated flows volume is greater

in CD16degSw than in CD16degFu with a respective FA peak of 5% and 3.5%. Subsequently, the fractional area occupied by the reversal flow in CD16degSw quickly decrease and stabilise at 1%, which, similarly to CD8degFu is considered to be residual separation located the immersed boundary point (IBP). In CD16degFu, the lowest FA=1.8%, occupied by the flow separation is established between AR=1.4 and AR=1.8 prior the development of the main flow separation around the exit of the diffuser where the highest FA peak takes approximately 10.5% of the cross-section AR=3.8. The integration of the fractional area along all the slices included in the diffuser enables the calculation of the mean flow separation volume. The volume is drastically reduced when a high tangential velocity is prescribed at the inlet. Indeed, the flow separation size in CD16degFu is 6.2% while being of 2.05% in CD16degSw. It is also interesting to depict that the intermittent transitory detachment in CD8degFu becomes more significant than in CD16degSw at AR=2.3. The tangential velocity effectively reduce the growth of the instantaneous flow separation.

The unsteadiness levels of the instantaneous separated flow is further investigated in Fig.5.10. Similarly to Chapter.4, the unsteadiness of the flow separation at specific region is evaluated using Simpson [1996] backflow coefficient. The assessment of the centreline vertical plane reveals great divergence when comparing the three diffusers in Fig.5.10, only CD16degFu is endowed of transitory detachment originating at the junction between the exit of the diffuser and the extension part (AR=4). Although ITD regions can be depicted in both CD8degFu and CD16degFu, the region is much more expand in CD16degFu and present both at the top ($AR \in [2.5, 4.8]$) and bottom ($AR \in [2, 6]$) region of the vertical plane while the narrow diffuser (CD8degFu) ITD is much more localised at the bottom of the slice between $AR \in [3, 5]$. The fractional area of the ITD give a better comprehension of the volume in which the separated flow developed and conveyed. The ITD region occupies the 15% of the fractional volume (FV) in CD8degFu, the geometrical change increase the ITD to 38% in CD16degFu. The impact of the inlet change overtakes the impact of the inlet as CD16degSw reduces the ITD volume to 9%.

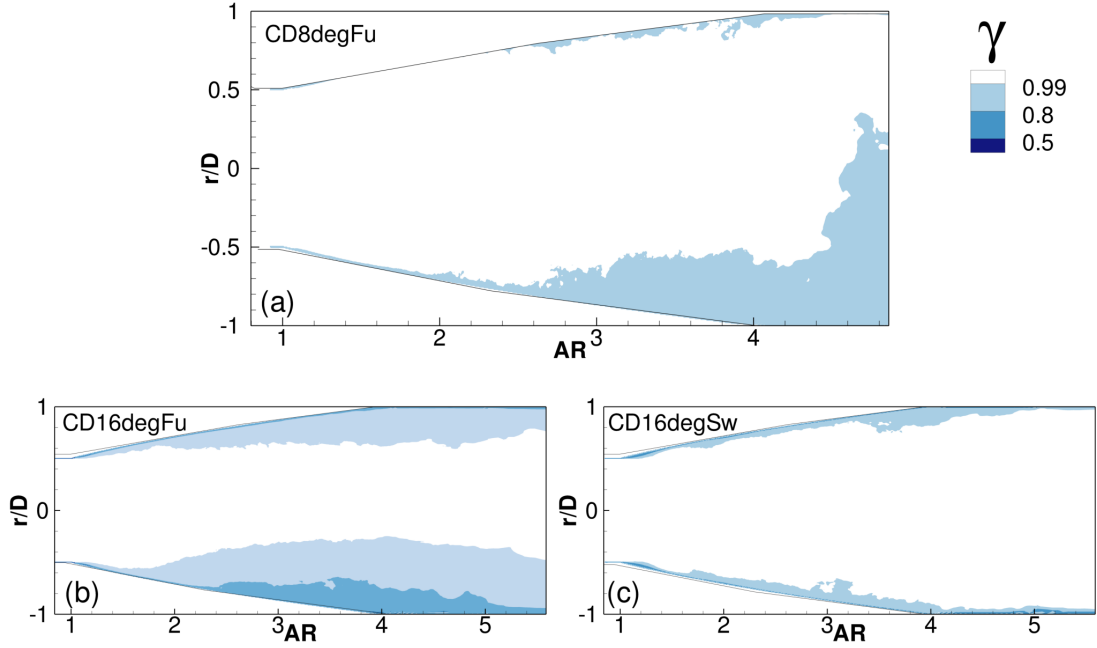


Figure 5.10: Backflow coefficient contour within the three conical diffusers: (a) CD8degFu (b) CD16degFu (c) CD16degSw

The cumulative fractional volume occupied by all the instantaneous backflow pocket was monitored at each time-step for a computational time of 45s in CD16degFu and CD16degSw as showed in Fig.5.11a. These time-series also capture a much larger backflow volume (BV) in CD16degFu than in CD16degSw as the averaged backflow volume these samples respectively inhabit 6.2% and 2.0% of the diffusers. When no substantial tangential momentum is present in the flow field, it facilitates a longer growth period of the cumulative recirculation zones in CD16degFu. Although, the backflow volume fluctuated an overall growth of BV can be observed in CD16degFu between $t \in [6, 28]$ peaking to 9.5% of the diffuser fractional volume just before being washed away by the streamwise momentum and abruptly dropping by 5.7%. This phenomenon does not occur when the flow is subjected to a swirling inlet, BV only fluctuates between 1.2% and 3.36%. The Fig.5.11b and Fig.5.11c correspond to the Fast-Fourier Transformation (FFT) of CD16degFu and CD16degSw BV signal. Unfortunately, no periodicity can be distinctively identified in the CD16degFu FFT, the behaviour of the instantaneous

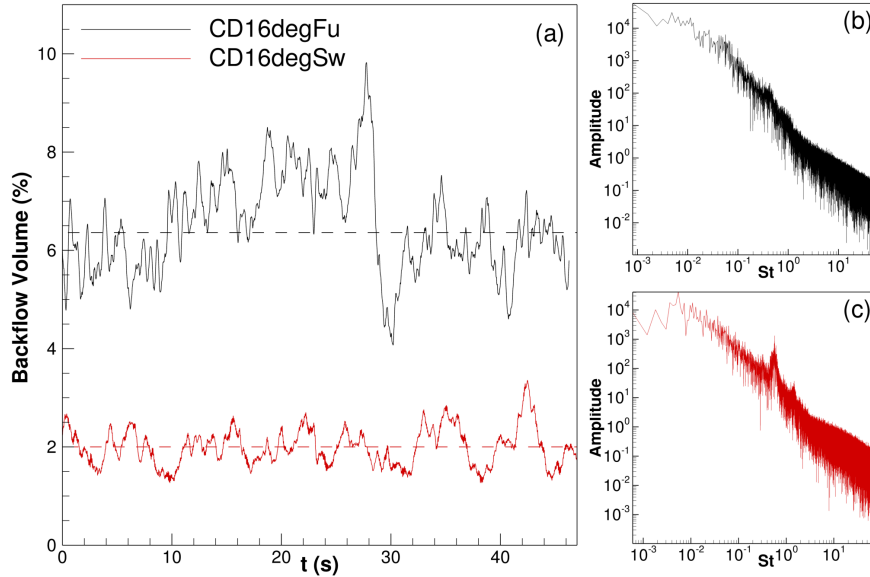


Figure 5.11: (a) Total instantaneous backflow fractional volume time-series within the two wide opening angle conical diffusers, (b) FFT: CD16degFu, (c) FFT: CD16degSw

reversal flow seems to be too chaotic to characterise any growth and reduction phase. However, a distinctive frequency is depicted in the FFT of CD16degSw, its dimensionless periodicity defined by the Strouhal number is equal to $St=0.57$. The unsteadiness level of BV is measured using the root mean square of the fluctuation time-series. The small size reversal flow in the CD16degSw ensue from a fast dissipation of BV leading to higher levels of unsteadiness with $BV_{rms} = 19\%$. In contrast, $BV_{rms} = 9.7\%$ in CD16degFu where the cumulative reversal flow exhibits a longer period of growth (Fig.5.11a). It suggests that the reversal flow growth and reduction periodicity is a bit slower than in the three-dimensional asymmetric rectangular diffuser where $St=0.7$. It might be due to the greater flow stability provided by tangential velocity detailed in the Section.5.3.5 which reduces the growth of the instantaneous reversal flow.

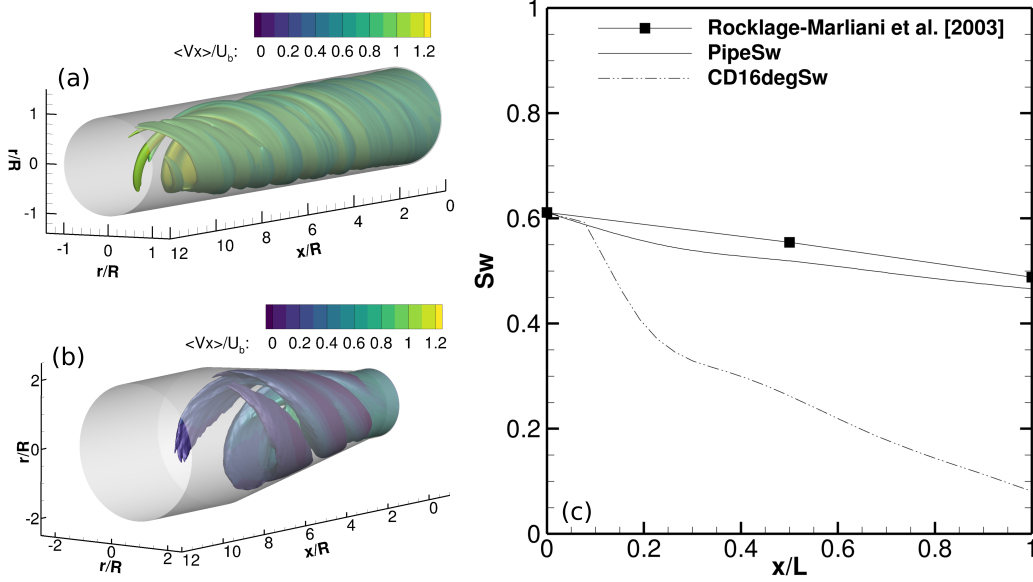


Figure 5.12: Iso-Surface of the normalised mean tangential velocity \overline{V}_t/U_b with a iso-contour of the normalised mean axial velocity \overline{V}_x/U_b : (a) PipeSw, (b) CD16degSw, (c) Swirling decay along PipeSw and CD16degSw

5.3.4 Swirling decay

The swirling decay corresponds to the swirling number gradient along the stream-wise axis (x/R) of the pipe or the conical diffuser. The swirling number also called swirling intensity characterises the ratio between the mean averaged axial and the tangential velocity:

$$Sw = \frac{2\pi\rho \int_0^R \overline{V}_x \overline{V}_t r^2 dr}{2\pi\rho R \int_0^R \overline{V}_x^2 r dr} \quad (5.2)$$

where ρ corresponds to the density, R is the radius of the cross-section, r defines the radial position while V_x and V_t are the axial and tangential velocity, respectively. The inlet swirling number is identical to Rocklage-Marliani *et al.* [2003] experimental measurement, $Sw_0 = 0.6112$. The iso-surface of the normalised mean tangential velocity showed in Fig.5.12a and Fig.5.12b clearly captures the impact of the adverse-pressure gradient onto the swirling decay. The swirl decay

was merely perceivable in the pipe when the magnitude of the tangential velocity was set under $\overline{V}_t/U_b < 0.9$ but at this value in the conical diffuser, the swirl would dissipate at $x/R=1$. For this reason, the magnitude of normalised tangential velocity selected to create the iso-surface differs between the pipe ($\overline{V}_t/U_b = 0.9$) and the diffuser ($\overline{V}_t/U_b = 0.6$).

In Fig.5.12c, disparities between PipSw and CD16degSw are depicted. The swirling decay gradient is substantial and exponential in CD16degSw while being gradual and linear in PipeSw. The swirling intensity displays a linear decay along the pipe section prior to the expansion section of the conical diffuser ($x/L \in [0, 0.8]$). The swirling decay experienced an abrupt drop as soon as it enters the expansion section. It evidences the significant impact of the adverse pressure gradient on the decay of the swirl intensity within conical diffusers. The swirling intensity in PipeSw experiences a drop of 0.145 when reaching the exit, corresponding to a 23% drop from the inlet swirling number. Moreover, CD16degSw swirling intensity reduces by 0.53 at the exit and is between three to four times greater than in PipeSw. It is equivalent to a decline of 80% from the diffuser inlet swirling number. The same exponential decay nature of the swirling intensity was previously observed in [Dauricio & Andrade \[2017\]](#) numerical study on wide opening angle conical diffusers.

5.3.5 Instantaneous flow

Many analytical proposals that identify and classify the turbulent eddies from the vector field has been set forth. The analysis of this section is based on [Kline & Robinson \[1989\]](#) definition also supported by [Adrian *et al.* \[2000a\]](#), which states:”A vortex exists when instantaneous streamlines mapped onto a plane normal to the core exhibit a roughly circular or spiral pattern, when viewed in a reference frame moving with the center of the vortex core”. The instantaneous vector field of the cross-sections located at AR=1.74 and AR=2.71 along the three diffusers is shown in Fig.5.13. The vector length was set to be 0.4% of each diffuser cross-section frame to ensure an accurate comparative analysis. [Kline \[1959\]](#)

CONICAL DIFFUSER: IMPACT OF A SWIRLING INLET ONTO THE FLOW-SEPARATION BEHAVIOUR

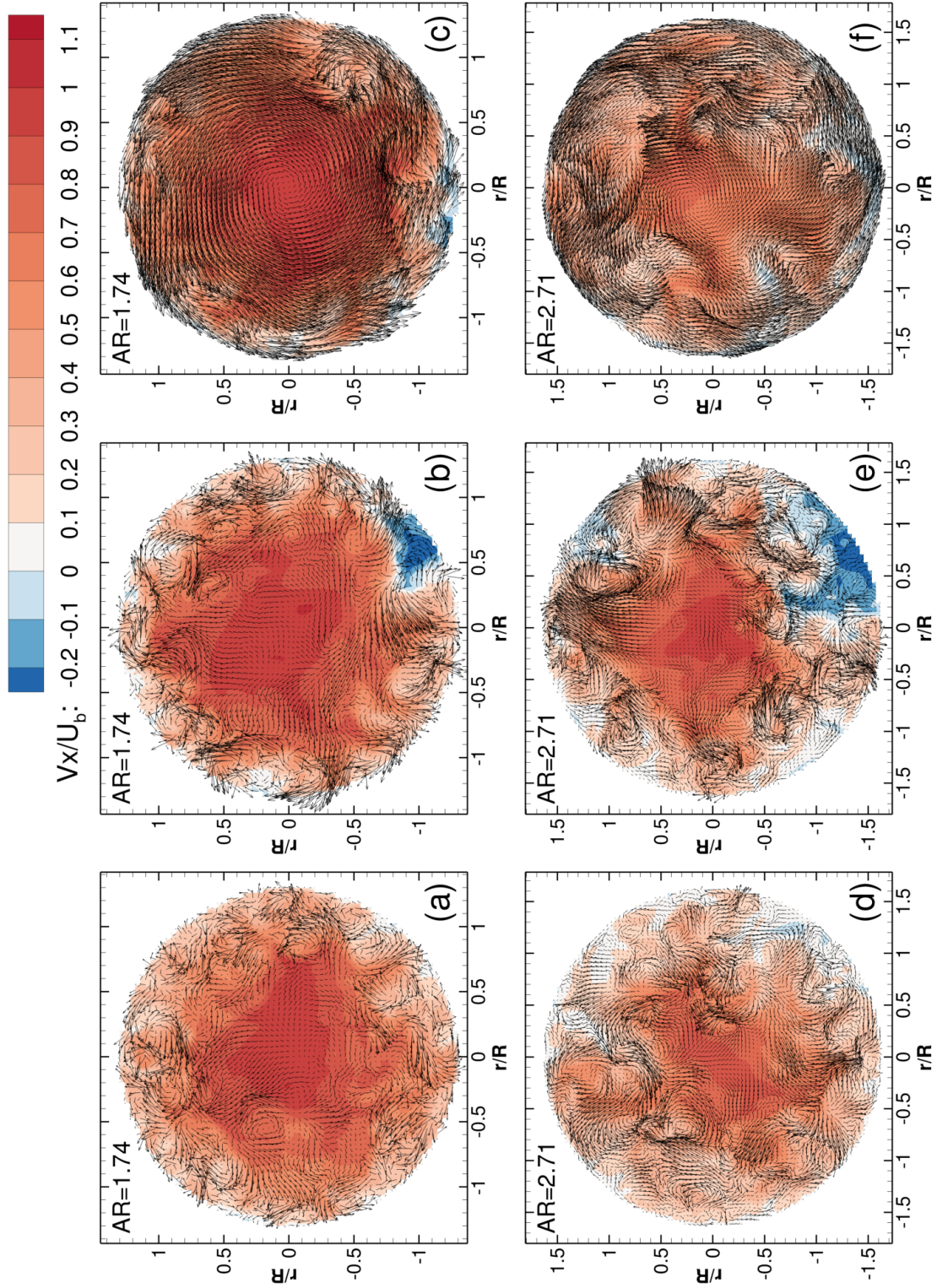


Figure 5.13: Cross-section vector field at two different locations ($AR=1.74, 2.71$) within three conical diffusers: (a,d) CD8degFu, (b,e) CD16degFu, (c,f) CD16degSw

, [Meinhart & Adrian \[1995\]](#) suggests that instantaneous backflow regions are induced by an alignment of a multitude of hairpin vortices in a streamwise coherent pattern. A multitude of circular patterns is depicted near the wall of CD8degFu and CD16degFu at AR=1.74 indicating the presence of quasi-streamwise and cane hairpin vortices in Fig.5.13a and Fig.5.13b ([Adrian *et al.* \[2000a\]](#)). The coherent structure distribution across these two cross-sections form an annular 'beam pattern' of hairpin packets develops along the length of the diffuser. These hairpin packets induce long-lasting low momentum regions within the inner and outer regions of the turbulent boundary layer ([Adrian *et al.* \[2000b\]](#)). Although the distribution and magnitude of the circular patterns are very similar in both Fig.5.13a and Fig.5.13b, instantaneous reversal flow has already burst from the boundary layer in CD16degFu. It suggests that instantaneous flow separation emerge and development only occurs (Fig.5.13b-e) when a high negative velocity gradient is superimposed with a significant adverse-pressure gradient as induced in CD16degFu by the wide opening angle. This juxtaposition in CD8degFu is not substantial enough to enforce the turbulent boundary layer detachment and the development of large recirculation zones. In Fig.5.13a minuscule zones of instantaneous reversal flow is observed at AR=1.74 but contrarily to CD16degFu this separated flow does not grow extensively and is fully dissipated in CD8degFu at AR=2.71.

The tangential velocity prescribed by the upstream swirling generator alters the distribution and the arrangement of the energy-containing motions significantly. The vector field in Fig.5.13c-e exhibits a lot less circular patterns than in CD8degFu and CD16degFu. It appears that the tangential momentum prevents or dissipates extremely rapidly the small energy-containing motions while sweeping away the larger hairpin vortices from the wall towards the core the larger of the conical diffuser. This centrifuge force prevents the alignment of quasi-streamwise vortices and the development of long-lasting low momentum region within the turbulent boundary layer, which is responsible for the emergence of reversal flow.

Numerous prediction models have been developed by the scientific community

CONICAL DIFFUSER: IMPACT OF A SWIRLING INLET ONTO THE
FLOW-SEPARATION BEHAVIOUR

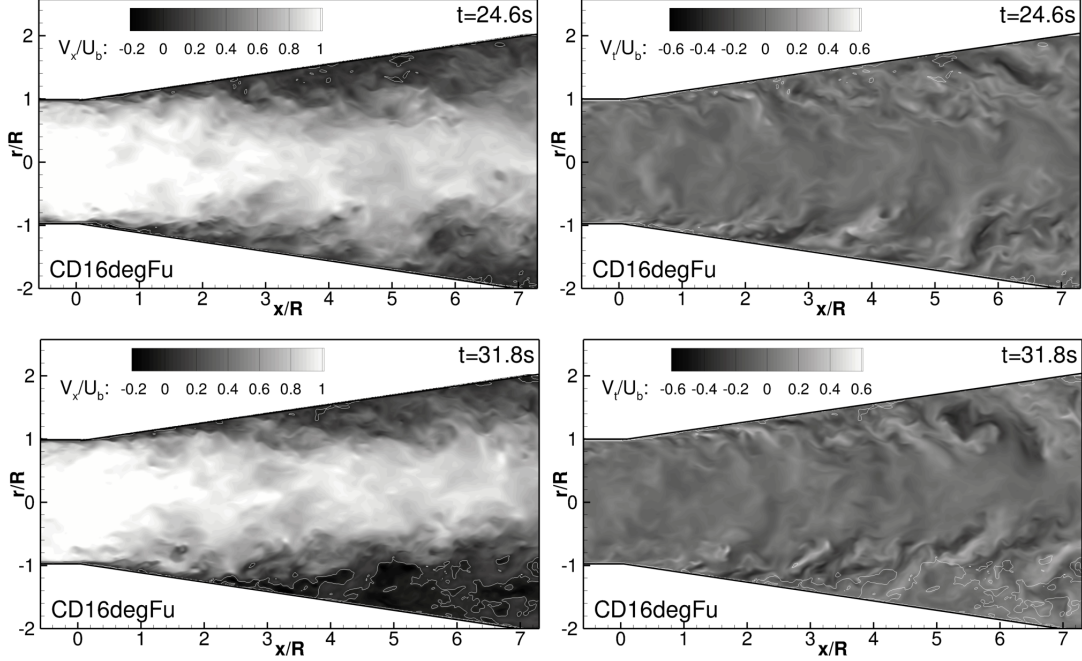


Figure 5.14: Instantaneous axial and tangential velocity fields at two different times ($t=24.6s$ and $t=31.8s$) within CD16degFu

to find a consensus that coherently connects the development of the energy-containing motions through the turbulent boundary layer. Relying on recent studies, Large Scale Motion (LSM) or bulges describes a large packet of coherent structures (from 3-10 quasi-streamwise hairpins) extending over a streamwise length of 2-3 boundary layer thickness while Very Large Scale Motions (VLSM) is a concatenation of LSM spreading over 15-20 radii long in the streamwise direction and reaching height up to 0.5 radius (Guala *et al.* [2006]). Following this consensus, LSM are present in both CD16degFu and CD16degSw illustrated in Fig.5.14 and Fig.5.15. Nonetheless, there is a clear difference in the shape and distribution of the energy-containing motions constituting the LSM of CD16degFu and CD16degSw. These screenshots were carefully selected to reveal the key phenomenons occurring within the diffusers' flow field. The core flow appears more stable when subjected to a tangential momentum, in Fig.5.14 the core flow velocity distribution is similar to a flame with numerous fluctuation while in Fig.5.15 the distribution and smoothness of the core flow is only dis-

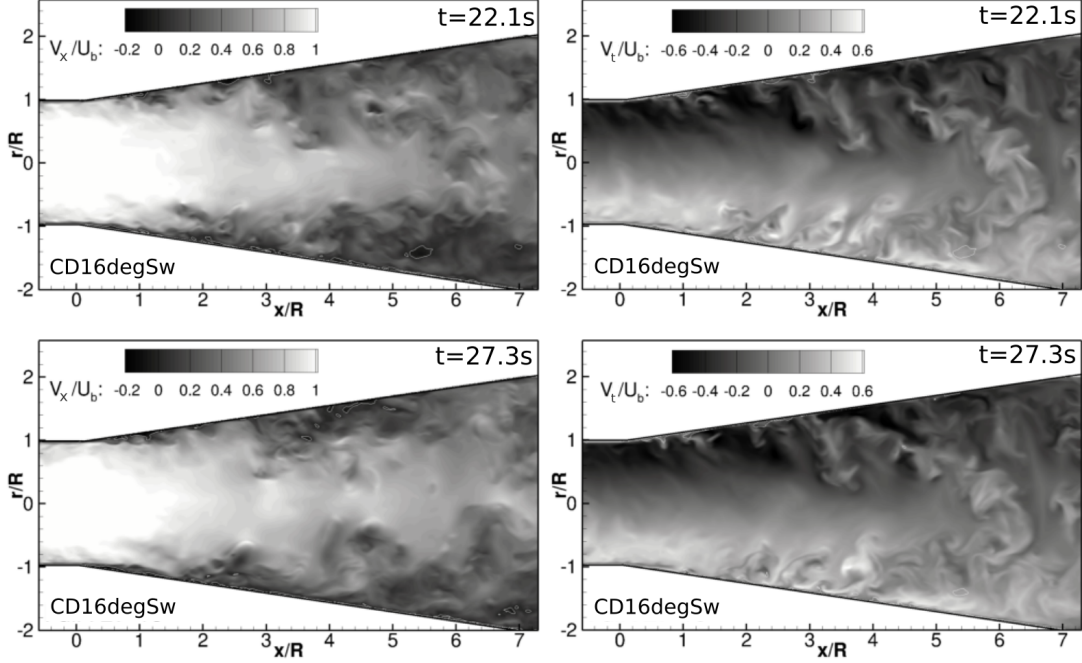
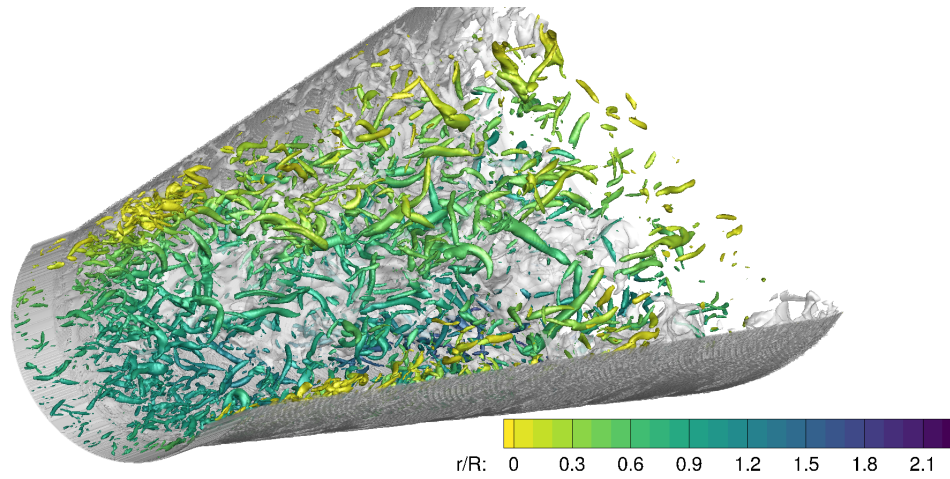


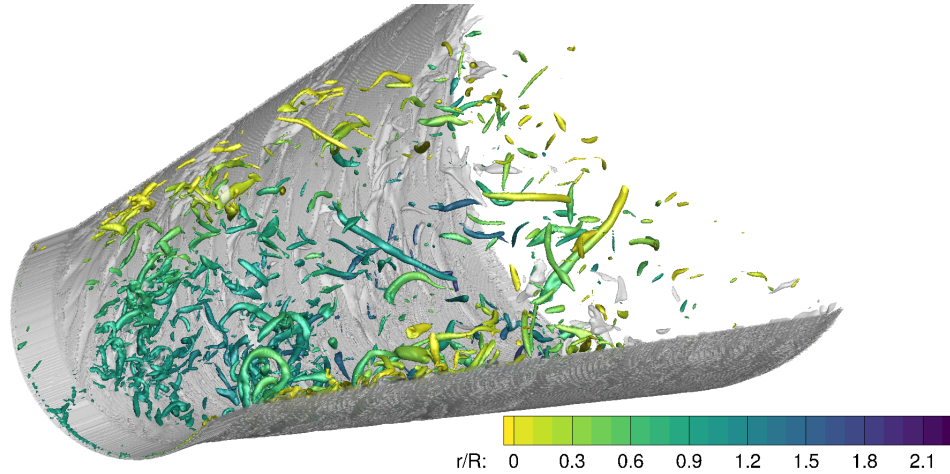
Figure 5.15: Instantaneous axial and tangential velocity fields at two different times ($t=22.1s$ and $t=27.3s$) within CD16degSw

turbed through its interaction with the wall eddies. The normalised tangential flow field V_t/U_b illustrate clearly the difference between the coherent structures of CD16degFu and CD16degSw. Long inclined strips of high and low momentum are witnessed along the full length of the conical diffuser in Fig.5.14, which are characteristic to quasi-streamwise hairpins vortices. These hairpins emerge at the beginning of the diffuser and extend as there travel downstream the diffuser. It is interesting to denote that the hairpin continues their growth at the interface with the instantaneous reversal flow (Fig.5.14 at $t=31.6s$). The swirling inlet enforces the bursting and development of much larger energy-containing motions, Fig.5.15's tangential velocity contour circular motions are depicted at the head of the hairpins, indicating the presence of horseshoes vortices. This phenomenon was previously visualised in compressible shear layers (Gatski & Bonnet [2009]) and referred to as Kelvin-Helmholtz instability (KH). Although the sweep and ejection events occurring from the turbulent boundary layer are of greater magnitude when horseshoes vortices are formed, the distance separating

these horseshoe vortices is greater than the space between each quasi-streamwise hairpins in CD16degFU reducing the frequency and succession of these motion events responsible for the emergence of separated flow.



(a)



(b)

Figure 5.16: Iso-Surface of the criterion $\lambda_2 = 20\%$ of maximum value with r/R contour joint with the iso-surface of the instantaneous axial velocity $V_x = 0$ in grey: (a) CD16degFu (b) CD16degSw

These aforementioned observations are further validated with the visualisation of the coherent structures using the λ_2 criterion in Fig.5.16. Jeong *et al.* [1997]

and Jeong & Hussain [1995] democratised this specific criterion, λ_2 is the second largest negative eigenvalue of the symmetric (Strain rate= $S_{ik}S_{kj}$) and the anti-symmetric (Rotation rate= $\Omega_{ik}\Omega_{kj}$) part of the velocity gradient tensor $u_{i,j}$. The grey iso-surface represents the zero-velocity of the flow and is considered as part of the turbulent boundary layer, the "bursting" of the coherent structure can clearly be depicted. As previously observed in Fig.5.13c-e, the bursting phenomenon occurring in the boundary layer lattice is significantly altered by the tangential momentum where larger but fewer coherent structures arise. It is also more localised in CD16degSw than in CD16degFu where the boundary layer lattice seems to be greatly affected by the bursting of small the energy-containing motion. A greater number of energy-containing motions in CD16degFu concentrates near the core of the diffuser flow. It heralds the presence of large instantaneous recirculation zones.

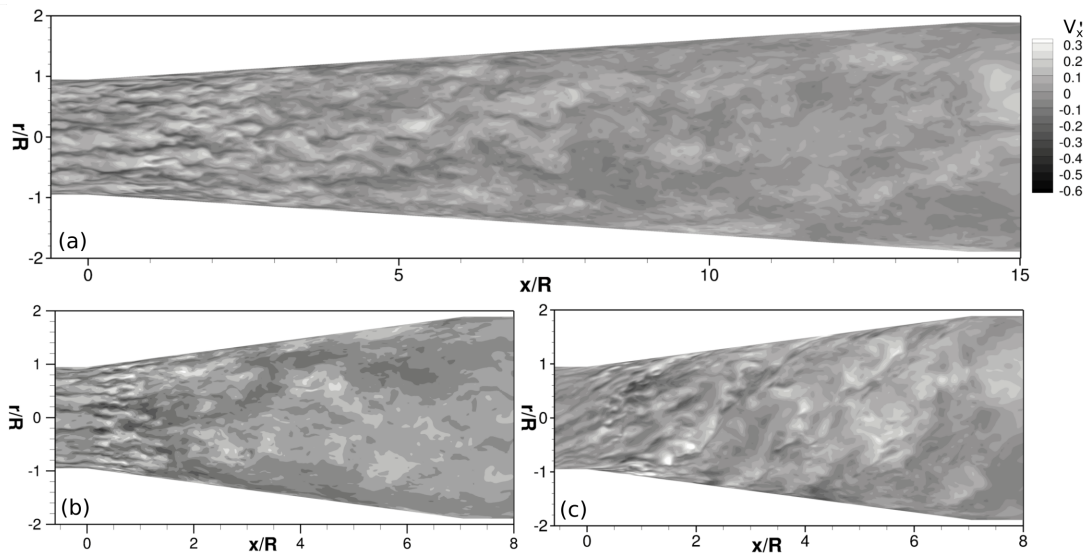


Figure 5.17: Iso-contour of the instantaneous axial fluctuation V'_x at the wall: (a) CD16degFu (b) CD16degFu (c) CD16degSw

The energy-containing motions are also captured for the three diffusers using the iso-contour of the flow field fluctuation at the wall (Fig.5.17). Fig.5.17 displays regions possessing a high density of elongated negative and positive streaks. The presence of these streaks was witness in previous open-channel studies with

zero-pressure gradient (Adrian [2007], Zampiron *et al.* [2020]) and in planar and three-dimensional diffusers where the flow is subjected to high adverse-pressure gradient (Herbst *et al.* [2007], Chap4). It is characteristic to the bursting of low-speed streaks and high-speed streaks flow structures. The streaks are sharply defined in CD8degFu until $x/R=4$ before dissipating into wider area patches, in CD16degFu where the flow is subjected to a higher adverse-pressure gradient the sharp streaks are less elongated and dissipated at a much earlier location along the diffuser ($x/R=1.5$). Similar findings for CD8degFu were described in Lee *et al.* [2012]. As observed in Fig.5.6 the high kinetic zone and shear-layers are located at the interface of the mean flow separation, the separated zone contains a low-momentum with very little shear. Hutchins & Marusic [2007] described those long meandering positive or negative momentum streak as 'superstructures'. The time-averaged high shear zone is a temporal collection of instantaneous shear motions characteristic to the emergence or conveying of coherent structures. Herein these low-magnitude area patches deprived of streaks might be suggesting the existence of instantaneous low-momentum separated bubbles at this location. The dynamics of the streak near the wall showcase a clear disparity in CD16degSw, the swirling-generators which prescribes the tangential velocity rotates the streaks by approximately 45° . The small streaks stand until $x/R=2$ followed by long streaks that subsist along most of the length of the diffuser ($x/R=6$). The low-magnitude patches are harder to locate, suggesting that the tangential velocity prevents the development of instantaneous separated flow.

The Spatial auto-correlation or Two-point correlation reveals and quantify the influence of the pressure gradient and tangential velocity onto the spatial coherence of the velocity fluctuation. The correlation between the target/reference point and its surrounding field is defined as:

$$R_{\mathbf{V}\mathbf{V}}(x, z) = \frac{\overline{\mathbf{V}'(x, z)\mathbf{V}'(x_{ref}, z_{ref})}}{\mathbf{V}_{rms}(x, z) * \mathbf{V}_{rms}(x_{ref}, z_{ref})} \quad (5.3)$$

where \mathbf{V} represents the velocity field (V_x, V_r, V_t) , \mathbf{V}' its fluctuation and \mathbf{V}_{rms} its root mean square while (x, z) are the coordinates of a flow field point which is correlate with the reference point of coordinates (x_{ref}, z_{ref}) . The Two-point correlation at four different locations of the diffusers ($AR=1.16, 1.83, 2.82, 3.74$) at a height of $0.11 * R(AR)$ away from the diffuser wall and is examined for all three velocities $R_{V_x V_x}$, $R_{V_r V_r}$ and $R_{V_t V_t}$. The data was collected for 10000 time-steps over a time period of 25FTPs in all cases. The contour varies from 0.3-0.9 with an increment of 0.15, the dark blue regions correspond to negative correlation values. The comparison of the these quantities between CD8degFu and CD16degFu will determine the impact of the pressure gradient onto the dominant structure while comparing CD16degFu and CD16degSw quantify the effect of the swirling onto the spatial coherence.

The Fig.5.18 presents similar two-points correlation characteristics for CD8degFu and CD16degFu, the correlation area localised at the beginning of the diffuser is significantly smaller than at the end of the diffuser. The correlation proportionally growth along the diffuser length as more ITD and TD separated flow is developed and conveyed. Contrarily, the correlation area in the swirling flow remains relatively constant at the four locations along CD16degSw as the tangential prevents the development of ITD and ID. At the point $AR=1.3$, negative correlation between the wall and the selected location only emerged in CD16degFu preconising the early detachment of the coherent structure from the wall. In Fig.5.20, the three diffuser displays relatively similar evolution of the radial two point correlation at the four different points of the diffuser. The correlation areas spread vertically along the diffusers, nonetheless, a different between CD8degFu, CD16degFu and CD16degSw can be depicted at the first correlation point near the throat of the diffusers. In CD8degFu, the correlation at that point in vertical while an angle can be depicted in CD16degFu which is exacerbated in CD16degSw. The Fig.5.19 corresponds to the two-point correlation of the tangential velocity, CD16degSw correlation at the first point shape is similar to the profile of a horse-shoes vortices and part of the leg is still attached to the wall. This characteristic is not occurring in CD8degFu and CD16degFu where correlation is already fully detached from the wall. The tangential correlation extends and spreads along the

CONICAL DIFFUSER: IMPACT OF A SWIRLING INLET ONTO THE
FLOW-SEPARATION BEHAVIOUR

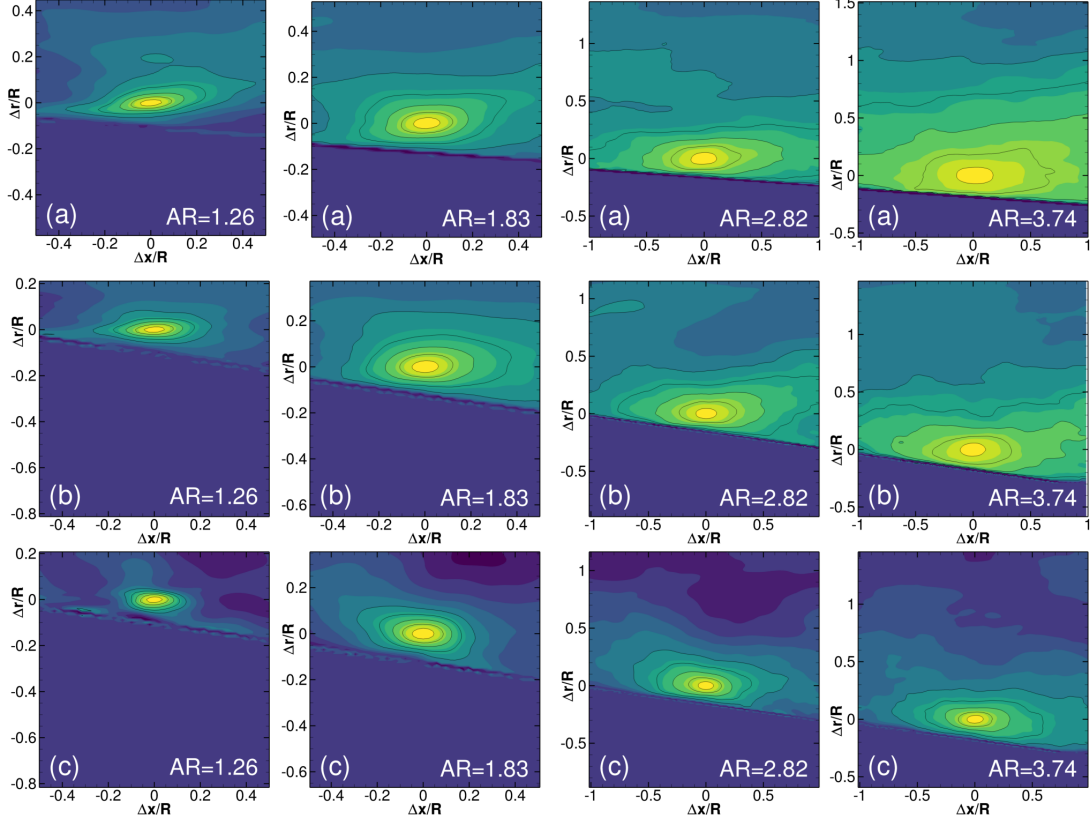


Figure 5.18: Two-points correlations of the axial velocity at four different locations ($AR=1.26, 1.83, 2.82, 3.74$) along the conical diffusers: (a) CD8degFu, (b) CD16degFu, (c) CD16degSw

diffuser while remaining relatively constant in CD8degFu.

5.4 Conclusion

This research presents and validated a new methodology to prescribe a fully turbulent swirling inlet using the mean velocity profile extract from the experiment in conjunction with the production and modification of the fluctuation properties extracted from a precursor pipe flow to best match the turbulence quantities monitor in the experiment. The time-averaged flow properties where no flow separation is identified for a $2\theta = 8^\circ$ opening angle diffuser were validated. Sub-

CONICAL DIFFUSER: IMPACT OF A SWIRLING INLET ONTO THE
FLOW-SEPARATION BEHAVIOUR

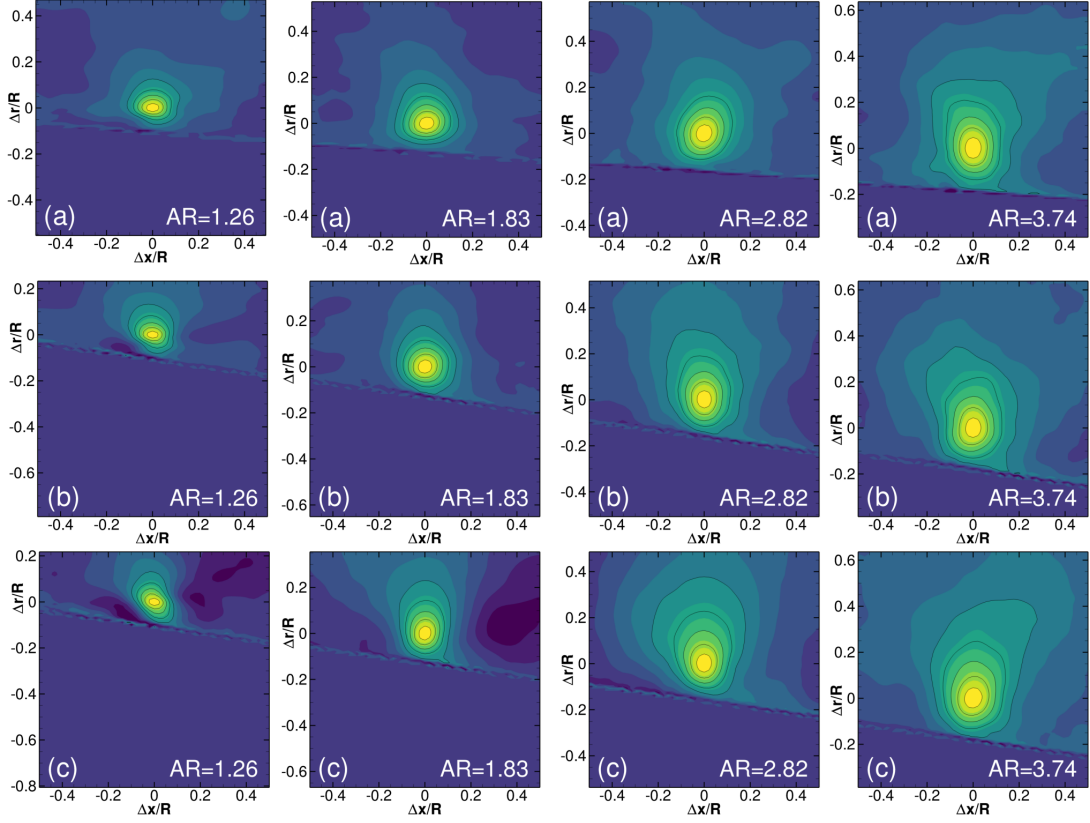


Figure 5.19: Two-points correlations of the radial velocity at four different locations ($AR=1.26, 1.83, 2.82, 3.74$) along the conical diffusers: (a) CD8degFu, (b) CD16degFu, (c) CD16degSw

sequently, to enforce the development of a mean flow separation and assess the impact of a swirling inlet its alteration two parametric simulations on a wide angle opening $2\theta = 16^\circ$ diffusers were performed. The mean flow separation was much greater in CD16degFu (6.2%) than in CD16degSw (2.05%) revealing the reduction impact of the tangential momentum. This significant reduction of the mean flow separation improved the pressure recovery or efficiency by 21% which is equivalent to the losses caused by the reduction of the diffuser and increase of the opening angle. For industrial application the swirling inlet enable a diffuser of $2\theta = 16^\circ$ and half length to have the same efficiency as a $2\theta = 8^\circ$ diffuser subjected to a fully developed axial flow. The investigation of the instantaneous vector field elucidate that hairpin packets aligned in streamwise coherent pattern

CONICAL DIFFUSER: IMPACT OF A SWIRLING INLET ONTO THE
FLOW-SEPARATION BEHAVIOUR

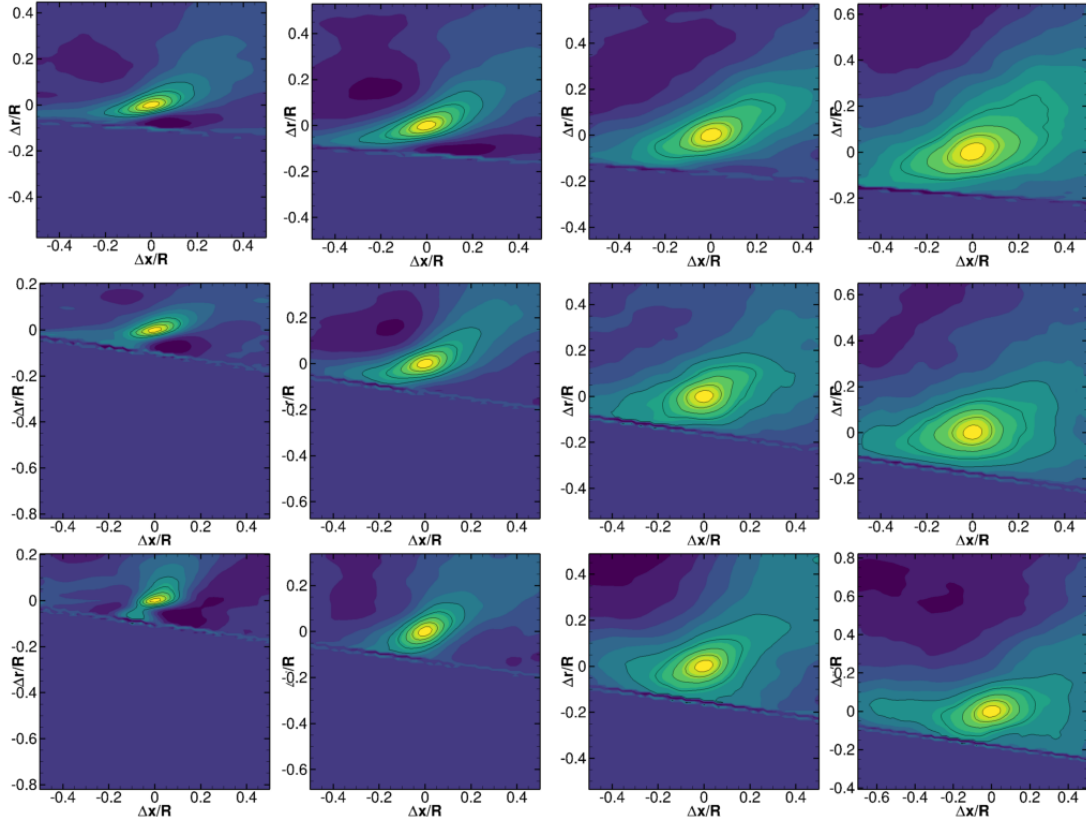


Figure 5.20: Two-points correlations of the tangential velocity at four different locations ($AR=1.26, 1.83, 2.82, 3.74$) along the conical diffusers: (a) CD8degFu, (b) CD16degFu, (c) CD16degSw

in conjunction with a strong adverse-pressure gradient was necessary to create a long-lasting low momentum zone within the turbulent boundary which in turn leads to the development of large temporal and spatial recirculation zone evidenced in CD16degFu. If the adverse-pressure gradient is not significant enough (CD8degFu) or if the hairpin packets streamwise alignment is greatly altered by centrifugal forces induced by a swirling generator (CD16degSw) the instantaneous flow might sporadically separate but it will rapidly dissipate preventing further expansion of the backflow region. A three-dimensional visualisation of the λ_{a2} criterion reveals only low-speed and high-speed streaks in CD16degFu while high energy-containing motions such as horseshoe vortices were located near the throat of CD16degSw. The presence of these horseshoes was further sup-

CONICAL DIFFUSER: IMPACT OF A SWIRLING INLET ONTO THE
FLOW-SEPARATION BEHAVIOUR

ported in a two-point correlation analysis. Overall, the swirling inlet stabilise the core the within the diffuser providing a faster deceleration of the flow.

Chapter 6

Conclusions, Contributions, and Recommendations for Further Studies

6.1 Conclusions

This research employed an advanced Large Eddy Simulation (LES) in-house software (Hydro3D) to investigate and quantify the influence of geometrical and inlet boundary conditions changes on the mean and instantaneous flow separation behaviour. Hydro3D is endowed with complex algorithms. The diffusers' geometry surfaces were all represented using the Immersed Boundary Method (IBM), which has been extensively validated in previous research. The Local Mesh Refinement (LMR) algorithm was used as part of an optimisation strategy. The strategy focused on coarsening the sub-domains located outside the diffuser's effective flow field, leading to significant computational load reductions for each simulation. The optimisation strategy was furthered with an algorithm that detected the cells outside the diffuser's flow field and imposed a null velocity field. It significantly reduced the number of Immersed Boundary Points required across the domain to enforce the no-slip condition. The simulations performed for the

asymmetric rectangular diffuser and the axisymmetric conical diffuser case were extensively validated. For the rectangular diffusers, the first order and second-order statistics were overall in good agreement with [Cherry *et al.*, 2008]. The mean flow separation was slightly over-predicted in the first diffuser D1 (+2.2%) and slightly under-predicted in the second diffuser D2 (-1.5%). In the conical case, the small opening angle diffuser CD8degFu ($2\theta = 8^\circ$) time-averaged properties were validated using Okwuobi & Azad [1973] experimental data. Moreover, the honeycomb swirling generator velocities were calibrated to be in excellent agreement with [Rocklage-Marliani *et al.*, 2003].

The impact of the geometrical changes was depicted in both the rectangular and conical diffusers cases. In the rectangular case, D1 and D2 have two diverging parameters the aspect ratio: $AS_{D1} = 1$, $AS_{D2} = 0.75$ and the area ratio: $AR_{D1} = 4.80$, $AR_{D2} = 4.56$. These geometrical differences lead to a significant disparity in the size of the mean reversal flow volume affecting the efficiency of the diffusers. The mean reversal flow fractional volume in D1 and D2 occupies respectively 16.3% and 9.2% of the diffusers, translating into an efficiency of $\eta_{D1} = 59\%$ and $\eta_{D2} = 55\%$. Their instantaneous flow field was also examined, the backflow coefficient revealed a higher Persistent Transitory Detachment (PTD) zone in the first diffuser ($PTD_{D1} = 4.75\%$) than in the second diffuser ($PTD_{D2} = 0.97\%$), enforcing a greater long-lasting blockage effect in D1, which reduces its pressure recovery. The cumulative fractional volume occupied by the instantaneous backflow was monitored throughout the simulation, a power density spectra analysis of their time series reveals the periodicity of the growth phase ($S_t = 0.7$) and reduction phases ($S_t = 0.1$) of the reversal flow in both diffusers. In the conical case, the increase of the opening angle factor from $2\theta = 8^\circ$ in CD8degFu and $2\theta = 16^\circ$ in CD16degFu severely influence the mean reversal flow and the efficiency of the diffuser. The mean reversal flow is nonexistent in the CD8degFu while occupying 6.2% CD16degFu's fractional volume. The presence of mean reversal flow in CD16degFu reduced its efficiency ($\eta = 50\%$) by 21% compared to CD8degFu ($\eta = 71\%$). The backflow coefficient revealed no PTD regions in neither CD8degFu and CD16degSw.

The impact of inlet characteristics such as a solid-body swirling inflow on the distribution of the coherent structures, which in turn affects the flow separation events and the overall behaviour of the reversal flow is examined in the conical case. The positive influence of the swirling inlet on the mean reversal volume occupying the diffusers with an opening angle of $2\theta = 16^\circ$ and efficiency is clearly revealed in Chap.5. The mean flow separation fractional volumes is reduced from 6.2% to 2% when a honeycomb swirling generator is placed prior to the diffuser's throat. The reduction of the mean flow separation volume inevitably leads to the improvement of the diffuser performance, when subjected to a swirling inlet the diffuser's efficiency increase from 50% to 70%, corresponding to a performance improvement of 20%. The increase of opening angle from $2\theta = 8^\circ$ to $2\theta = 16^\circ$ was performed by dividing the length of CD8degFu by two. The performance losses enforced through the geometrical change was overcome by the introduction of a swirling generator. Indeed, CD8degFu ($\eta = 71\%$) and CD16degSw ($\eta = 70\%$) display similar efficiencies. It is extremely interesting from an engineering point of view, considering a diffuser downstream a bulb turbine, a reduction by half of the length of the diffuser would significantly bring the cost of dam structure down. Moreover, the study of the instantaneous flow field revealed the impact of the swirling inlet onto the distribution of the coherent structure within the turbulent boundary layer of the diffuser's walls. The study of instantaneous flow field snapshots reveals the significant impact of the tangential velocity onto the ejection cycle of the coherent structures. The early ejection of the large energy-containing motions from the boundary layer and their conveying into the core flow prevent the emergence of substantial separated reversal flow within CD16degSw. Furthermore, the iso-surface λ_2 visualisation of the flow field reveals different coherent structures near the throat of the diffuser depending on the inlet boundary condition. The fully developed inlet is endowed with numerous low-speed streak coherent structure while the swirling inlet provides stability to the flow enabling the development of larger energy-containing motions including horseshoes hairpin vortices near the wall of the diffuser. Two conditions need to juxtapose to enforce the development of a large recirculation zone, large hairpin packets composed of quasi-streamwise vortices aligned durably along the diffuser producing a long-lasting low momentum and a high adverse pressure gradient will create the

substantial backflow region when a bursting event occurs.

The coherent structure of the instantaneous flow was monitored and visualised in both diffuser cases. The quadrant analysis in the rectangular diffuser depicted the sweeping and ejections shear event in the vicinity of the turbulent boundary layer, the visualisation of the vortices using the Q-criterion depict the formation of quasi-streamwise vortices at these locations. It validates the bursting paradigm which defines the quasi-cyclic sequence of sweeping and ejections event within the turbulent boundary layer lattice to form energy-containing motions. In the conical case, the λ_2 criterion visualisation revealed both horseshoes and quasi-streamwise vortices. The presence of quasi-streamwise vortices in both diffuser case dismiss the Theodorsen's paradigm which state that the turbulent boundary layer is only composed horseshoes vortices which only differ in scale. The visualisation of hairpin vortices solely relying upon Q criterion and λ_2 criterion snapshot is insufficient to fully validates the single hairpin-vortex paradigm of [Adrian *et al.*, 2000b] and the Townsend attached-eddies hypothesis. Nonetheless, the grouping of the quasi-streamwise vortices and their inclinations are in line with these two latter predictive models.

6.2 Thesis Contributions

The main contributions that the thesis provides to the field of Computational Fluid Dynamics (CFD) and to the field of diffuser's aerodynamics are listed as following:

- implementation of a new boundary condition methodology to accurately prescribe any types of swirling inlet as inflow into a diffuser. It consists of executing a pipe channel precursor simulation and extracting the instantaneous fluctuation field at its outlet once the flow properties are fully converged and developed. Subsequently, the second-order statistics field are evaluated, and in turn, the instantaneous fluctuation field is corrected adequately to match the experiment using parabolic damping equations. Finally, the mean velocity profile extracted from the experimental data is

radially prescribed and is juxtaposed with the instantaneous fluctuation field to provide an accurate instantaneous swirling inlet.

- a novel analysis was introduced to quantify the unsteadiness of the instantaneous flow separation over a specific period of time. The computational implementation calculates at each time-step the number of cells in which the streamwise velocity is inferior to zero within the diffuser flow field. The ratio between the cell that contains reversal flow and the total cells provides the fractional backflow volume occupied by the recirculation pockets. A FFT analysis of the fractional backflow volume time-series provides the frequency of the growth and reduction phase of the flow separation. The root mean square of the time series quantifies the unsteadiness of the instantaneous flow separation around its mean.
- an extensive study of the instantaneous flow field and vector field revealed how the tangential velocity alters the hydrodynamics of the flow field. It elucidates the impact of the centrifugal force on the emergence and development of the energy-containing motions that prevent the formation of large instantaneous recirculation zones.
- [Simpson \[1996\]](#) backflow coefficient is composed of three categories Incipient Detachment (ID : $\gamma = 0.99\%$), Intermittent Transitory Detachment (ITD : $\gamma = 0.8\%$) and Transitory Detachment (ITD : $\gamma = 0.5\%$). This classification only accounts for the intermittent detachment and does not reveals the stagnation zones of the separated flow. For this reason, the Persistent Transitory Detachment (PTD : $\gamma = 0.2\%$) and Permanent Detachment (PTD : $\gamma = 0.01\%$) categories were introduced to depict these long-lasting flow separation zone impacting the pressure recovery and the performance of the diffusers greatly.

6.3 Recommendations for Further Studies

The ability of high-resolution LES simulations in accurately capturing the instantaneous characteristics of the flow separation and the coherent structures has

been demonstrated in this research. Many aspects of these research could be furthered in the future to enhance the knowledge on the flow separation behaviour and the correlation between the energy-containing motions arrangement and the emergence of the instantaneous reversal pockets:

- The impact of other swirling inlet profiles, including concentrated vortex (CV) and wall jet (WJ) on the flow separation and the development of the coherent structures within the turbulent boundary could be investigated.
- Experimental studies ([Harvey \[1962\]](#)) have depicted the presence of core reversal bubble in the middle and near the exit of conical diffusers when the swirling number is considerably high. A numerical investigation could further the understanding of the interaction of the wall coherent structure packets interact and alter the development and behaviours of the core recirculation zone. Further research is required on the impact on the inlet Reynolds number and inlet boundary layer thickness on the size and location of the instantaneous flow separation.
- Lastly, in the hydro-power industry, most barrage hydro-turbines are connected to a diffuser which often consists of a circular entry and a rectangular exit. It would be of great interest to understand how this geometrical transition affects the flow field, the turbulent boundary layer and the efficiency of a diffuser. One could compare performance with a $2\theta = 16^\circ$ diffuser with a circular inlet and rectangular outlet with the $2\theta = 16^\circ$ conical diffuser present in this research.

CONCLUSIONS, CONTRIBUTIONS, AND RECOMMENDATIONS FOR FURTHER
STUDIES

[S] r Radial position [S] R Inlet pipe Radius

References

- ABE, K.I. & OHTSUKA, T. (2010). An investigation of LES and Hybrid LES/RANS models for predicting 3-D diffuser flow. *International Journal of Heat and Fluid Flow*, **31**, 833–844. [34](#), [44](#)
- ADRIAN, R.J. (2007). Hairpin vortex organization in wall turbulence. *Physics of Fluids*, **16**. [viii](#), [12](#), [59](#), [61](#), [91](#)
- ADRIAN, R.J. & MARUSIC, I. (2012). Coherent structures in flow over hydraulic engineering surfaces. *Journal of Hydraulic Research*, **50**, 451–464.
- ADRIAN, R.J., CHRISTENSEN, K.T. & LIU, Z.C. (2000a). Analysis and interpretation of instantaneous turbulent velocity fields. *Experiments in Fluids*, **29**, 275–290. [84](#), [86](#)
- ADRIAN, R.J., MEINHART, C.D. & TOMKINS, C.D. (2000b). Vortex organization in the outer region of the turbulent boundary layer. *Journal of Fluid Mechanics*, **422**, 1–54. [11](#), [86](#), [100](#)
- ARMPFIELD, S. (1988). *Numerical simulation of incompressible turbulent swirling flow in conical diffusers*. Ph.D. thesis, University of Sydney. [65](#)
- ARORA, S. & AZAD, R. (1980). Turbulent kinetic energy balance in a flow with adverse pressure gradient. In *18th Aerospace Sciences Meeting*, American Institute of Aeronautics and Astronautics, Pasadena, CA, U.S.A. [64](#)
- AZAD, R.S. (1996). Turbulent flow in a conical diffuser: A review. *Experimental Thermal and Fluid Science*, **13**, 318–337. [63](#), [64](#), [74](#)

- AZAD, R.S. & BURHANUDDIN, S. (1983). Measurements of some features of turbulence in wall-proximity. *Experiments in Fluids*, **1**, 149–160. [64](#)
- AZAD, R.S. & HUMMEL, R.H. (1971). Measurement of the Intermittency Factor in Diffuser-Flow. *Canadian Journal of Physics*, **49**, 2917–2930. [63](#)
- BACKSHALL, R.G. & LANDIS, F. (1969). The Boundary-Layer Velocity Distribution in Turbulent Swirling Pipe Flow. *Journal of Basic Engineering*, **91**, 728–733. [13](#)
- BALI, T. & SARAC, B.A. (2014). Experimental investigation of decaying swirl flow through a circular pipe for binary combination of vortex generators. *International Communications in Heat and Mass Transfer*, **53**, 174–179. [20](#)
- BANDYOPADHYAY, P. (1980). Large structure with a characteristic upstream interface in turbulent boundary layers. *Physics of Fluids*, **23**, 2326. [viii](#), [12](#)
- BINNIE, A.M. (1957). Experiments on the slow swirling flow of a viscous liquid through a tube. *The Quarterly Journal of Mechanics and Applied Mathematics*, **10**, 276–290. [12](#), [14](#)
- BINNIE, A.M. & TEARE, J. (1956). Experiments on the flow of swirling water through a pressure nozzle and an open trumpet. *Proceedings of the Royal Society of London. Series A. Mathematical and Physical Sciences*, **235**, 78–89. [12](#)
- BLACK, T. (1968). An analytical study of the measured wall pressure field under supersonic turbulent boundary layers. Tech. Rep. CR-888, National Aeronautics and Space Administration. [12](#)
- BOGARD, D.G. & TIEDERMAN, W.G. (1986). Burst detection with single-point velocity measurements. *Journal of Fluid Mechanics*, **162**, 389.
- BROWN, A.C., NAWROCKI, H.F. & PALEY, P.N. (1968). Subsonic diffusers designed integrally with vortex generators. *Journal of Aircraft*, **5**, 221–229. [9](#)
- CHANG, F. (1994). Turbulent flow field in tangentially injected swirl flows in tubes. *International Journal of Heat and Fluid Flow*, **15**, 11. [20](#)

- CHERRY, E.M., ELKINS, C.J. & EATON, J.K. (2008). Geometric sensitivity of three-dimensional separated flows. *International Journal of Heat and Fluid Flow*, **29**, 803–811. [3](#), [33](#), [34](#), [35](#), [38](#), [54](#), [61](#), [68](#), [79](#), [98](#)
- CHERRY, E.M., ELKINS, C.J. & EATON, J.K. (2009). Pressure measurements in a three-dimensional separated diffuser. *International Journal of Heat and Fluid Flow*, **30**, 1–2. [48](#)
- CHERRY, E.M., PADILLA, A.M., ELKINS, C.J. & EATON, J.K. (2010). Three-dimensional velocity measurements in annular diffuser segments including the effects of upstream strut wakes. *International Journal of Heat and Fluid Flow*, **31**, 569–575. [33](#)
- CHORIN, A.J. (1968). Numerical solution of the Navier-Stokes equations. *Mathematics of computation*, **22**, 745–762, iSBN: 0025-5718. [29](#)
- CHRISTENSEN, K.T. & ADRIAN, R.J. (2001). Statistical evidence of hairpin vortex packets in wall turbulence. *Journal of Fluid Mechanics*, **431**, 433–443.
- CLAUSEN, P., KOH, S. & WOOD, D. (1993). Measurements of a swirling turbulent boundary layer developing in a conical diffuser. *Experimental Thermal and Fluid Science*, **6**, 39–48. [14](#), [64](#)
- COCKRELL, D.J., DIAMOND, M.J. & JONES, C.D. (1965). The Diffuser Inlet Flow Parameter. *The Journal of the Royal Aeronautical Society*, **69**, 350–352. [10](#)
- DANIELS, S., RAHAT, A., TABOR, G., FIELDSEND, J. & EVERSON, R. (2020). Shape optimisation of the sharp-heeled Kaplan draft tube: Performance evaluation using Computational Fluid Dynamics. *Renewable Energy*, **160**, 112–126. [5](#)
- DAURICIO, E.T.V. & ANDRADE, C.R. (2017). Numerical Analysis of Swirl Effects on Conical Diffuser Flows. *Journal of Aerospace Technology and Management*, **9**, 91–100. [84](#)
- DAVID, S. (2015). Numerical and experimental investigation of swirling flow in a conical diffuser. EDP Sciences. [66](#)

- DOBY, M.J., NOWAKOWSKI, A.F., NOWAK, E. & DYAKOWSKI, T. (2007). Numerical and experimental examination of swirl flow in a cylindrical container with rotating lids. *Minerals Engineering*, **20**, 361–367. [13](#)
- DUCROS, F., NICOUD, F. & POINSOT, T. (1998). Wall-adapting local eddy-viscosity models for simulations in complex geometries. *Numerical Methods for Fluid Dynamics VI*, 293–299, publisher: Oxford University Computing Laboratory, Wolfson Building, Parks Road, Oxford. [27](#)
- DUQUESNE, P., MACIEL, Y. & DESCHÊNES, C. (2016). Investigation of Flow Separation in a Diffuser of a Bulb Turbine. *Journal of Fluids Engineering*, **138**, 011102. [5](#)
- DÉLERY, J.M. (2001). Robert Legendre and Henri Werlé: Toward the Elucidation of Three-Dimensional Separation. *Annual Review of Fluid Mechanics*, **33**, 129–154. [11](#)
- ESCUE, A. & CUI, J. (2010). Comparison of turbulence models in simulating swirling pipe flows. *Applied Mathematical Modelling*, **34**, 2840–2849. [66](#)
- FEIL, O.G. (1964). Vane Systems for Very-Wide-Angle Subsonic Diffusers. *Journal of Basic Engineering*, **86**, 759–764. [10](#)
- FISHENDEN, C.R. & STEVENS, S.J. (1977). Performance of Annular Combustor-Dump Diffusers. *Journal of Aircraft*, **14**, 60–67. [5](#)
- FURAYA, Y., SATO, T. & KUSHIDA, T. (1966). The Loss of flow in the conical diffuser with suction at the entrance. *Japan Society of Mechanical Engineers*. [10](#)
- GANAPATHISUBRAMANI, B., LONGMIRE, E.K. & MARUSIC, I. (2003). Characteristics of vortex packets in turbulent boundary layers. *Journal of Fluid Mechanics*, **478**, 35–46.
- GATSKI, T. & BONNET, J. (2009). Compressible shear layers. *Compressibility, Turbulence and High Speed Flow*. [88](#)

- GIBSON, A.H. (1910). On the Flow of Water through Pipes and Passages Having Converging or Diverging Boundaries. *Proceedings of the Royal Society A: Mathematical, Physical and Engineering Sciences*, **83**, 366–378. [6](#), [8](#), [10](#)
- GRUNDMANN, S., SAYLES, E.L., ELKINS, C.J. & EATON, J.K. (2012). Sensitivity of an asymmetric 3D diffuser to vortex-generator induced inlet condition perturbations. *Experiments in Fluids*, **52**, 11–21. [34](#)
- GUALA, M., HOMMEMA, S.E. & ADRIAN, R.J. (2006). Large-scale and very-large-scale motions in turbulent pipe flow. *Journal of Fluid Mechanics*, **554**, 521. [87](#)
- HARVEY, J.K. (1962). Some observations of the vortex breakdown phenomenon. *Journal of Fluid Mechanics*, **14**, 585. [102](#)
- HEAD, M.R. & BANDYOPADHYAY, P. (1981). New aspects of turbulent boundary-layer structure. *Journal of Fluid Mechanics*, **107**, 297. [12](#)
- HERBST, A.H., SCHLATTER, P. & HENNINGSON, D.S. (2007). Simulations of Turbulent Flow in a Plane Asymmetric Diffuser. *Flow, Turbulence and Combustion*, **79**, 275–306. [33](#), [91](#)
- HOFFMANN, J.A. (1981). Effects of Free-Stream Turbulence on Diffuser Performance. *Journal of Fluids Engineering*, **103**, 385–390. [10](#)
- HUTCHINS, N. & MARUSIC, I. (2007). Evidence of very long meandering features in the logarithmic region of turbulent boundary layers. *Journal of Fluid Mechanics*, **579**, 1–28. [91](#)
- HWANG, Y. (2015). Statistical structure of self-sustaining attached eddies in turbulent channel flow. *Journal of Fluid Mechanics*, **767**, 254–289.
- IACCARINO, G. & VERZICCO, R. (2003). Immersed boundary technique for turbulent flow simulations. *Applied Mechanics Reviews*, **56**, 331–347. [22](#)
- JAKIRLIĆ, S., KADAVELIL, G., KORNHAAS, M., SCHÄFER, M., STERNEL, D.C. & TROPEA, C. (2010). Numerical and physical aspects in LES and

- hybrid LES/RANS of turbulent flow separation in a 3-D diffuser. *International Journal of Heat and Fluid Flow*, **31**, 820–832. [34](#), [36](#)
- JEONG, J. & HUSSAIN, F. (1995). On the identification of a vortex. *Journal of Fluid Mechanics*, **285**, 69. [90](#)
- JEONG, J., HUSSAIN, F., SCHOPPA, W. & KIM, J. (1997). Coherent structures near the wall in a turbulent channel flow. *Journal of Fluid Mechanics*, **332**, 185–214. [89](#)
- KERREBROCK, J.L. & MEGHREBLIAN, R.V. (1961). Vortex Containment for the Gaseous-Fission Rockett. *Journal of the aerospace sciences*, 15. [13](#)
- KIM, J., MOIN, P. & MOSER, R. (1987). Turbulence statistics in fully developed channel flow at low Reynolds number. *Journal of Fluid Mechanics*, **177**, 133–166. [55](#)
- KLEIN, A. (1981). Review: Effects of Inlet Conditions on Conical-Diffuser Performance. *Journal of Fluids Engineering*, **103**, 250–257. [10](#)
- KLINE, S. (1959). Optimum Design of Straight Walled Dlfusers. *American Society of Mechanical Engineers*. [8](#), [63](#), [84](#)
- KLINE, S. & ROBINSON, S. (1989). Quasi-coherent structures in the turbulent boundary layer. Part I: status report on a community- wide summary of the data. Near Wall Turbulence. Proceedings of Zaric Memorial Conference. [84](#)
- KLINE, S.J., REYNOLDS, W.C., SCHRAUB, F.A. & RUNSTADLER, P.W. (1967). The structure of turbulent boundary layers. *Journal of Fluid Mechanics*, **30**, 741–773.
- KREITH, F. & MARGOLIS, D. (1959). Heat transfer and friction in turbulent vortex flow. *Applied Scientific Research*, **8**, 457–473. [13](#)
- KREITH, F. & SONJU, O.K. (1965). The decay of a turbulent swirl in a pipe. *Journal of Fluid Mechanics*, **22**, 257–271. [14](#)

- LALIBERTE, G.E., SHEARER, M.N. & ENGLISH, M.J. (1983). Design of Energy-Efficient Pipe-Size Expansion. *Journal of Irrigation and Drainage Engineering*, **109**, 13–28. [5](#)
- LAUFER, J. (1954). The structure of turbulence in fully developed pipe flow. *National Advisory Committee for Aeronautics*. [66](#), [73](#)
- LEE, J., JANG, S.J. & SUNG, H.J. (2012). Direct numerical simulations of turbulent flow in a conical diffuser. *Journal of Turbulence*, **13**, N30. [64](#), [91](#)
- LEE, J.H. & SUNG, H.J. (2009). Structures in turbulent boundary layers subjected to adverse pressure gradients. *Journal of Fluid Mechanics*, **639**, 101–131.
- LEGG, R. (2017). Fluid Flow: General Principles. In *Air Conditioning System Design*, 225–257, Elsevier. [viii](#), [7](#)
- LIVESEY, J. & TURNER, J. (1964). The effect of velocity profile decay on shear flow in diffusers. *International Journal of Mechanical Sciences*, **6**, 371–379. [9](#)
- MAGER, A. (1971). Incompressible, viscous, swirling flow through a nozzle. *American Institute of Aeronautics and Astronautics*, 10. [13](#)
- MALM, J., SCHLATTER, P. & HENNINGSON, D.S. (2012). Coherent structures and dominant frequencies in a turbulent three-dimensional diffuser. *Journal of Fluid Mechanics*, **699**, 320–351. [34](#), [61](#)
- MCDONALD, A. & FOX, R. (1966). An experimental investigation of incompressible flow in conical diffusers. *International Journal of Mechanical Sciences*, **8**, 125–139. [viii](#), [9](#), [11](#), [73](#)
- MCDONALD, A.T., FOX, R.W. & VAN DEWOESTINE, R.V. (1971). Effects of swirling inlet flow on pressure recovery in conical diffusers. *American Institute of Aeronautics and Astronautics*, **9**, 2014–2018. [viii](#), [14](#), [64](#), [65](#), [78](#)
- MCMILLAN, O. & JOHNSTON, J. (1973a). Part I: Performance of Low-Aspect-Ratio Diffusers With Fully Developed Turbulent Inlet Flows. *Journal of Fluid Mechanics*. [8](#)

- MCMILLAN, O. & JOHNSTON, J. (1973b). Part II : Performance of Low-Aspect-Ratio Diffusers With Fully Developed Turbulent Inlet Flows. *Journal of Fluid Mechanics*, **8**, 11
- MEINHART, C.D. & ADRIAN, R.J. (1995). On the existence of uniform momentum zones in a turbulent boundary layer. *Physics of Fluids*, **7**, 694–696. [86](#)
- MORRISON, J.F., TSAI, H.M. & BRADSHAW, P. (1989). Conditional-sampling schemes for turbulent flow, based on the variable-interval time averaging (VITA) algorithm. *Experiments in Fluids*, 15.
- MUSHATET, K.S., RISHAK, Q.A. & FAGR, M.H. (2020). Experimental and numerical investigation of swirling turbulent flow and heat transfer due to insertion of twisted tapes of new models in a heated tube. *Applied Thermal Engineering*, **171**, 115070. [66](#)
- NAJAFI, A., SAIDI, M., SADEGHIPOUR, M. & SOUHAR, M. (2005). Boundary layer solution for the turbulent swirling decay flow through a fixed pipe: SBR at the inlet. *International Journal of Engineering Science*, **43**, 107–120. [20](#)
- NICOUD, F. & DUCROS, F. (1999). Subgrid-Scale Stress Modelling Based on the Square of the Velocity Gradient Tensor. *Flow, Turbulence and Combustion*, **62**, 183–200. [27](#)
- OBI, S., AOKI, K. & MASUDA, S. (1993). Experimental and computational study of turbulent separating flow in an asymmetric plane diffuser. In *Ninth Symposium on Turbulent Shear Flows, Hyoto, Japan*, 305–1. [33](#)
- OBI, S., NIKAIDO, H. & MASUDA, S. (1999). Reynolds Number Effect on the Turbulent Separating Flow in an Asymmetric Plane Diffuser. *American Society of Mechanical Engineers*, 7. [33](#)
- OHLSSON, J., SCHLATTER, P., FISCHER, P.F. & HENNINGSON, D.S. (2010). Direct numerical simulation of separated flow in a three-dimensional diffuser. *Journal of Fluid Mechanics*, **650**, 307–318. [34](#), [35](#), [38](#), [42](#), [46](#)

- OKHIO, C.B., HORTON, H.P. & LANGERT, G. (1983). Effects of swirl on flow separation and performance of wide angle diffusers. *International Journal of Heat and Fluid Flow*, **4**, 8. [14](#)
- OKWUOBI, P.A.C. & AZAD, R.S. (1973). Turbulence in a conical diffuser with fully developed flow at entry. *Journal of Fluid Mechanics*, **57**, 603–622. [3](#), [64](#), [65](#), [66](#), [68](#), [70](#), [73](#), [76](#), [98](#)
- OKWUOBI, P.A.C., AZAD, R.S. & HAWALESKA, O. (1972). Turbulence structure parameters in an inhomogeneous strain field. *American Institute of Aeronautics and Astronautics*, **10**, 1414–1417. [73](#)
- OURO, P., FRAGA, B., LOPEZ-NOVOA, U. & STOESSER, T. (2019). Scalability of an Eulerian-Lagrangian large-eddy simulation solver with hybrid MPI/OpenMP parallelisation. *Computers & Fluids*, **179**, 123–136. [38](#)
- PATTERSON, G.N. (1938). Modern Diffuser Design. *Aircraft Engineering*, **7**. [6](#), [63](#), [65](#)
- PERRY, A.E. & CHONG, M.S. (1982). On the mechanism of wall turbulence. *Journal of Fluid Mechanics*, **119**, 173–217.
- PERRY, A.E., HENBEST, S. & CHONG, M.S. (1986). A theoretical and experimental study of wall turbulence. *Journal of Fluid Mechanics*, **165**, 163.
- PESKIN, C.S. (1972). Flow patterns around heart valves: a numerical method. *Journal of computational physics*, **10**, 252–271, iSBN: 0021-9991 Publisher: Elsevier. [22](#)
- PESKIN, C.S. (1982). The Fluid Dynamics of Heart Valves: Experimental, Theoretical, and Computational Methods. *Annual Review of Fluid Mechanics*, **14**, 235–259. [22](#)
- PETERS, H. (1931). Energieumsetzung in Querschnitts-erweiterungen bei verschiedenen Zulaufbedingungen. *Ingenieur-Archiv*. [8](#)

- RAO, K.N., NARASIMHA, R. & NARAYANAN, M.A.B. (1971). The ‘bursting’ phenomenon in a turbulent boundary layer. *Journal of Fluid Mechanics*, **48**, 339–352.
- ROBINSON, S.K. (1991). Coherent Motions in the Turbulent Boundary Layer. *Annual Review of Fluid Mechanics*, 39. [11](#)
- ROCHINO, A. & LAVAN, Z. (1969). Analytical Investigations of Incompressible Turbulent Swirling Flow in Stationary Ducts. *Journal of Applied Mechanics*, **36**, 151–158. [12](#), [13](#)
- ROCKLAGE-MARLIANI, G., SCHMIDTS, M. & VASANTA RAM, V.I. (2003). Three-Dimensional Laser-Doppler Velocimeter Measurements in Swirling Turbulent Pipe Flow. *Flow, Turbulence and Combustion (formerly Applied Scientific Research)*, **70**, 43–67. [3](#), [65](#), [66](#), [67](#), [70](#), [71](#), [83](#), [98](#)
- SCHNEIDER, H. (2009). Reliable and Accurate Prediction of Three-Dimensional Separation in Asymmetric Diffusers Using Large-Eddy Simulation. In *Proceedings of ASME Turbo Expo 2009: Power for Land, Sea and Air*, 10. [34](#), [35](#), [42](#)
- SCHUBAUER, G. & SPANGENBERG, W. (1948). Effect of screens in wide-angle diffusers. [10](#)
- SENOO, Y. (1974). Improvement of the performance of conical diffusers by vortex generators. *American Society of Mechanical Engineers*. [10](#), [65](#)
- SIMPSON, R.L. (1996). Aspects of turbulent boundary-layer separation. *Progress in Aerospace Sciences*, **32**, 457–521. [51](#), [52](#), [80](#), [101](#)
- SINGH, R.K. & AZAD, R.S. (1995a). Measurement of instantaneous flow reversals and velocity field in a conical diffuser. *Experimental Thermal and Fluid Science*, **10**, 397–413. [73](#)
- SINGH, R.K. & AZAD, R.S. (1995b). The structure of instantaneous reversals in highly turbulent flows. *Experiments in Fluids*, **18**, 409–420. [64](#)

- SINGH, R.K. & AZAD, R.S. (1995c). Structure of Turbulence in an Incipient-Separating Axisymmetric Flow. *Journal of Fluids Engineering*, **117**, 433–438. [64](#)
- SMITHBERG, E. & LANDIS, F. (1964). Friction and Forced Convection Heat-Transfer Characteristics in Tubes with Twisted Tape Swirl Generators. *Journal of Heat Transfer*. [13](#)
- SO, K.L. (1967). Vortex phenomena in a conical diffuser. *American Institute of Aeronautics and Astronautics*, **5**, 1072–1078. [14](#), [64](#)
- STEENBERGEN, W. & VOSKAMP, J. (1998). The rate of decay of swirl in turbulent pipe flow. *Flow Measurement and Instrumentation*, **9**, 67–78. [20](#)
- STOESSER, T. (2001). *Development and validation of a CFD-code for turbulent open-channel flows..* PhD, Bristol University. [16](#)
- TARDU, S. (1995). Characteristics of single and clusters of bursting events in the inner layer. *Experiments in Fluids*, **13**.
- THEODORSEN, T. (1952). Mechanism of turbulence. *Proceedings 2nd Midwestern Conference on Fluid Mechanics*. [11](#)
- THEODORSEN, T. (1955). The structure of turbulence. *50 Jahre Grenzschichtforschung*. [11](#)
- TOMKINS, C.D. & ADRIAN, R.J. (1999). Characteristic of Vortex Packets in Wall Turbulence. *First Symposium on Turbulence and Shear Flow Phenomena*. [61](#)
- TOWNSEND, A. (1976). The Structure of Turbulent Shear Flow. *Cambridge University Press*. [11](#)
- TÖRNBLUM, O., LINDGREN, B. & JOHANSSON, A.V. (2009). The separating flow in a plane asymmetric diffuser with 8.5° opening angle: mean flow and turbulence statistics, temporal behaviour and flow structures. *Journal of Fluid Mechanics*, **636**, 337–370. [33](#), [48](#)

- UHLMANN, M. (2005). An Immersed Boundary Method with Direct Forcing for the Simulation of Particulate Flows. *Journal of Computational Physics*, **209**, 448–476, arXiv: 1809.08170. [24](#)
- VENTURI, G.B... (1797). *Recherches expérimentales sur le principe de la communication latérale du mouvement dans les fluides, appliqué à l'explication de différens phénomènes hydrauliques..* [6](#)
- WAITMAN, B.A., RENEAU, L.R. & KLINE, S.J. (1961). Effects of Inlet Conditions on Performance of Two-Dimensional Subsonic Diffusers. *Journal of Basic Engineering*, **83**, 349–360. [9](#)
- WALLACE, J.M. (2016). Quadrant Analysis in Turbulence Research: History and Evolution. *Annual Review of Fluid Mechanics*, **48**, 131–158. [12](#)
- WALLACE, J.M. & BRODKEY, R.S. (1977). Reynolds stress and joint probability density distributions in the u-v plane of a turbulent channel flow. *Physics of Fluids*, **20**, 351. [56](#)
- WALLACE, J.M., ECKELMANN, H. & BRODKEY, R.S. (1972). The wall region in turbulent shear flow. *Journal of Fluid Mechanics*, **54**, 39–48. [55](#)
- WELSH, M. (1976). Flow control in wide-angled conical diffusers. *American Society of Mechanical Engineers*. [10](#)
- WESKE, J.R. & PLANTHOLT, A.H. (1953). Discrete Vortex Systems in the Transition Range of Fully Developed Flow in a Pipe. *Journal of the Aeronautical Sciences*, **20**, 717–718. [12](#)
- WHITE, A. (1964). Flow of a Fluid in an Axially Rotating Pipe. *Journal of Mechanical Engineering Science*, **6**, 47–52. [13](#)
- WU, X., SCHLÜTER, J., MOIN, P., PITSCH, H., IACCARINO, G. & HAM, F. (2006). Computational study on the internal layer in a diffuser. *Journal of Fluid Mechanics*, **550**, 391. [33](#)
- YASUTOSHI SENOO, KAWAGUCHI NOBUMASA & NAGATA TETSUZOU (1978). Swirl Flow in Conical Diffusers. *Japan Society of Mechanical Engineers*. [65](#)

- YILMAZ, M. (1999). Enhancement of heat transfer by turbulent decaying swirl flow. *Energy Conversion*, 12. [20](#)
- ZAMPIRON, A., CAMERON, S. & NIKORA, V. (2020). Secondary currents and very-large-scale motions in open-channel flow over streamwise ridges. *Journal of Fluid Mechanics*, **887**, A17. [91](#)
- ZHANG, R.K., MAO, F. & LIU, S.H. (2009). Characteristics and Control of the Draft-Tube Flow in Part-Load Francis Turbine. *Journal of Fluids Engineering*, **131**. [5](#)
- ZHOU, J., ADRIAN, R.J. & BALACHANDAR, S. (1996). Autogeneration of near-wall vortical structures in channel flow. *Physics of Fluids*, **8**, 288–290.
- ZHOU, J., ADRIAN, R.J., BALACHANDAR, S. & KENDALL, T.M. (1999). Mechanisms for generating coherent packets of hairpin vortices in channel flow. *Journal of Fluid Mechanics*, **387**, 353–396. [55](#), [59](#)